Characterisation of Micromechanical Materials and MEMS Structures using Optically Generated Ultrasound

by

Campbell McKee

CMP (Centre for Microsystems and Photonics)

Department of Electronic and Electrical Engineering

University of Strathclyde

A thesis submitted to the Department of Electronic and Electrical Engineering of the University of Strathclyde for the degree of Doctor of Philosophy.

Prof. Brian Culshaw   Internal Supervisor

Prof. Richard Leach   External Supervisor

December 2014

Declaration

This thesis is the result of the author's original research. It has been composed by the author and has not been previously submitted for examination which has led to the award of a degree.

The copyright of this thesis belongs to the author under the terms of the United Kingdom Copyright Acts as qualified by University of Strathclyde Regulation 3.50. Due acknowledgment must always be made of the use of any material contained in, or derived from, this thesis.

Signature:

Date:

How many times when you are working on something frustratingly tiny, like your wife's wrist watch, have you said to yourself, "If I could only train an ant to do this!" What I would like to suggest is the possibility of training an ant to train a mite to do this. What are the possibilities of small but movable machines? They may or may not be useful, but they surely would be fun to make.

"There's Plenty of Room at the Bottom," Richard P. Feynman 1959.

Abstract

Due to the increased commercial demand for miniaturisation, MEMS manufacturers have to characterise their components to improve quality control with ever-higher accuracy and resolution. One method of characterisation, using laser-generated and detected ultrasonic Lamb waves, is described in this thesis. Laser generated ultrasound is an attractive approach for material testing as it provides a non-contact non-destructive characterisation method. In the work reported here, Lamb waves are generated using a broadband laser source, giving a high temporal and spatial bandwidth, and the generated Lamb waves are detected using either a commercially available vibrometer or a custom built large bandwidth Michelson interferometer.

An investigation has been conducted on the optical conversion efficiency into Lamb waves. Lamb wave amplitudes were measured on a silicon wafer and a variety of thin films on silicon wafers. This was to determine how parameters such as absorption coefficient and optical reflectivity as functions of excitation wavelength, influence the generation of Lamb waves. As a result, it was concluded that light of wavelength 532 nm is the optimal wavelength for Lamb wave generation.

The capabilities of laser-generated Lamb waves, coupled with a large bandwidth Michelson interferometer, have been demonstrated to accurately measure the thickness of a MEMS pressure sensor membrane in the [110] direction of a silicon wafer. Using the reassigned Gabor time-frequency method, to produce group velocity dispersion curves, the thickness was determined to be 35.01 μm ± 0.18 μm, from a single measurement. For comparison, the thickness was measured using an independent technique; obtaining a value of 34.60 μm ± 0.27 μm. Values for Young's modulus and Poisson's ratio were also determined to be 163 GPa ± 11.7 GPa and 0.351 respectively and these are in good agreement (to within 3.6% for Young's modulus and 2.5% for Poisson's ratio) with values found in the literature.

Acknowledgments

The work involved in completing this PhD and thesis would not have been possible without the support of a great number of people. Within the University, first and foremost, a great deal of thanks has to be given to my supervisor, Prof. Brian Culshaw for his support, patience, and at times, much needed criticism. Alongside Prof. Culshaw, was a very friendly and helpful team who included Dr. Gareth Pierce, Dr Graham Thursby, Dr Alison Cleary, Dr Ian Armstrong, Dr Istvan Veres, Dr Gordon Flockhart, Dr Michael Lengdon and Mr Gordon Brown. I would especially like to thank Dr Alison Cleary and Dr Ian Armstrong for their massive contributions to the construction of the Michelson interferometer.

Dr Borja Sorazu, although he had left the university, was also able to make time for various disscusions regarding his previous work.

From NPL, I would like to thank Prof Richard Leach for his continued support and motivational talks, and his help in getting this thesis ready for submission. I would also like to thank Dr Nigel Jennett for his help and advice on the equipment in his lab.

Thesis Funding

This research has been funded by an EPSRC grant (EP/E053319/1) and complimented by a CASE award from the National Physical Laboratory (NPL).

Contents

ABSTRACT .... **I**

ACKNOWLEDGMENTS .... **II**

THESIS FUNDING .... **III**

CONTENTS .... **IV**

FIGURES .... **VIII**

NOMENCLATURE .... **XV**

1 INTRODUCTION **1**

1.1 WHY CHARACTERISE THE MEMS PRESSURE SENSOR? 1

1.2 OVERVIEW OF THESIS 3

1.3 REFERENCES 5

2 THE MEMS PRESSURE SENSOR AND CHARACTERISATION OF MEMS DEVICES **6**

2.1 INTRODUCTION 6

2.2 THE MEMS PRESSURE SENSOR 6

2.3 CURRENT TECHNIQUES FOR CHARACTERISING MEMS SENSORS, THIN FILMS AND SILICON WAFERS 11

2.3.1 Characterisation of MEMS mechanical properties *12*

2.3.1.1 Thickness measurements 12

2.3.1.2 Mechanical properties of MEMS 14

2.3.2 Commercially available equipment *15*

2.3.2.1 Capacitive sensor for thickness measurements 15

2.3.2.2 Nanoindentation and impact excitation 16

2.3.2.3 LAwave SAW spectrometer 17

2.3.2.4 Wafer thickness measurement using optical methods 18

2.3.2.5 Vibrational measurements 18

2.4 CONCLUSIONS 19

2.5 REFERENCES 19

3 GENERATION OF ELASTIC WAVES USING LASER PULSES **24**

3.1 INTRODUCTION 24

3.2 LASER GENERATED ULTRASOUND 24

3.3 ADVANTAGES AND DISADVANTAGES OF LASER BASED ULTRASONIC SYSTEMS 25
3.4 MECHANISMS OF THERMOELASTIC LASER GENERATED ULTRASOUND . 29
3.4.1 Optical absorption in metals 29
3.4.2 Optical absorption in semiconductors.... 30
3.5 HEATING THROUGH OPTICAL ABSORPTION 32
3.6 THE THERMO-ELASTO DYNAMIC PROBLEM 36
3.7 PHOTOSTRICTION AS AN ACOUSTIC WAVE GENERATION SOURCE 37
3.8 CONCLUSIONS 38
3.9 REFERENCES.... 38
4 OPTICAL DETECTION OF ELASTIC WAVES.... 43
4.1 INTRODUCTION 43
4.2 REVIEW OF OPTICAL METHODS FOR ULTRASONIC WAVE DETECTION ... 44
4.2.1 Non interferometric detection of ultrasound 44
4.2.2 Interferometric detection of ultrasound.... 45
4.3 THE PATH STABILISED MICHELSON INTERFEROMETER.... 47
4.3.1 Calibration of the Michelson interferometer..... 55
4.3.2 Electronic stabilisation of the Michelson interferometer to compensate for background vibrations 56
4.4 NOISE CONSIDERATIONS, SENSITIVITY AND SOURCES OF ERROR 58
4.5 CONCLUSIONS 61
4.6 REFERENCES.... 61
5 GUIDED ELASTIC WAVES IN ANISOTROPIC MEDIA AND THE MECHANICAL PROPERTIES OF SILICON.... 65
5.1 INTRODUCTION 65
5.2 GUIDED ELASTIC WAVES IN PLATES 65
5.3 A NOTE ON SILICON CRYSTAL ORIENTATION 71
5.4 CONCLUSIONS 75
5.5 REFERENCES.... 75
6 DEPENDENCE OF OPTICAL WAVELENGTH ON LASER GENERATED ULTRASOUND 77
6.1 INTRODUCTION 77
6.2 MATERIALS UNDER INVESTIGATION 77

6.3 EXPERIMENTAL METHOD 80

6.3.1 Errors in the Measurement Process 84

6.4 RESULTS AND DISCUSSION 85

6.4.1 Acoustic wave generation in the metals 85

6.4.1.1 Aluminium 90

6.4.1.2 Chromium 94

6.4.1.3 Copper 97

6.4.2 Acoustic wave generation in the silicon 101

6.4.3 Acoustic wave generation in the semiconductors with thin metallic films 105

6.5 PHOTOSTRICTION AS A METHOD OF GENERATING ACOUSTIC WAVES IN SILICON 113

6.6 CONCLUSIONS. 115

6.7 REFERENCES. 116

7 CHARACTERISATION OF THE MEMS PRESSURE SENSOR 119

7.1 INTRODUCTION 119

7.2 TIME–FREQUENCY ANALYSIS OF LAMB WAVES. 119

7.3 SHORT TIME FOURIER TRANSFORM. 120

7.4 THE REASSIGNMENT METHOD 125

7.5 GENERATING GUIDED ELASTIC WAVES IN A MEMS PRESSURE SENSOR 127

7.6 DISPERSION CURVE SENSITIVITY 131

7.6.1 Variation in Thickness 132

7.6.2 Variation in Young's Modulus 135

7.6.3 Variation in Poisson's Ratio 137

7.7 THE MEMS PRESSURE SENSOR 140

7.7.1 Plate velocity 144

7.7.2 Rayleigh velocity 145

7.7.3 The S_1 mode and membrane thickness 146

7.8 ESTIMATION OF YOUNG'S MODULUS AND POISSON'S RATIO IN THE [110] DIRECTION 150

7.9 EXPERIMENTAL AND THEORETICAL RESULTS 150

7.10 FUTURE EXPERIMENTS 152

7.11 CONCLUSIONS 153

7.12 REFERENCES 153
8 COMPARISON OF OTHER TECHNIQUES TO MEASURE THE THICKNESS OF A MEMS PRESSURE SENSOR MEMBRANE .. 156
8.1 INTRODUCTION 156
8.2 SCANNING ELECTRON MICROSCOPE 156
8.3 INFRARED TRANSMISSION OF THE MEMS PRESSURE SENSOR MEMBRANE 158
8.4 CONCLUSIONS 161
8.5 REFERENCES 161
9 CONCLUSIONS AND FUTURE WORK 163
9.1 CONCLUSIONS 163
9.2 FUTURE WORK 165
PUBLICATIONS 166

Figures

Figure 1.1: Industry applications of the MEMS pressure sensor. 3
Figure 2.1: Schematic illustration of a pressure sensor with diffused piezoresistive elements. Overall dimensions are approximately 2 mm^2 and resistor R4 would be located opposite resistor R1 (section cut away). 8
Figure 2.2: The four resistive elements form a Wheatstone bridge configuration....... 8
Figure 2.3: Effect of Potassium Hydroxide etchant on (100) plane of a silicon wafer to produce a membrane. 9
Figure 2.4: SEM image of MEMS pressure sensor. 10
Figure 2.5: SEM image of MEMS pressure sensor, with one edge removed showing cross-section. 11
Figure 2.6: Outcome of recent survey on important characteristics needing addressed in MEMS sensors. 12
Figure 2.7: Sites for thickness measurement on wafers with flat. 13
Figure 2.8: Sites for thickness measurement on wafers with notch. 14
Figure 2.9: Basic operating principles of the LAwaves system [25]. 17
Figure 3.1: Laser based system used in this thesis. 26
Figure 3.2: Optical reflectivity of the metals and semiconductors under investigation. 32
Figure 3.3: Longitudinal acoustic wavelength and thermal diffusion length as a function of frequency in silicon. 33
Figure 3.4: Laser generation of ultrasound in the thermoelastic regime.................... 36
Figure 4.1: Ultrasonic signals superimposed on a low frequency background from an unstabilised interferometer. 48
Figure 4.2: Schematic layout of Michelson interferometer. 50
Figure 4.3: Two beam interferometer output intensity as a function of phase change. The largest variation in output intensity for a small phase change occurs at the quadrature point 51
Figure 4.4: Schematic layout of the path stabilised Michelson interferometer constructed for the detection of acoustic waves. 53

Figure 4.5: The Michelson interferometer. 54
Figure 4.6: Beam profile of HeNe laser and ×100 microscope objective. 55
Figure 4.7: Schematic diagram of the electronic feedback stabilisation circuit. 58
Figure 5.1: Symmetric Lamb wave modes. 66
Figure 5.2: Anti-symmetric Lamb wave modes. 67
Figure 5.3: Example of a lamb wave measured in a 50 µm silicon wafer. Calibration procedure given in section 4.3.1 69
Figure 5.4: Lamb wave phase velocity dispersion curves for a 50 µm silicon wafer in the [110] direction. 70
Figure 5.5: Lamb wave group velocity dispersion curves for a 50 µm silicon wafer in the [110] direction. 70
Figure 5.6: Image identifying various planes in a wafer of (100) orientation 72
Figure 5.7 The primary and secondary flats of {100} and {111} wafers for both n-type and p-type doping.: 73
Figure 5.8: Lamb wave phase velocity dispersion curves for a 50 µm silicon wafer in the [100] and [110] direction. Solid lines refer to the [100] direction and dashed lines refer to the [110] direction. 74
Figure 6.1: Stylus profile measurement of aluminium film on silicon substrate, thickness = 118 nm. 79
Figure 6.2: Stylus profile measurement of chromium film on silicon substrate, thickness = 97 nm. 79
Figure 6.3: Stylus profile measurement of copper film on silicon substrate, thickness = 188 nm. 80
Figure 6.4: Schematic of experimental setup showing generation laser with attenuator, 2nd and 3rd harmonic generator, focusing the beam onto the surface with a cylindrical lens. Also shown is the detection system, a laser vibrometer. 82
Figure 6.5: Metallic thin film coating on silicon substrate. 82
Figure 6.6: Lamb waves generated in a silicon wafer with chromium thin film at differing pulse energies using 532 nm light. 83

Figure 6.7: Lamb waves generated in a silicon wafer with chromium thin film using three different wavelengths, 1064 nm, 532 nm and 355 nm, with a pulse energy of 9.8 mJ. 84
Figure 6.8: Relationship between plasma frequency, refractive index, extinction coefficient and real part of the dielectric constant in copper. 89
Figure 6.9: Reflectivity of aluminium in vacuum. 91
Figure 6.10: Peak to peak amplitude representation of acoustic waves generated in an aluminium plate at three optical wavelengths and varying pulse energies. 92
Figure 6.11: Generated acoustic wave amplitudes in aluminium, compensated for optical reflectivity. 93
Figure 6.12: Peak to peak amplitude representation of acoustic waves generated in a chromium plate at two optical wavelengths and varying pulse energies. 94
Figure 6.13: Generated acoustic wave amplitudes in Chromium, compensated for optical reflectivity. 95
Figure 6.14: Reflectivity of chromium in vacuum. 96
Figure 6.15: Reflectivity of copper in vacuum. 97
Figure 6.16: Peak to peak amplitude representation of acoustic waves generated in a copper plate at three optical wavelengths and varying pulse energies.... 98
Figure 6.17: Generated acoustic wave amplitudes in copper, compensated for optical reflectivity. 99
Figure 6.18: Imaginary part of the dielectric constant for copper. 100
Figure 6.19: Optical penetration depth of radiation in copper as a function of wavelength. 100
Figure 6.20: Reflectivity of silicon in vacuum. 101
Figure 6.21: Peak to peak amplitude representation of acoustic waves generated in a silicon wafer at three optical wavelengths and varying pulse energies. 102
Figure 6.22: Generated acoustic wave amplitudes in silicon, compensated for optical absorption. 103
Figure 6.23: Reflectivity, reflectance, absorption and transmission on silicon in vacuum. 103
Figure 6.24: Optical penetration depth of silicon. 104

Figure 6.25: Peak to peak amplitude representation of acoustic waves generated in a silicon wafer with an aluminium film at three optical wavelengths and varying pulse energies. 106
Figure 6.26: Generated acoustic wave amplitudes in silicon with an aluminium film, compensated for optical absorption........ 106
Figure 6.27: Peak to peak amplitude representation of acoustic waves generated in a silicon wafer with a chromium film at three optical wavelengths and varying pulse energies. 107
Figure 6.28: Generated acoustic wave amplitudes in silicon with a chromium film, compensated for optical absorption........ 107
Figure 6.29: Peak to peak amplitude representation of acoustic waves generated in a silicon wafer with a copper film at three optical wavelengths and varying pulse energies. 108
Figure 6.30: Generated acoustic wave amplitudes in silicon with a copper film, compensated for optical absorption........ 108
Figure 6.31: Comparison of acoustic generation efficiency, comparing the three thin films, Al, Cr and Cu on a silicon substrate to that of a blank silicon wafer at 1064 nm. 111
Figure 6.32: Comparison of acoustic generation efficiency, comparing the three thin films, Al, Cr and Cu on a silicon substrate to that of a blank silicon wafer at 532 nm. 111
Figure 6.33: Comparison of acoustic generation efficiency, comparing the three thin films, Al, Cr and Cu on a silicon substrate to that of a blank silicon wafer at 355 nm. 112
Figure 6.34: Acoustic bulk waves generated in silicon and silicon with an aluminium thin film. 114
Figure 7.1: Time frequency analysis splits the time domain waveform into overlapped windowed sections before performing an FFT on them [7]. 121
Figure 7.2: Lamb wave measured in 50 µm silicon wafer. 122
Figure 7.3: Bandpass filtered Lamb wave........ 123
Figure 7.4: Spectrogram obtained using a narrow time window. 124

Figure 7.5: Spectrogram obtained using a wide time window. 124
Figure 7.6: Realistic spectrogram of Lamb wave. 125
Figure 7.7: The three windows used for reassignment, (a) the normal Hanning window, (b), the time derivative window and (c) the time ramped window.. 126
Figure 7.8: Reassigned spectrogram of Lamb wave. 127
Figure 7.9: MEMS pressure sensor on wafer with test point highlighted. 129
Figure 7.10: MEMS pressure sensors mounted in position. 129
Figure 7.11: Experimental set up for the measurement of high frequency acoustic waves in silicon wafers and MEMS pressure sensors. Components shown are, (a) - Michelson interferometer, (b) - UV laser, (c) - translation stage, (d) - stabilisation circuit and (e) – trigger photodiode. 130
Figure 7.12: Variation in group velocity dispersion curve with increasing sample thickness. E = 169 GPa, υ = 0.36, G = 79.6 GPa. h = (50 µm, +1%, +5%, +10%). 133
Figure 7.13: Variation in group velocity dispersion curve with decreasing sample thickness. E = 169 GPa, υ = 0.36, G = 79.6 GPa. h = (50 µm, -1%, -5%, -10%). 133
Figure 7.14: Variation in time frequency dispersion curve with increasing sample thickness. E = 169 GPa, υ = 0.36, G = 79.6 GPa. h = (50 µm, +1%, +5%, +10%). 134
Figure 7.15: Variation in time frequency dispersion curve with decreasing sample thickness. E = 169 GPa, υ = 0.36, G = 79.6 GPa. h = (50 µm, -1%, -5%, -10%). 134
Figure 7.16: Variation in group velocity dispersion curve with increasing Young's modulus. h = 50 µm, υ = 0.36, G = 79.6 GPa. E = (169 GPa, +1%, +5%, +10%). 135
Figure 7.17: Variation in group velocity dispersion curve with decreasing Young's modulus. h = 50 µm, υ = 0.36, G = 79.6 GPa. E = (169 GPa, -1%, -5%, -10%). 136

Figure 7.18: Variation in time frequency dispersion curve with increasing Young's modulus. h = 50 µm, υ = 0.36, G = 79.6 GPa. E = (169 GPa, +1%, +5%, +10%). 136
Figure 7.19: Variation in time frequency dispersion curve with decreasing Young's modulus. h = 50 µm, υ = 0.36, G = 79.6 GPa. E = (169 GPa, -1%, -5%, -10%). 137
Figure 7.20: Variation in group velocity dispersion curve with increasing Poisson's ratio. E = 169 GPa, h = 50 µm, G = 79.6 GPa. υ = (0.36, +1%, +5%, +10%). 138
Figure 7.21: Variation in group velocity dispersion curve with decreasing Poisson's ratio. E = 169 GPa, h = 50 µm, G = 79.6 GPa. υ = (0.36, -1%, -5%, -10%). 138
Figure 7.22: Variation in time frequency dispersion curve with increasing Poisson's ratio. E = 169 GPa, h = 50 µm, G = 79.6 GPa. υ = (0.36, +1%, +5%, +10%). 139
Figure 7.23: Variation in time frequency dispersion curve with decreasing Poisson's ratio. E = 169 GPa, h = 50 µm, G = 79.6 GPa. υ = (0.36, -1%, -5%, -10%). 139
Figure 7.24: Measured Lamb wave generated in MEMS pressure sensor. 141
Figure 7.25: Measured data after bandpass filter between 5 MHz and 250 MHz is applied. 141
Figure 7.26: Reassigned Gabor time-frequency representation on the detected Lamb wave measured in the MEMS pressure sensor membrane. Also showing measured signal and energy spectral density. 142
Figure 7.27: Reassigned Gabor time-frequency representation on the detected Lamb wave measured in the MEMS pressure sensor membrane. 143
Figure 7.28: Low frequency S_0 and A_0 modes. 144
Figure 7.29: Onset of Rayleigh wave. 145
Figure 7.30: FFT of measured signal. S1 mode is visible at ≈120 MHz. (Signal bandpass filtered between 100 MHz and 150 MHz). 147

Figure 7.31: Modelled wavenumber, phase velocity and group velocity dispersion curves for the S_1 (green) and S_2 (magenta) modes using material property estimates for MEMs pressure sensor. 148
Figure 7.32: Measure S_1 mode approaching zero group velocity. 149
Figure 7.33: Measured and theoretical time-frequency dispersion curve for MEMS pressure sensor membrane. Solid lines refer to the antisymmetric modes and dashed lines refer to the symmetric modes................................... 151
Figure 7.34: Measured and theoretical group velocity dispersion curve for MEMS pressure sensor membrane. Solid lines refer to theoretical dispersion curves and crosses show the measured points..................................... 152
Figure 8.1: Cross-section of MEMS pressure sensor membrane (×37 magnification). 157
Figure 8.2: Cross-section of MEMS pressure sensor membrane (×950 magnification). 157
Figure 8.3: Experimental setup to measure the infrared transmission of the MEMS pressure sensor. 159
Figure 8.4: Sellmeier equation for the wavelength range 1530 nm to 1610 nm...... 160
Figure 8.5: Transmission spectrum for the MEMS pressure sensor. 161

Nomenclature

This thesis covers more than one major topic including optics, elasticity, and signal processing. Many symbols used in each of these areas are shared in the literature, for example λ could refer to optical wavelength or acoustic wavelength, or k could be the extinction coefficient in optics or the wave number in elasticity. Due to this, the terms presented below is listed per chapter.

Chapter 2

υ	Poisson's Ratio
E	Young's modulus
E^*	Indentation modulus of surface

Chapter 3

I	Optical intensity
I_0	Intensity at material surface
α	Absorption coefficient
x	Propagation distance into material
δ	Skin depth
σ	conductivity
μ_r	Relative permeability of the metal
μ_0	Permeability of free space
f	Frequency of incident radiation
k	Extinction coefficient
λ_{opt}	Optical wavelength
D_{th}	Thermal diffusion length
κ	Thermal conductivity
ρ	Material density
c_p	Specific heat
f_{mod}	Modulation frequency

T	Temperature
c_{th}	Thermal wave speed
Q	Heat source
t	Time
x_1, x_2	x and y spatial dimensions
x_3	Depth (z spatial dimension)
t_0	Laser pulse rise time
r_0	Laser beam spot radius
Φ_T	Volumetric expansion
λ, μ	Lamé constants
α_T	Coefficient of thermal expansion
B	Bulk modulus

Chapter 4

φ	Optical phase
d	Surface displacement
λ	Optical wavelength
V	Detector output
V_0	Amplitude of interference
I_D	Intensity on photodetector
I_R	Intensity of reference beam
I_S	Intensity of signal beam
i_s	Photocurrent signal
i_n	Photocurrent Noise
P	Laser power from sample incident on photodetector
η	Quantum efficiency of photodetector
B	Detection frequency bandwidth
$h\upsilon$	Energy of quanta of light
U_{min}	Minimum detectable displacement

Chapter 5

d	Plate thickness
h	$d/2$
k	wavenumber
ω	Angular frequency
c_p	Phase velocity
f	Frequency
C_L	Longitudinal velocity
C_T	Transverse velocity
λ, μ	Lamé constants
E	Young's modulus
ρ	Material density
υ	Poisson's ratio
c_s	Plate velocity
C_R	Rayleigh velocity

Chapter 6

ϵ	Dielectric constant
ϵ_1	Real part of dielectric constant
ϵ_2	Imaginary part of dielectric constant
i	$\sqrt{-1}$
n	Real part of complex refractive index
k	Imaginary part of complex refractive index (extinction coefficient)
N	Complex refractive index
R	Reflectivity
α	Absorption coefficient
λ	Optical wavelength
δ	Skin depth
ω_p	Plasma frequency
N_e	Material electron density
q	Electronic charge

m_e	Mass of electron
ε_0	Permittivity of free space
x_3	Depth (z spatial dimension)
υ	Poisson's ratio
l	Acoustic source width
$\frac{d\varepsilon_g}{dP}$	Pressure dependence of bandgap
Δn	Excess charge carriers

Chapter 7

$STFT$	Short time Fourier transform
S	Spectrogram
$x(\tau)$	Original signal
ω	Frequency, frequency coordinate
t	Time, time coordinate
$h(\tau\text{-}t)$	Window function
i	$\sqrt{-1}$
E	Energy density spectrum
σ_t	Standard deviation for time
σ_ω	Standard deviation for frequency
$\hat{t}$	Time reassigned coordinate
$\Re$	Real part
$S_{\tau h}$	STFT using time ramped version of the window
S_h	Standard STFT
$\widehat{\omega}$	Frequency reassigned coordinate
$\Im$	Imaginary part
S_{Dh}	First derivative of window function
c_g	Group velocity
d	Source – detector separation distance
E	Young's modulus
υ	Poisson's ratio
G	Shear modulus

c_s	Plate velocity
ρ	Material density
δh	Thickness sensitivity
h	Thickness
δf	Group velocity frequency shift
f	Group velocity frequency
C_R	Rayleigh velocity
C_T	Transverse velocity

Chapter 8.

$\Delta \upsilon$	Free spectral range (waveneumber)
c	Speed of light in vacuum
n	Real part of refractive index
d	Sample thickness
$\Delta \lambda$	Free spectral range (wavelength)
λ	Optical wavelength

1 Introduction

1.1 Why characterise the MEMS pressure sensor?

In the technological world, silicon has been at the fore front of the semiconductor industry since the 1940s. More recently, since the 1980s, it has proved its versatility again, this time as a mechanical material in the development and production of microelectromechanical systems (MEMS). This was achieved by adapting the tool set developed for Very Large Scale Integration (VLSI). Silicon is a very attractive material as mechanical structures can also incorporate electronic functions. When considering the mechanical properties of any material, there are 3 main categories [1]:

- elastic properties
- inelastic properties
- strength

Knowledge of the elastic properties is needed to be able to predict how much deflection there will be when a force is applied to a material or vice versa. If it is desired that the material is to be permanently deformed, then knowledge of the inelastic properties is necessary and finally, knowledge of the strength of the material is needed so that the permitted operating limits can be determined.

One of the early pioneers in the field of MEMS research, Richard Muller, in 1990 stated "*Research on the mechanical properties of the electrical materials forming microdynamic structures (which previously had exclusively electrical uses), on the scaling of mechanical design, and on the effective use of computer aids is needed to provide the engineering base that will make it possible to exploit fully this technology*" [2]. Later, recommendations were made in another report [3] to the National Research Council committee of which Muller was chair. One conclusion

was "*Test and characterisation methods and metrologies are required to (1) help fabrication facilities define MEMS materials for potential users, (2) facilitate consistent evaluations of material and process properties at the required scales, and (3) provide a basis for comparisons among material fabricated at different facilities*". The recommendation to achieve this was given as "*Standard test methods, characterization methods, and test devices should be developed and disseminated that are suitable for the range of materials and processes of MEMS. Ideally, metrology structures will be physically small, simply designed, easily replicated, and conveniently and definitively interrogated. MEMS engineering standards should be similar to those already established for materials and devices in conventional sizes by organizations such as the National Institute of Standards and Technology (NIST), the American Society for Testing and Materials (ASTM), and the Institute of Electrical and Electronics Engineers (IEEE). This recommendation calls for new strategic investment*". With respect to characterizing MEMS materials, the author wrote "*The characterization and testing of MEMS materials should be an area of major emphasis. Studies that address fundamental mechanical properties (e.g., Young's modulus, fatigue strength, residual stress, and internal friction) and the engineering physics of long-term reliability, friction, and wear are vitally needed. It is important that these studies take into account fabrication processes, scaling, temperature, operational environment (i.e., vacuum, gaseous, or liquid), and size dependencies. Studies of the size effects of physical elements, on a scale comparable to the crystallite regions in a polycrystalline material, are required. This recommendation calls for continuing strategic investment*".

According to the MEMS journal [www.memsjournal.com], MEMS pressure sensors are set to become the top selling MEMS device by 2014, overtaking the current top selling MEMS devices, accelerometers and gyroscopes. The automotive industry is the main driver for this increase and it is estimated that by 2014, revenue for MEMS pressure sensors will approach $2 billion.

The main applications of MEMS pressure sensors in the automotive industry are manifold air pressure sensors and common fuel rail pressure sensors for engine management systems and brake and tyre pressure sensors for safety systems. In the medical industry they are used in applications such as disposable devices for catheters employed in surgical operations and for pressure and differential flow monitoring in continuous positive airway pressure machines for treating sleep apnoea. The construction industries use MEMS pressure sensors in heating, ventilation and air conditioning while the aerospace industry uses the sensors to monitor engines, flaps and other functions and also to provide precision altitude air pressure measurement. Compared to the use of accelerometers and gyroscopes in consumer and mobile devices, MEMS pressure sensors have not been as successful, where their revenue is currently under $50 million. The use of pressure sensors during the next few years will remain very modest. The chart below shows the industry application for MEMS pressure sensors in 2011 [4].

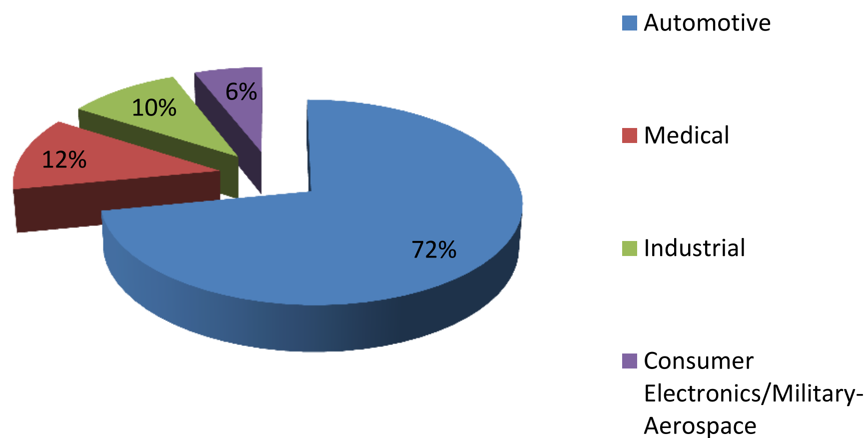

Figure 1.1: Industry applications of the MEMS pressure sensor.

1.2 Overview of thesis

The purpose of this thesis is to bring together the application of laser generated and detected ultrasound to generate Lamb waves in sub millimetre structures and detect

them using broadband optical detection instrumentation. This permits a non-contact examination of MEMS pressure sensor membranes. Lamb waves, while more commonly used for defect detection, are also extremely suitable for material characterisation and this thesis focuses on that. Laser generated Lamb waves are used to measure the membrane thickness of the pressure sensor and to obtain values of the material properties, Young's modulus and Poisson's Ratio.

This thesis presents a non-destructive, non-contact method of characterising a MEMS pressure sensor. It could be a rapid, in line with manufacture, method which, with a single measurement, could provide more information than the bulge test method currently used.

This thesis is composed of seven main chapters. The first four chapters cover the necessary background material for the thesis. Chapter 2 introduces the MEMS pressure sensor, and gives a review of current methods for testing and characterising MEMS devices, silicon wafers and thin films on a substrate. Chapter 3 investigates laser generated ultrasound while Chapter 4 looks at optically detected ultrasound. Chapter 4 also details the high bandwidth Michelson interferometer built to detect the acoustic waves. Finally, Chapter 5 gives an introduction to Lamb waves and elasticity in plates.

The last three chapters present the results from the research. Chapter 6 investigates the optical properties of silicon and various metallic thin films on silicon. Chapter 7 shows the advantages of using time-frequency analysis on a single detected Lamb wave in a MEMS pressure sensor to determine the membrane thickness and how this can be used to estimate the material properties, Young's modulus and Poisson's ratio. Finally, Chapter 8 verifies the membrane thickness using an alternative optical technique.

1.3 References

[1] W. N. Sharpe, “Mechanical Properties of MEMS Materials,” in The MEMS Handbook, M. Gad-el-Hak, Ed., CRC Press, 2002.

[2] R. S. Muller, “Microdynamics,” Sensors and Actuators A: Physical, vol. 21, no. 1-3, pp. 1-8, 1990.

[3] R. S. Muller, “Micromechanical Systems,” National Academy of Sciences, Washington, D.C., 1997.

[4] J. Bouchaud and R. Dixon, “MEMS Market Brief Volume 4 Issue 9,” IHS Technology, 2011. [Online].

2 The MEMS Pressure Sensor and Characterisation of MEMS Devices

2.1 Introduction

Microelectromechanical systems (MEMS) refer to devices that have dimensions that fall within the 1 μm to 1 mm range and combine electrical and mechanical components. The MEMS pressure sensor is an example of one such structure. With the continued growth of the MEMS industry, there is an ever increasing need to be able to measure the dimensions and material properties of these structures – both on the silicon wafers and the final pressure sensor membrane, not only to ensure reliability but also to improve future designs. One concern is that the material properties at the microscale can vary, in some instances by up to 20% compared to those of the bulk material. The work in this thesis was conducted on the membranes of pressure sensors etched into silicon wafers. Due to the potential rapidness of the test procedure, it could be possible to automate this as a test mechanism during the manufacturing process.

This chapter begins by giving a brief overview of the MEMS pressure sensor and also describes the sample that will be investigated within this thesis. The second part of the chapter looks at current methods employed to measure thickness and various material properties of MEMS structures, before ending with a list of some commercial measurement instruments currently available

2.2 The MEMS pressure sensor

The MEMS pressure sensor is considered one of the biggest successes of micromachining technology. Its applications are varied but are mainly concentrated in the automotive industry, where they are used in engine manifolds, exhausts, tyres, fuel lines and seats, and the biomedical industry, where applications include

implantable devices for measuring bowel, cranial or ocular pressure, and devices built into catheters that assist in procedures such as angioplasty [1]. Other applications include accelerometers and ink jet printer nozzles [2]. Two of the largest and most successful applications of the MEMS pressure sensor are used to measure manifold absolute pressure in passenger vehicles, critical in determining the airflow into an engine [3] and the medical pressure sensor, produced by GE Measurement & Control [4] used in applications such as medical instrumentation, blood pressure measurement, infusion pumps and kidney dialysis machines to name a few. Sanchez [5, 6] demonstrated the first solid state pressure sensor to use a diaphragm and large scale production of MEMS pressure sensors began in 1974 at National Semiconductor Corporation using borrowed technology from the integrated circuit industry [7]. With this existing technology, silicon became the material of choice as a structural material, because of its advantageous material properties. Silicon does not plastically deform and after the load is removed, returns to its original dimensions and tensions.

In the MEMS pressure sensor, as in all mechanical sensors, the sensing element will convert an external force, pressure, into an electrical signal. The electrical signal normally needs some further conversion to obtain a voltage, for example, a Wheatstone bridge may be used in a piezoresistive sensor or a charge amplifier may be used in a piezoelectric sensor. The work involving a MEMS pressure sensor, completed in this thesis was conducted on a piezoresistive pressure sensor supplied in wafer form by GE Measurement & Control[1]. This type of pressure sensor has four sensing elements in a Wheatstone bridge that measures strain within the thin silicon membrane. This is illustrated in Figure 2.1 and Figure 2.2, taken from [7]. The strain, and hence change in resistance is linearly proportional to the deflection of the membrane when a pressure differential is applied across the front and back sides of the sensor. The deflection is balanced by the elastic reaction force of the diaphragm

[1] It should be noted that as only the mechanical properties of the sensor were under investigation, the circuitry was irrelevant. A brief discussion with GE Measurement & Control revealed that the wafer came from a scrap bin, failing a quality check. The only known, with the wafer, was the metallic elements were a titanium tungsten aluminium alloy, indicating the sensor was manufactured for an aerospace application *i.e.* a high temperature application.

[6]. The membrane is typically edge supported, deflecting in response to a transverse pressure. The deflections are obviously dependant on the applied pressure, but are also proportional to the thickness of the membrane and Poisson's ratio and are inversely proportional to Young's modulus and thickness. Membrane deflections are typically around 1 μm. The membrane is the most critical component in a MEMS pressure sensor and having an optimal membrane is crucial to the sensor efficiency. A thin membrane will give a higher sensitivity and maximise the deflection. However if the deflection is large, nonlinear effects may result which are undesirable.

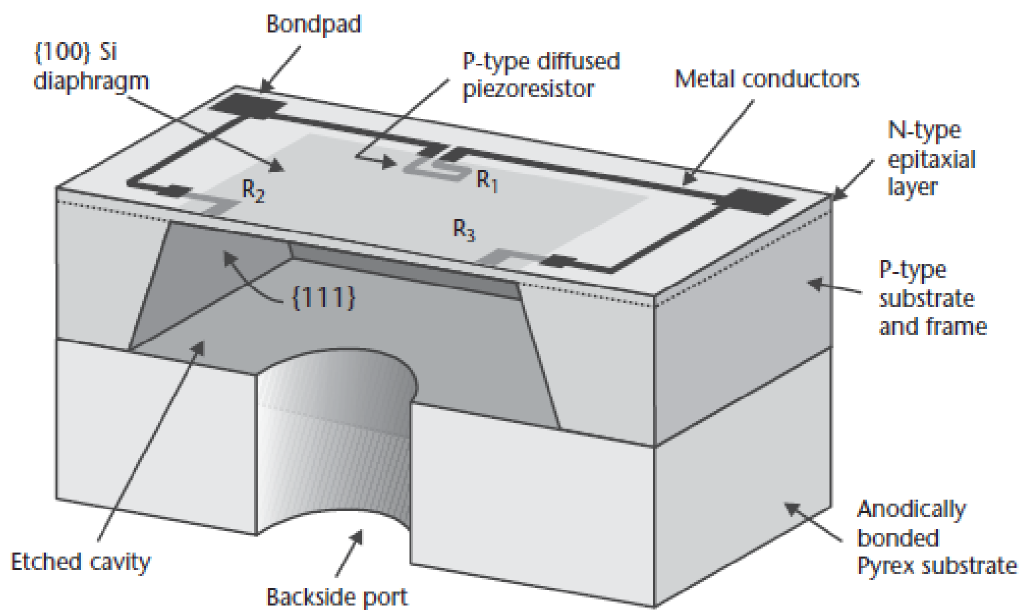

Figure 2.1: Schematic illustration of a pressure sensor with diffused piezoresistive elements. Overall dimensions are approximately 2 mm^2 and resistor R4 would be located opposite resistor R1 (section cut away).

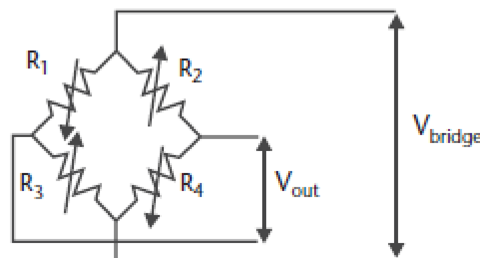

Figure 2.2: The four resistive elements form a Wheatstone bridge configuration.

MEMS pressure sensors are generally manufactured using anisotropic wet silicon etching, where potassium hydroxide etches the material parallel to the (111) plane, *i.e.* creating a 54.7° angle with the (100) plane as shown in Figure 2.3. The end diaphragm thickness is determined by the etch time. The geometrical design of the structure, that is, its dimensions and membrane thickness will affect the sensitivity of the device and as a result of this, the pressure sensing range of the device. The sensitivity is inversely proportional to the square of the membrane thickness and proportional to the membrane area [8, 9]. Devices designed to measure low pressures (less than 10 kPa) will tend to have more complex membrane structures such as central stiffening bosses, aimed at stiffening the centre of the membrane and concentrating the stresses near to the piezoresistive elements to improve sensitivity and linearity [7, 10].

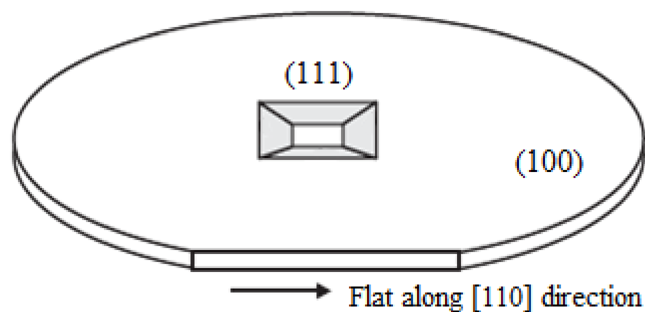

Figure 2.3: Effect of Potassium Hydroxide etchant on (100) plane of a silicon wafer to produce a membrane.

GE Measurement & Control used an electrochemical etch-stop technique to produce the structure, including stiffening boss. The stiffening boss is also hollow, adding less mass to the structure and helping reduce acceleration sensitivity. The cost of this however is an increase in die size. The pressure sensors used in this work contained one of these stiffening bosses and is shown in Figure 2.4 and Figure 2.5. The scanning electron microscope used to obtain these images is a Hitachi S-3000 SEM.

The MEMS pressure sensor is generally available in three different forms [11]:

- Absolute pressure sensors
- Gauge pressure sensors
- Differential pressure sensors

The output of the absolute pressure sensor is referenced to a vacuum, where the vacuum is created by sealing a cavity under the membrane. The gauge pressure sensor is referenced to atmospheric pressure. The differential pressure sensor comes in two variations. One compares two pressures input at each port on either side of the membrane, while another compares an input pressure to a reference pressure sealed within the device.

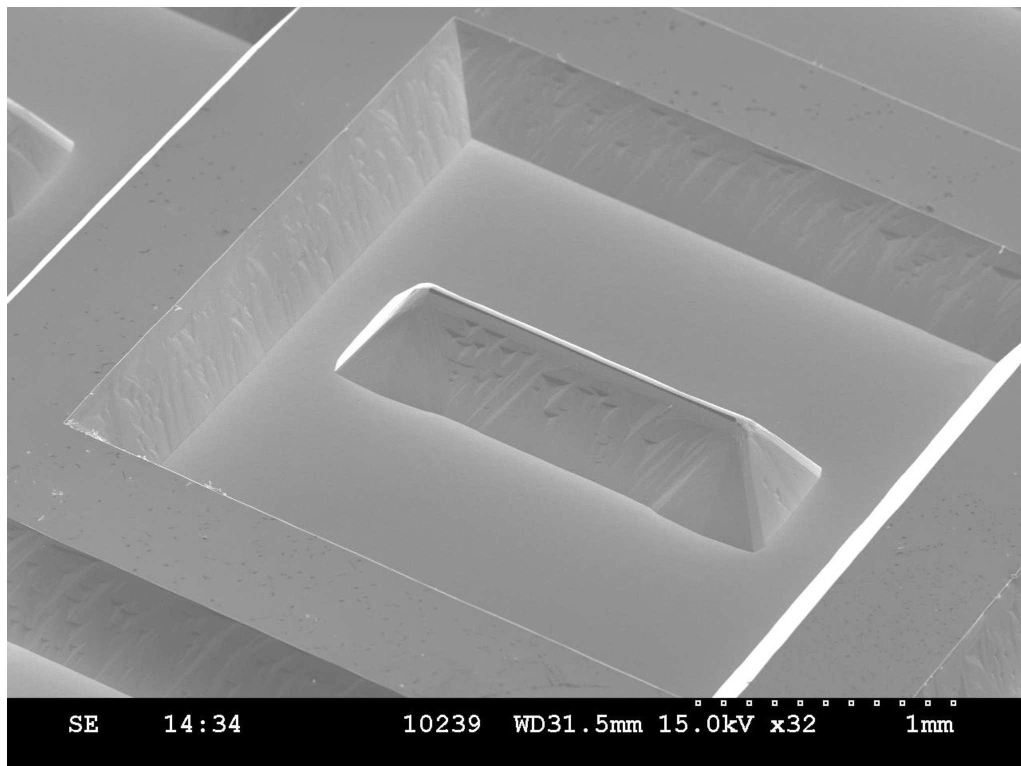

Figure 2.4: SEM image of MEMS pressure sensor.

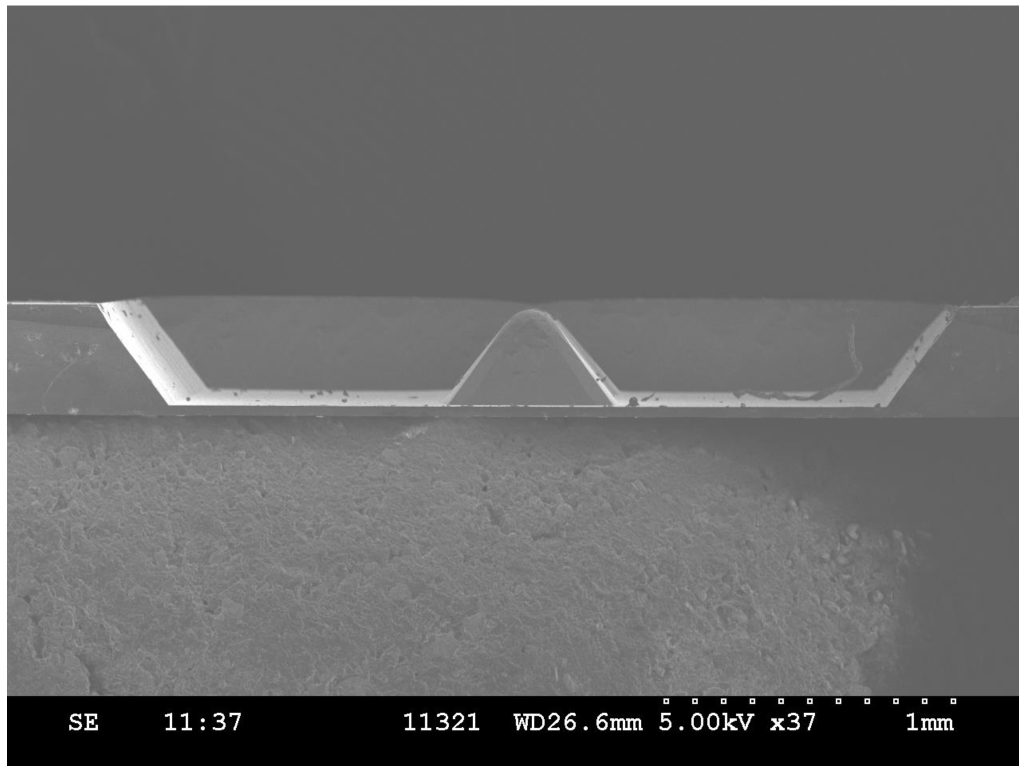

Figure 2.5: SEM image of MEMS pressure sensor, with one edge removed showing cross-section.

2.3 Current techniques for characterising MEMS sensors, thin films and silicon wafers

Along with the development of MEMS sensors, researchers have had to develop means of testing the structures and devices manufactured. Electrical testing provides information on the device functionality, but rarely gives an indication on the sensing elements' mechanical properties. Other than electrical testing, the main area of MEMS metrology is dimensional metrology. This can be either static measurements (Atomic Force Microscopy, Scanning Electron Microscopy, Optical Microscopy etc.) or dynamic measurements (Digital Holographic Microscopy or Laser Doppler Vibrometry) [12]. This is illustrated in Figure 2.6 [13] which shows that material property measurements come second to dimensional measurements in a recent survey illustrating important characteristics needed to be addressed.

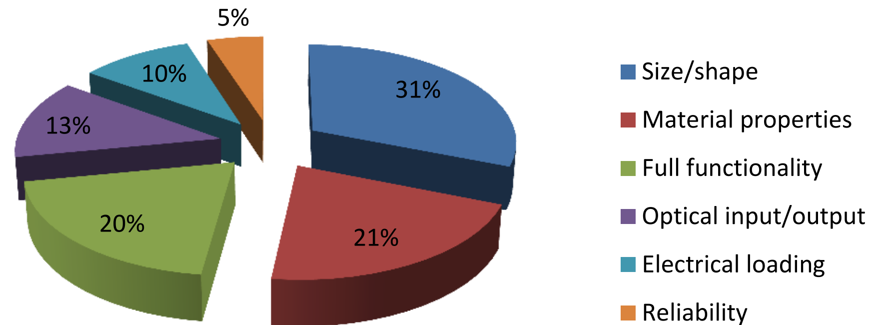

Figure 2.6: Outcome of recent survey on important characteristics needing addressed in MEMS sensors.

2.3.1 Characterisation of MEMS mechanical properties

2.3.1.1 Thickness measurements

Thickness of the membrane is probably one of the most critical parameters in a pressure sensor and this affects the amount of deflection and hence the range of applied pressure, and also the sensitivity of the device. SEMI, the association that serves the manufacturing supply chain for micro and nano electronics industries has published a method for testing thickness and thickness variation of silicon wafers [14]. Although this is not directly related to the thickness of a membrane, knowing the thickness of the wafer being etched is critical, to know how long the etchant should be applied for. The test method involves taking a measurement at the centre of the wafer followed by either four or eight other sites, with positions defined with respect to the primary flat or notch. If four test points (indicated by dark circles) are used, they are chosen to be equally spaced around the wafer, with the first at a 30° angle from the perpendicular to the flat. The diameter of the test points should be 6 mm from the edge of the wafer (Figure 2.7).

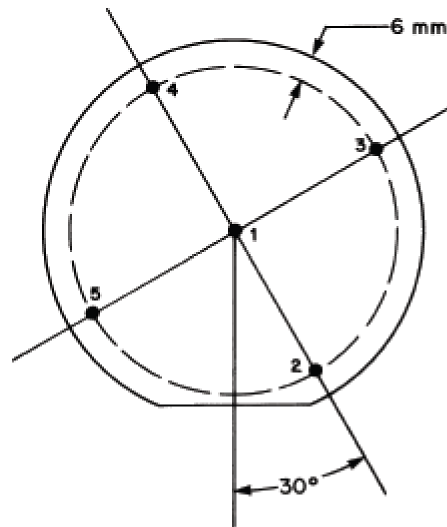

Figure 2.7: Sites for thickness measurement on wafers with flat.

If eight points are used, the first circle of points is taken, again, 6 mm from the edge of the wafer with the first point taken above the notch. The second circle of points is taken at a distance *R/2* from the centre, where *R* is the radius of the wafer. The instrument used to make the measurement should have a resolution of 2 µm and if it is a contact method, the probed area should not exceed 2 mm^2 as shown in Figure 2.8. If it is a non-contact method, the probed area should not exceed 130 mm^2. The thickness is determined from the centre point reading and the thickness variation is given as the maximum difference between any two of the thickness measurements.

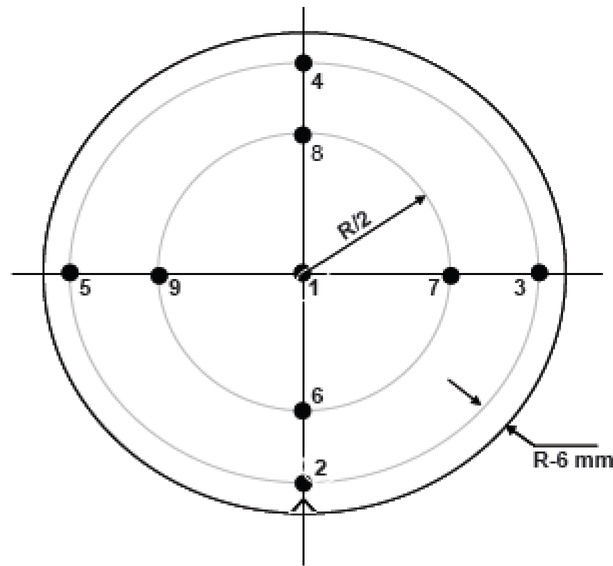

Figure 2.8: Sites for thickness measurement on wafers with notch.

Researchers have used a variety of methods to characterise thickness. Profunser *et al.* [15] used high frequency acoustic waves that travelled perpendicular to the membrane. The acoustic wave was generated with a 70 fs laser at a repetition rate of 81 MHz. With source and detector on the same face, they were able to monitor the reflections of the acoustic waves from the back face of the membrane as well as any discontinuities, *i.e.* boundaries caused by applied thin films. Schmitz *et al.* [16] used an infrared interferometer which produced a collimated wavefront to produce interference fringes between the between the front and back surfaces of a plane parallel silicon wafer.

2.3.1.2 Mechanical properties of MEMS

Knowing the mechanical properties of a material is critical to the design, manufacture and reliability of a sensor. One of the standard methods used for pressure sensor membranes and also for free standing thin films is the bulge test [17], [18]. Small and Nix [18] discussed the bulge test method from a theoretical/modelling viewpoint for a circular membrane and showed that the most important factors that need to be taken into consideration are the effects of the initial

conditions and experimental uncertainties. They also concluded that residual stress needs to be determined to obtain accurate results. Patil *et al.* [19] used an atomic force microscope to apply a controlled force *i.e.* pressure onto a pressure sensor membrane. The aim of their work was to characterise the electrical output of the sensor. However, this arrangement could have been extended to perform a bulge test. Zhang *et al.* [20] applied an external acoustic field propagating through air exciting the structure into resonance when the frequency of the acoustic field matched the resonant frequency of the structure. Vibration detection was via a heterodyne interferometer and values for Young's modulus and residual stress were determined. Residual stresses in membranes have also been characterised by Maseeh *et al.* [21] while Sato *et al.* [22] used tensile testing via bending through an applied load to determine fracture strain.

2.3.2 Commercially available equipment

Some companies, such as Lion Precision [23], Microsense [24], Fraunhofer Institute [25], NPL [6, 26], Polytec [27, 28] and Chapman Instruments [29] have developed testing equipment for this market. However, most of the research is conducted in academic environments. The list below outlines a selection of some of the measurement tools available and research being conducted.

2.3.2.1 Capacitive sensor for thickness measurements

A number of manufacturers (*e.g.* Lion Precision [23] and Microsense [24]) produce capacitive sensors for measuring thickness. This typically consists of a material being placed between a probe and a reference plate. The probe detects a change in capacitance as a result of the change in distance between the probe and the sample (the permittivity of the medium between sensor and sample (air normally) and the area of the sensor are also factors). The capacitance is proportional to the area of the sample and its dielectric constant and inversely proportional to the distance between them. If the sample is deformed in any way so the sample does not sit flat on the reference plate, an error is created. This can be eliminated by replacing the reference

plate with a second probe. Summing the two sensors gives a more accurate representation of thickness.

2.3.2.2 Nanoindentation and impact excitation

At NPL, Maxwell *et al*. [30] used impact excitation and nanoindentation to measure Young's modulus and Poisson's ratio of thin film coatings, and at the same time, Jennett *et al.* [31] used a combination of nanoindentation and acoustical methods to measure Young's modulus, Poisson's ratio and thickness of thin film coatings. Maxwell *et al.*, using impact excitation were able to determine a value for Young's modulus of TiN coatings of thickness 2.66 µm. Impact excitation is where the sample, supported by two thin wires a known distance apart (0.224l, where l is the length of the sample) at fundamental nodal points. Flexural vibrations are excited at the centre of the sample, using an automatic impulse. The vibrations are detected using a noncontact microphone at the end of the sample. From the fundamental frequency and all the harmonics generated, they showed that using Euler – Bernoulli theory, a value of Young's modulus could be obtained. This avoided using Poisson's ratio, which is a material dependant parameter. To obtain a value for Young's modulus, the measurement had to be performed on the substrate both before and after the titanium nitride had been sputtered onto it.

Using a nanoindentation technique, the indentation modulus was obtained. In this case, a diamond indenter, of known area and contact depth was pressed at varying loads and loading rates resulting in three different test forces being applied. By combining the values of Young's modulus, E and indentation modulus, E^*, a value for Poisson's ratio v was calculated using the following expression.

$$\nu = \sqrt{\left(1 - \frac{E}{E^*}\right)} \qquad \textbf{2.1}$$

Jennett *et al.* used the techniques described above, and went a step further by using acoustic methods to determine the thickness of the thin film coating using an LAwave SAW spectrometer. This is discussed in the following section.

2.3.2.3 LAwave SAW spectrometer

The LAwave system is a laser ultrasound based non-destructive testing instrument developed by the Fraunhofer Institute (Centre for Coatings and Laser Applications) [25]. It can be used for a variety of process development and quality control applications, including, Young's modulus measurement of ultra-thin (<5 nm) films, defect density monitoring of highly polished surfaces, monitoring of resistant coatings on machine tools and the monitoring of porosity and heat treated surfaces. References [32-36] show examples of specific applications of the LAwave system. The basic principle is illustrated below in Figure 2.9. The system comprises of two main components, an acoustic wave source in the form of a nitrogen laser (pulse duration – 0.5 ns, pulse energy – 0.4 mJ) and a piezoelectric film, pressed onto the sample surface with a small steel blade which acts as the detector. The laser is focused onto the surface using a cylindrical lens. Due to the short pulse duration, a broad spectrum of acoustic waves (surface acoustic waves) is generated. The high frequency waves have low penetration depths and while the penetration depth can be greater than the film thickness, the surface acoustic wave is sensitive to the mechanical properties of films with thicknesses considerably thinner than the penetration depth of the acoustic wave.

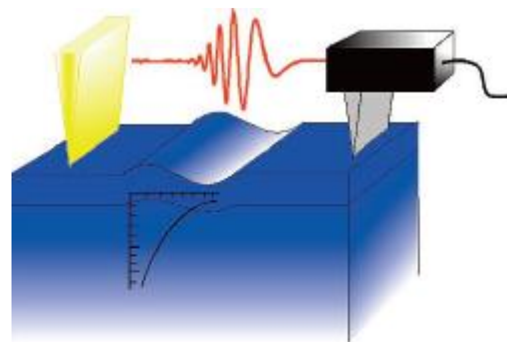

Figure 2.9: Basic operating principles of the LAwaves system [25].

The main purpose of this system is the measurement of thin film coatings using surface acoustic waves. In principle, there is no reason (other than dimensional) why this system cannot be used to generate and detect other types of acoustic waves, such as guided waves in thin plates or membranes, such as those found in a pressure sensor however, to date, no evidence of this is available.

2.3.2.4 Wafer thickness measurement using optical methods

Chapman Instruments [29] produce measurement equipment to measure all aspects of a wafer. This includes wafer thickness, total thickness variation, bow, warp, surface roughness and edge chip and crack. Measurements can be performed on a variety of materials such as silicon, germanium, indium phosphide and gallium arsenide. The measurement technique is optical, meaning it is non-contact and the capability of measuring wafers down to a thickness of 100 μm exists. The technique uses two focused laser beams, one on the top and one on the bottom of the sample. This arrangement measures wafer thickness, independent of material properties and wafer configuration

2.3.2.5 Vibrational measurements

Polytec [27, 28] are probably the largest manufacturer of laser vibrometers and as well as servicing the automotive, aerospace and civil engineering sectors, they also produce two products for MEMS characterisation. The first, the MSA-500 Micro System Analyser [27, 12] is an instrument for the analysis and visualisation of structural vibrations and surface topography in MEMS structures. The instrument is a microscope integrated with the following components:

1. Scanning laser Doppler vibrometer – used to measure out-of-plane motion. Automatic scanning can produce 3D animations of structure deflection.
2. Stroboscopic video microscope – to measure in-plane motion. Analysis of the planar direction provides 3D motion measurements.
3. Scanning white light interferometer – giving the capability of surface topography measurements for static shape.

The second Polytec vibrometer which shows considerable promise is the UHF-120 Ultra High Frequency vibrometer [28]. This is another microscope based product which moves away from Polytec's traditional bandwidth of 24 MHz and has been extended to 1.2 GHz. Unfortunately, there is no peer reviewed literature available on the performance or applications of this product, apart from the manufacturers datasheet, however, it is expected to produce promising results in the near future.

2.4 Conclusions

Since the development of MEMS structures and devices, there has been a need to be able to characterise them. The main issue is that the material properties are dependent on the fabrication route and the mechanical properties at the microscale can vary, in some instances by up to 20% compared to those of the bulk material. One of the biggest problems in characterisation is that a force of some kind must be applied to the device and this normally means a mechanical force acting on it. This contact can, and in most cases does, modify the surface, if not completely destroy the sample. The one limiting factor is that the sample needs to be mounted in some way and this generally is mechanical in nature. The commercial instruments described, do claim to be non-contact however, whether it is by capacitance or optical methods, they are only able to measure properties such as thickness, bow, warp etc., *i.e.* "surface properties". What is needed is a complete non-contact method that can not only measure thickness, but also the mechanical properties such as Young's modulus and Poisson's ratio. This requirement is met by the optically generated and detected ultrasonic Lamb wave method presented next.

2.5 References

[1] J. S. Park, C. Wilson and Y. B. Gianchandani, "Micromachined Pressure Sensors," in *The MEMS Handbook*, M. Gad-el-Hak, Ed., CRC Press, 2002.

[2] R. S. Muller, "Micromechanical Systems," National Academy of Sciences, Washington, D.C, 1997.

[3] W. S. Czarnocki and J. P. Schuster, “The evolution of automotive pressure sensors,” *Sensors,* vol. 16, no. 5, 1999.

[4] *NPC-100 Data sheet,* GE Measurement & Control.

[5] J. C. Sanchez, “Semiconductor strain gauge pressure sensors,” *Instruments and Control Systems,* pp. 117-120, 1963.

[6] S. P. Reilly, R. K. Leach, A. Cuenat, S. A. Awan and M. Lowe, “Overview of MEMS sensors and the metrology requirements for their manufacture,” NPL, 2006.

[7] N. Maluf and K. Williams, “MEM Structures and Systems in Industrial and Automotive Applications,” in *An Introduction to Microelectromechanical Systems Engineering*, 2nd Edition ed., Artech House, 2004.

[8] P. K. Kinnell, J. King, M. Lester and R. Craddock, “A hollow stiffening structure for low pressure sensors,” *Sensors and Actuators A: Physical,* vol. 160, pp. 35-41, 2010.

[9] P. K. Kinnell, J. King, M. Lester and R. Craddock, “A hollow stiffening structure for low pressure sensors,” in *Procedia Chemistry*, 2009.

[10] R. Frank, “Pressure sensors merge micromachining and microelectronics,” *Sensors and Actuators A,* vol. 28, pp. 93 - 103, 1991.

[11] “Kulite Semiconductor Products,” [Online]. Available: http://www.kulite.com/technology.asp.

[12] E. Lawrence, “Optical measurement techniques for dynamic characterisation of MEMS devices,” Polytec, 2012.

[13] Z. Cui, R. K. Leach and D. R. Flack, “Microsystems technology standardisation roadmap,” NPL, 2003.

[14] “Test Methods for Thickness and Thickness Variation of Silicon Wafers,” SEMI, 2010.

[15] D. M. Profunser, J. Vollmann and J. Dual, “Determintaion of the material properties of microstructures by laser based ultrasound,” *Ultrasonics,* vol. 42, pp. 641-646, 2004.

[16] T. L. Schmitz, A. Davies, C. J. Evans and R. E. Parks, “Silicon wafer thickness variation measurements using the National Institute of Standards and Technology infrared interferometer,” *Opt. Eng.,* vol. 42, no. 8, pp. 2281-2290, 2003.

[17] T. Yi and C. J. Kim, “Measurement of mechanical properties for MEMS materials,” *Meas. Sci. Tech.,* vol. 10, pp. 706-716, 1999.

[18] M. K. Small and W. D. Nix, “Analysis of the accuracy of the bulge test in determining the mechanical properties of thin films,” *J. Mater. Res.,* vol. 7, no. 6, pp. 1553-1563, 1992.

[19] S. K. Patil, Z. Celik-Butler and D. Butler, “Characterization of MEMS piezoresistive pressure sensor using AFM,” *Ultramicroscopy,* vol. 110, pp. 1154-1160, 2010.

[20] L. M. Zhang, D. Uttamchandani, B. Culshaw and P. Dobson, “Measurement of Young’s modulus and internal stress in silicon microresonators using a resonant frequency technique,” *Meas. Sci. Tech.,* vol. 1, pp. 1343-1346, 1990.

[21] F. Maseeh, M. A. Schmidt, M. G. Allen and S. D. Senturia, “Calibrated measurements of elastic limit, modulus and the residual stresses of thin films using micromachined suspended structures,” in *IEEE Solid-State Sensorand Actuator Workshop*, 1988.

[22] K. Sato, M. Shikida, T. Yoshioka, T. Ando and T. Kawabata, “Micro tensile test of silicon film having different crystallographic orientations.,” in *International Conference on Solid-State Sensors and Actuators.*, Chicago, 1997.

[23] “Lion Precision,” [Online]. Available: www.lionprecision.com.

[24] “Microsense,” [Online]. Available: www.microsense.net.

[25] Fraunhofer Institute, [Online]. Available: http://www.ccl.fraunhofer.org/download/LA_Wave.pdf.

[26] R. Leach and N. Jennett, *National Physical Laboratory (NPL), Private Communication.*

[27] Polytec, [Online]. Available: http://www.polytec-ltd.co.uk/uk/products/vibration-sensors/microscope-based-systems/msa-050-3d-micro-system-analyzer/.

[28] Polytec, [Online]. Available: http://www.polytec-ltd.co.uk/uk/products/vibration-sensors/microscope-based-systems/uhf-120-ultra-high-frequency-vibrometer/.

[29] Chapman Instruments, [Online]. Available: http://www.chapinst.com/ProductsMPT1000.htm.

[30] A. S. Maxwell, S. Owen-Jones and N. M. Jennett, “Measurement of Young's modulus and Poisson's ratio of thin coatings using impact excitation and depth-sensing indentation,” *Review of Scientific Instruments,* vol. 75, no. 4, pp. 970 - 975, 2004.

[31] N. M. Jennett, G. Aldrich-Smith and A. S. Maxwell, “Validated measurement of Young’s modulus, Poisson ratio, and thickness for thin coatings by combining instrumented nanoind,” *J. Mater. Res,* vol. 19, no. 1, pp. 143 - 148, 2004.

[32] D. Schneider and M. D. Tucker, “Non destructive characterization and evaluation of thin films buy laser induced ultrasonic surface waves,” *Thin Solid Films,* Vols. 290 - 291, pp. 305 - 311, 1996.

[33] D. Schneider and T. Schwarz, “A photoacoustic method for characterising thin films,” *Surface and Coatings Technology,* vol. 91, pp. 136 - 146, 1997.

[34] D. Schneider, T. Witke, T. Schwarz, B. Schoneich and B. Schultrich, “Testing ultra thin films by laser acoustics,” *Surface and Coatings Technology,* vol. 126, pp. 136 - 141, 2000.

[35] F. Atchison, T. Brys, M. Daum, P. Fierlinger, A. Foelske, M. Gupta, R. Henneck, S. Heule, M. Kasprzak, K. Kirch, R. Kotz, M. Kuzniak, T. Lippert, C.-F. Meyer, F. Nolting, A. Pichlmaier, D. Schneider, B. Schultrich, P. Siemroth and U. Straumann, “Structural characterization of diamond like carbon films for ultracold neutron applicaions,” *Diamond and Related Materials,* vol. 16, pp. 334 - 341, 2007.

[36] I. Jansen, D. Schneider and R. Hassler, “Laser acoustic, thermal and mechanical methods for investigations of bond lines,” *International Journal of Adhesion and Adhesives,* vol. 29, pp. 210 - 216, 2009.

3 Generation of Elastic Waves using Laser Pulses

3.1 Introduction

The optical generation and detection of ultrasound has become a very useful tool in both academia and industry for the study of material characteristics and defect detection and location. The ability to be able to interrogate material properties, especially from a distance, has found many applications in industries such as engineering [1-7] and aerospace [8-12]. With an increasing demand for smaller products and the accelerating development of MEMS and nano-technological devices, ultrasonic testing is becoming increasingly useful. The characterisation of thin structures such as thin films, layers or thin films on substrates can be carried out, by first obtaining dispersion curves followed by using an inversion process, to obtain material properties. The most common laser used in modern generation schemes is the Nd:YAG laser operating at 1064 nm.

The focus of this chapter is to introduce the principles of laser generated ultrasound and show how material properties, such as reflectivity and optical absorption can influence the generation of acoustic waves. The chapter finishes with a short overview of the photostrictive generation of acoustic waves.

3.2 Laser generated ultrasound

Using light to generate sound waves can be traced back as early as 1881 [13] where Alexander Graham Bell showed that by mechanically chopping sunlight incident on a thin metal disk, among other materials, could make the material emit a low audible sound. It wasn't until the 1960's that the concept of using electromagnetic radiation to generate elastic waves became a proper area of research in its own right. The founding of this line of research can be attributed to White, who published two journal papers showing that it was possible to generate elastic stress waves in a

material using a thermal mechanism, rather than radiation pressure [14, 15]. White stated that although a time varying incident energy on an elastic surface could produce a stress wave, a more efficient thermal mechanism can be used to produce an elastic wave if a pulsed source is used. With the advent and continued development of the laser, pulsed lasers have become common place in laser ultrasonic experiments.

The subject of laser generated ultrasound has been extensively reviewed, with the most comprehensive review being published by Scruby and Drain [1]. With continued research, a large number of papers were published describing the processes involved in laser generated ultrasound. Davies *et al.* produced a review article [16] that describes in detail three generation regimes: the thermoelastic regime, the ablation regime and the constrained surface regime. They go on to detail some experimental investigations and finish with applications of laser generated ultrasound. Table 2 listed in [16] summarises the authors, laser properties and aim of investigations. To generate acoustic waves using light, in most cases a pulsed laser source is required, however Pierce *et al.* published a review of work conducted at the University of Strathclyde outlining an alternative method to pulsed lasers using low power cw lasers to generate acoustic waves [17].

3.3 Advantages and disadvantages of laser based ultrasonic systems

Scruby published a review of possible applications of laser generated ultrasound [18]. He stated that "*laser ultrasonic techniques are only likely to find industrial application where they answer a need that cannot be met by conventional transducers, for instance deployment at elevated temperatures, where access is limited or where exceptionally high spatial or temporal resolution is called for*". Before discussing the application of laser ultrasound, the features and drawbacks of a laser ultrasound system are laid out. Figure 3.1 shows the laser generation and detection scheme developed for this thesis. The components are as follows:

a) Large bandwidth Michelson interferometer (200 MHz)
b) Vertical sample mount (samples held with magnetic tape)
c) 800 Hz stabilisation circuit
d) 355 nm laser, mounted on translation stage
e) Trigger circuit

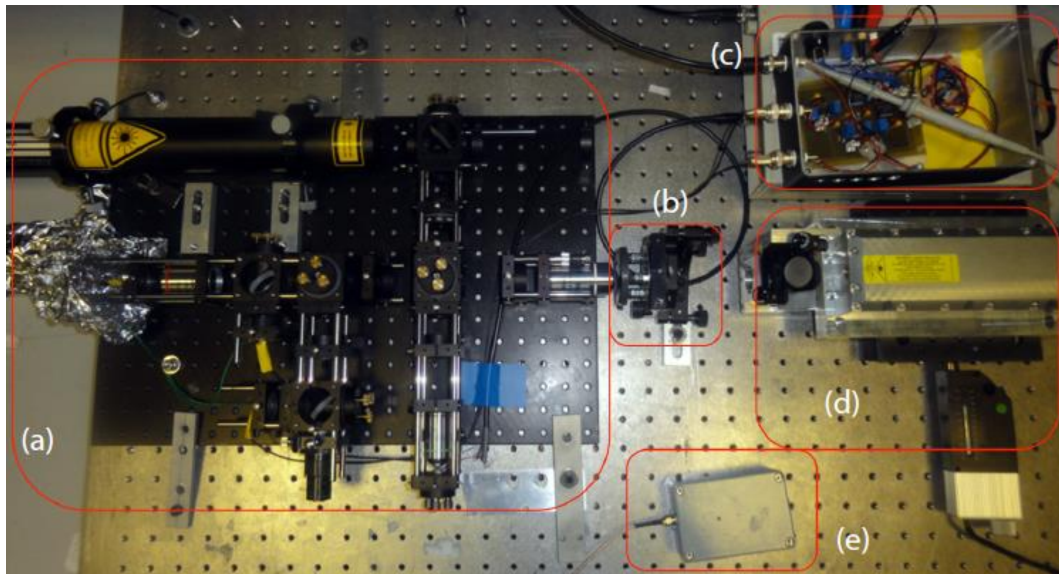

Figure 3.1: Laser based system used in this thesis.

Non-contact

Both generation and detection beams are incident on the surface of the material. No coupling medium is needed as the generation beam couples directly into the conduction electrons in the surface of the material. By not using a couplant, there are no intensity variations due to the couplant however, the incident laser beam may itself have intensity variations from pulse to pulse [19]. The sample is also free from mechanical loading. While it is fair to say there is no mechanical loading when the sample is a large plate for example with source and detector beams separated by large numbers of millimetres, is this case true for a very small structure where radiation pressure from both the source and detector beams and thermal spreading from the detector beam could influence the measurement? Radiation pressure is

typically several orders of magnitude smaller than thermoelastic effects and can be ignored [1].

Remoteness

If the source of the acoustic waves is defined as the laser, rather than the strain field induced by the laser, then it can be said that a laser ultrasound system is remote and both generation beams and detection beams can be located centimetres to metres from the surface. This is important in applications where the sample is hot or the beams must travel through a glass window into a sealed chamber where the environment may be hostile or contain high levels of radiation. Two perfect examples of this is where Matsuda *et al.* [20] and Vedantham *et al.* [2, 3] used laser ultrasonics to measure velocity and temperature and thickness respectively while the silicon wafers were being heated. Also, with the advantage of remoteness comes the possibility of automating the system too, for example, scan multiple components in a test cell [21].

High Bandwidth

Very high bandwidths are now attainable, where Q-switched solid state lasers (such as a Nd:YAG laser) are able to produce optical pulses of 0.5 ns which will produce acoustic waves at frequencies into the 100's MHz. Likewise, detection schemes can have a flat response over a very large bandwidth, with the upper limit dictated by the detection electronics, amplifiers etc, and the lower limit dictated by the background stabilisation electronics. This makes optically generated and detected ultrasound ideal for characterising layered structures and defect detection and sizing.

High Spatial Resolution

In principle, both the generation and detection beams used can be focused to diffraction limited spots. While this has a distinct advantage for an interferometer, the same cannot be said for the generation beam. Focusing this beam to tighter and tighter spots will result in an increase in the power density incident on the surface. The resultant of this is the production of a plasma on the surface of the material,

known as the ablation regime, which ultimately damages the surface. Dixon *et al*. [22] however used the formation of a plasma to non-destructively produce acoustic waves. They achieved this by focusing the laser beam onto a dummy target, placed a few millimetres in front of the test sample. The plasma expanded away from the dummy target and impacted on the test sample generating the acoustic wave. An increase in high spatial resolution can increase the accuracy of defect location and sizing.

Other advantages of laser generated ultrasound are good access to hard to reach areas, mainly with the use of mirrors and optical fibres and taking advantage of the small spot sizes of both generation and detection beams, and rapid scanning using prisms and mirrors. This can be a major advantage over piezoelectric probes as light has zero inertia and there is no viscous drag from any couplant.

Like any measurement system, there are going to be disadvantages compared to other competing systems and laser ultrasound systems are no different.

Sensitivity

When comparing amplitudes of ultrasonic waves created by laser systems to those produced by broadband piezoelectric probes, the laser generated waves are only slightly lower in amplitude. The problem with sensitivity comes from the optical detection side of the equation and this will be described in Chapter 4.

Surface Finish

Like sensitivity, surface finish is a material characteristic that is more of a problem with laser detection than generation. Indeed, a rough or dirty surface can in fact enhance the strength of the source, whereas a highly polished surface will reflect most of the energy.

Other disadvantages include expense, where laser systems are much more expensive than piezoelectric transducers, complexity in setting up laser generation and

detection schemes, size of complete systems and most importantly, where lasers are capable of causing tissue and eye damage.

Most of the work in this subject has been applied to isotropic materials, such as metals, but recently there has been an increase in interest in composites and semiconducting materials

3.4 Mechanisms of thermoelastic laser generated ultrasound

3.4.1 Optical absorption in metals

When light, from a coherent monochromatic source is incident on the surface of a material, normal to the surface of that material, some of the light is reflected, and the rest is absorbed. In certain cases, depending on the material's optical properties, and laser wavelength, some of the light is transmitted, however, for the purpose of generating ultrasonic waves, materials (where possible) and laser wavelengths must be chosen that forbid this criteria.

When considering the optical properties of materials in terms of laser generated ultrasound, there are three important parameters: the refractive index, n, the extinction coefficient, k, and the reflectivity, R. The refractive index is the ratio of the phase velocity of propagation of an electromagnetic wave of a given wavelength (hence frequency) in vacuum to that in the material. The extinction coefficient is a measure of the electromagnetic wave energy in the process of propagation through the material and is an exponential decay. It should be noted that these constants are functions of wavelength and temperature. Reflection of an electromagnetic wave from a surface depends on the complex refractive indices of the two media making up the interface of the reflected surface. In other words, it is a ratio of the intensity of the wave reflected back into the first medium to the intensity of the wave approaching the interface [23]. For all the work presented in this thesis, the first medium is air, with a refractive index $n \approx 1$ and all work is carried out at normal incidence. After propagating a distance, x into a material, the intensity I of the wave can be given as

$$I = I_0 e^{-\alpha x} \quad \textbf{3.1}$$

where the intensity I_0 is the intensity at $x=0$ and α is the absorption coefficient.

The light propagating into a metal is attenuated by $1/e$ when it has travelled a distance known as the skin depth. The skin depth, δ is given as

$$\delta = \sqrt{\pi \sigma \mu_r \mu_0 f} \quad \textbf{3.2}$$

where σ is the conductivity, μ_r is the relative permeability of the metal, μ_0 is the permeability of free space and f is the frequency of the radiation incident on the metal surface. For metals is typically 10s nm at visible wavelengths [1]. The absorption of light into the metal will increase with temperature. Conductivity will decrease with temperature as does the reflection coefficient, so as the temperature rises, more energy is absorbed [24].

3.4.2 Optical absorption in semiconductors

In a semiconductor, the absorption of light results in the excitation of a valence band electron to the conduction band. To be absorbed, the energy of the light must be greater than the bandgap, 1.12 eV for silicon. Light with energy below this value will be transmitted, for example, silicon is transparent to light at 1550 nm (0.8 eV).

The optical absorption, in most cases, is proportional to the thickness and the intensity of the light varies within the material. The absorption coefficient is given as

$$\alpha = \frac{4\pi k}{\lambda_{opt}} \quad \textbf{3.3}$$

where k is the extinction coefficient and λ_{opt} is the optical wavelength.

In semiconductors, the skin depth is given by

$$\delta = \frac{1}{\alpha} \tag{3.4}$$

Again, this is the distance after which the intensity has been reduced by $1/e$. At high photon energies compared to the bandgap, the skin depth is very short (≈10 nm at 355 nm wavelength) compared to lower energies (≈500 µm at 1064 nm wavelength) for silicon.

No engineering material will be perfectly flat, so does surface roughness effect reflectivity? Since the reflectivity is dependent on refractive index, the short answer is no, surface roughness has no effect. However, it does change the ratio of specular reflection to diffuse reflection. This turns out to be a double edged sword in terms of laser ultrasound. On the one hand, a surface that is as flat, clean and polished as possible is desired to maximise the return beam in a laser interferometer. However, if the surface of the sample under interrogation is rough, this can lead to an increase in energy used to form the acoustic signal, ideal from the elastic wave generation point of view. The reflectivities[2] of the metals and semiconductors studied in this thesis are shown in Figure 3.2 with values given for the fundamental, second and third harmonics of an Nd:YAG laser.

[2] The optical, thermal and mechanical properties used within this thesis are taken from, or calculated from values given in [23], unless stated otherwise.

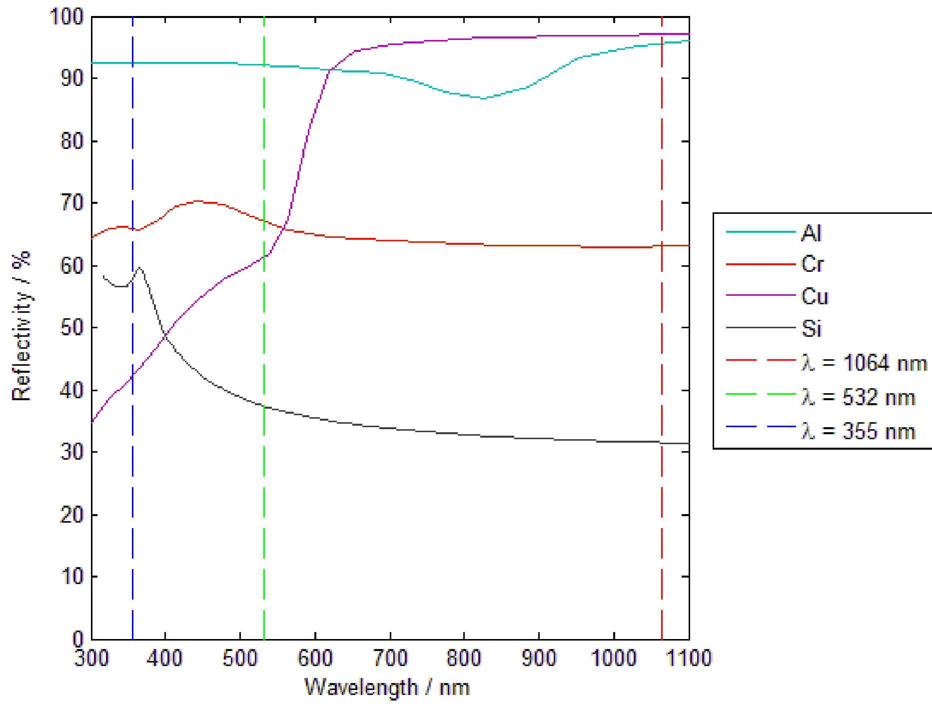

Figure 3.2: Optical reflectivity of the metals and semiconductors under investigation.

3.5 Heating through optical absorption

As described by equation 3.1, light penetrates into the material to a depth dependent on those materials' properties. The absorbed energy or power density is dictated by the reflectivity of the surface and the pulse duration. Increasing the pulse duration will result in a lower temperature rise on the surface of the material. The energy absorbed E_{ab} by the material is of the form $E_{ab} = E_{pulse}(1 - R)$, where E_{pulse} is the pulse energy and R is the reflectivity. Through electron – phonon interactions, the absorbed energy is converted to heat and this "heat source" propagates into the material to a depth known as the thermal diffusion length [17]. The thermal diffusion length, D_{th}, is given as

$$D_{th} = \sqrt{\left(\frac{\kappa}{\rho c_p f_{mod}}\right)} \qquad \textbf{3.5}$$

where κ is the thermal conductivity, ρ is the material density, c_p is the specific heat and f_{mod} is the modulation frequency. For the case of a pulsed laser source being used, f_{mod} is taken as the reciprocal of the pulse width. For an anisotropic material, κ is the thermal conductivity tensor and therefore D_{th} varies with orientation.

If typical values for silicon are used, (κ = 148 $Wm^{-1}K$, ρ = 2331 kgm^{-3} and c_p = 712 $JKg^{-1}K$) and taking f_{mod} to be equal to 100 MHz gives a thermal diffusion length of 0.9 µm. If the longitudinal velocity of sound in single crystal silicon is assumed to be 8556 ms^{-1} [25] (in the (100) direction), the acoustic wavelength is approximately 100 times greater than the thermal diffusion length. If however, the acoustic wave frequency is increased to 1 GHz, the wavelength is now approximately only 10 times greater than the thermal diffusion length as illustrated in Figure 3.3.

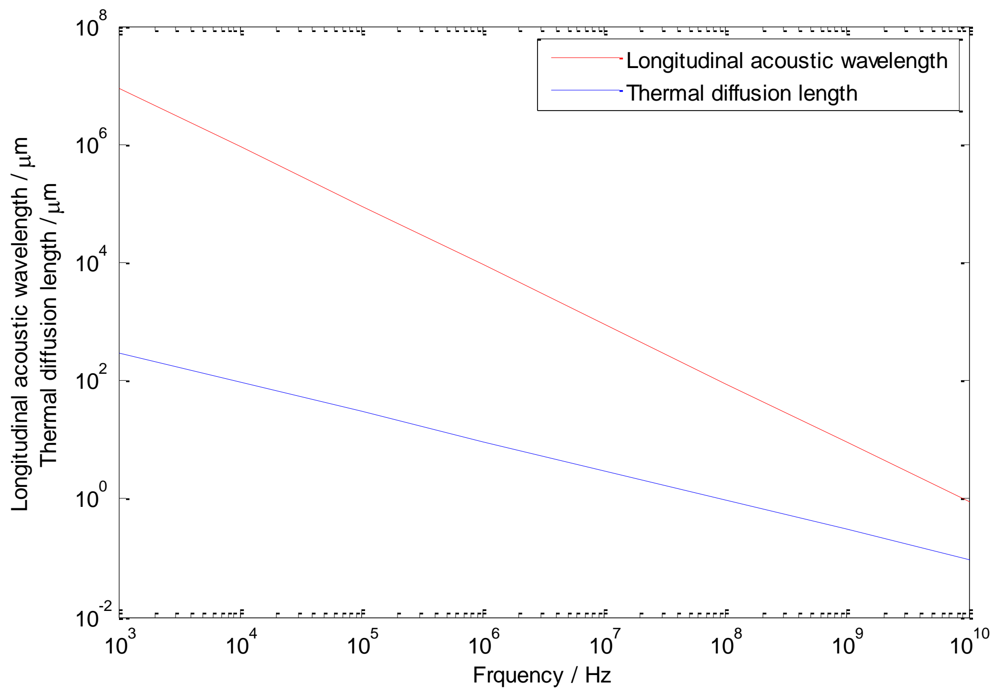

Figure 3.3: Longitudinal acoustic wavelength and thermal diffusion length as a function of frequency in silicon.

The thermal diffusion length is equal to the thermal wavelength [26] and as can be seen, there is a point where the thermal wavelength and acoustic (longitudinal) wavelength will cross. This occurs at frequency limits much beyond those studied in

this thesis however, at this point, the periodic heating from the laser is no longer contained within one acoustic wavelength [27]. This could increase the coupling between the acoustic wave and the thermally induced stress wave [28].

The heat equation governs the distribution of heat in a given space over a given time. The heat equation has traditionally been given as a parabolic equation [29], although it has been shown that the hyperbolic version given below in equation 3.6 is sometimes more suited to thermal generation of acoustic waves [30, 31] for very short pulse lengths.

Hyperbolic Form

$$\frac{\kappa}{c_{th}^2}\frac{\delta^2 T}{\delta t^2} + \rho c_p \frac{\delta T}{\delta t} = \kappa \nabla^2 T + Q(r,t) \qquad \textbf{3.6}$$

where T is the temperature, ρ is the material density, c_p is the specific heat, κ is the thermal conductivity tensor, c_{th} is the thermal wave speed and is usually given as the longitudinal wave velocity, and Q is the heat source proportional to the laser intensity.

Once the laser pulse becomes shorter than $\approx 10^{-9}$ s, it is best to use the hyperbolic form for modelling purposes. For nanosecond pulses, the Fourier heat conduction equation, *i.e.* the parabolic form gives good results, but if picosecond lasers are used, the Fourier equation becomes invalid. For the case of heat conduction, phonons propagate with a limiting speed of heat propagation or the speed of second sound[3], where heat transfer takes place through wave motion rather than diffusion [32, 33].

For nanosecond pulses, the parabolic heat equation is given as

Parabolic Form

$$\rho c_p \frac{\delta T}{\delta t} = \kappa \nabla^2 T + Q(r,t) \qquad \textbf{3.7}$$

[3] Second sound is where heat transfer follows a wave like motion rather than diffusion. Heat takes the place of pressure in normal sound waves and is named so, due to the wave motion of heat being similar to the propagation of sound in air.

The heat source, Q can be given as

$$Q = I_0 f(t) g(x_1, x_2) h(x_3) \qquad \textbf{3.8}$$

where the function $f(t)$ is the temporal profile and is given by

$$f(t) = \frac{t}{t_0^2} exp\left(-\frac{t}{t_0}\right) \qquad \textbf{3.9}$$

and $g(x_1,x_2)$is the spatial profile, given by

$$g(x) = exp\left(-\frac{x_1^2 + x_2^2}{r_0^2}\right) \qquad \textbf{3.10}$$

where t_0 is the rise time of the laser and r_0 is the beam spot radius.

The heat distribution into the material due to the laser pulse decays exponentially within the solid according to

$$h(x_3) = \alpha \exp(-\alpha x_3) \qquad \textbf{3.11}$$

where α is the optical absorption coefficient and $1/\alpha$ is the optical penetration depth as given above. For the time scales of interest in this work, both forms of the heat equation provide indistinguishable results [34]. This was demonstrated by Arias *et al*. [35] who showed that with a 10 ns pulse width, the two equations converged to the same temperature profile after only 150 ps. They were also able to show the infinite speed of propagation associated with the parabolic form compared to the finite propagation speed of the hyperbolic form.

3.6 The thermo-elasto dynamic problem

The induced temperature rise from the absorbed laser energy leads to a volumetric expansion source. This is given in equation 3.12 and shown in Figure 3.4.

$$\phi_T = \frac{3\lambda + 2\mu}{\lambda + 2\mu} \alpha_T T \qquad \mathbf{3.12}$$

where λ and μ are the Lamé elastic constants of the material and α_T is the coefficient of thermal expansion. μ is also known as the shear modulus of the material and both Lamé constants are related to the bulk modulus B of the material by

$$B = \lambda + \frac{2}{3}\mu \qquad \mathbf{3.13}$$

It is this expansion and the resulting temperature gradients that generates stresses and produce a rapidly changing strain field within the material.

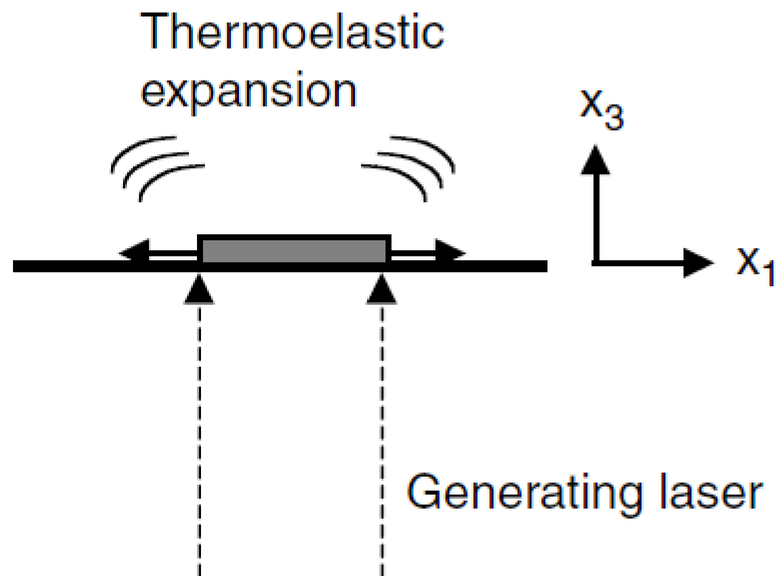

Figure 3.4: Laser generation of ultrasound in the thermoelastic regime [37].

The volumetric expansion leads to local stresses being set up within the material. The irradiated surface is generally unconstrained and is free to expand, however there is a generation mechanism, known as the constrained surface mechanism which restricts this [16]. In the thermoelastic regime, the acoustic waves generated are a function of the angle (known as directivity angle), normal to the plate. These directivity patterns are well documented [1] and show that the longitudinal wave is launched at approximately 60° to the normal while the shear wave is launched at approximately 30° to the normal. In effect, this is launching all types of acoustic waves in all directions, which greatly reduces the efficiency than if one wave was generated in one given direction [36]. There are a large number of elastic waves that can be generated using optical techniques, depending on experimental set up and the structure of the sample, *e.g.* Bulk waves, waves propagating through a material [37], Rayleigh waves, waves propagating along the surface of a half space [38], Lamb waves, waves propagating between two parallel boundaries, *i.e.* a plate or membrane [39], Love waves, waves propagating in the horizontal direction (shear) on a half space [40], Stoneley waves, waves propagating through the interface of two solid half spaces [41]. This thesis will only be concerned with Lamb waves and the formation, propagation and characteristics of these waves will be investigated in more detail in Chapter 5.

3.7 Photostriction as an acoustic wave generation source

An alternative method for generating acoustic waves in semiconductors is using the phenomena known as photostriction. In semiconductor materials, Figielski [42] was the first to show this effect in Germanium while Gauster and Habing [43] were the first to demonstrate it in Silicon.

When a semiconductor is illuminated with light of energy greater than the semiconductor bandgap energy (1.12 eV for silicon), electron-hole pairs are generated in the surface of the material. The depth to which the charge carriers are generated will depend on the optical absorption properties of that material.

If light, of wavelength, λ = 532 nm (E = 2.33 eV), is incident on a silicon surface, a portion of the incident energy (1.12 eV) generates an electron-hole pair. The remaining energy is absorbed by the material as heat. If the correct laser wavelength is chosen, with energy E = 1.12 eV, an electron would be excited to the bottom of the conduction band but there would be no remaining energy available for heating. This case is known as a cold shockwave [44]. Charge carriers are generated in a much faster time than thermal diffusion effects resulting in a photoinduced stress occurring much sooner than a thermal stress. It was never the intention of this work to study the photostrictive effect however, during the literature review, photostriction was discovered and with the experimental setup used in Chapter 6, demonstrating this effect was straightforward. Some basic results will be shown in Chapter 6.

3.8 Conclusions

It has been said that laser ultrasonics will not replace traditional piezoelectric methods unless a specific application is required. It is clear from the above discussion that using optical means to generate elastic waves is a viable alternative to more traditional methods such as piezoelectric transducer. Laser ultrasound does have many advantages and with the exception of expense, these greatly outweigh the disadvantages. When considering generating acoustic waves in MEMS structures, the ability to have an extremely small source is critical, as is ability to have a source that will not damage the sample.

3.9 References

[1] C. B. Scruby and L. E. Drain, “Laser Ultrasonics - Techniques and Applications,” Taylor & Francis, 1990.

[2] V. Vedantham, C. S. Suh and R. Chona, “Laser induced stress wave thermometry for in-situ temperature and thickness charcaterization of single crystalline silicon wafer: Part I - Theory and apparatus,” *Experimental Mechanics,* vol. 51, pp. 1103-1114, 2011.

[3] V. Vedantham, C. S. Suh and R. Chona, “Laser induced stress wave thermometry for in-situ temperature and thickness charcaterization of single crystalline silicon wafer: Part II - Experimental results,” *Experimental Mechanics,* vol. 51, pp. 1115-1122, 2011.

[4] C. Caliendo, A. D'Amico and F. Lo Castro, “Lamb wave propagation along 3C-SiC/AlN membranes for application in temperature-compensated, high-sensitivity gravimetric sensors,” *Sensors,* vol. 13, no. 1, pp. 550-564, 2013.

[5] G. Dobie, A. Spencer, K. Burnham, G. Pierce, K. Worden, W. Galbraith and G. Hayward, “Simulation of ultrasonic lamb wave generation, propagation and detection for an air coupled robotic scanner,” *Ultrasonics,* vol. 51, no. 3, pp. 258-269, 2011.

[6] K. Edalati, A. Kermani, B. Naderi and B. Panahi, “Defects evaluation in lamb wave testing of thin plates,” in *Defects Evaluation in Lamb Wave Testing of Thin Plates*, Bahrain, 2005.

[7] J. Pei, M. I. Yousuf, F. L. Degertekin, B. V. Honein and B. T. Khuri-Yakub, “Lamb wave tomography and its application in pipe erosion/corrosion monitoring,” in *IEEE Ultrasonics Symposium*, 1995.

[8] C. Silva, B. Rocha and A. Suleman, “Guided Lamb waves based structural health monitoring through a PZT network system,” in *NDT in Aerospace*, 2010.

[9] B. Janarthan, M. Mitra and M. Mujumdar, “Damage detection in stiffened composite panels using Lamb wave,” in *6th European Workshop on Structural Health Monitoring*, 2013.

[10] F. H. Chang, T. E. Drake, M. A. Osterkamp, R. S. Prowant, J. P. Monchalin, R. Heon, P. Bouchard, C. Padioleau, D. A. Froom, W. Frazier and J. P. Barton, “Laser ultrasonic inspection of honeycomb aircraft structures,” in *Review of Progress in Quantitative Nondestructive Evaluation*, 1993.

[11] M. Choquet, R. Heon, C. Padioleau, P. Bouchard, C. Neron and J. P. Monchalin, “Laser-ultrasonic inspection of the composite structure of an aircraft in a maintenance hanger,” in *Review of Progress in Quantitative Nondestructive Evaluation*, 1995.

[12] J. P. Monchalin, C. Neron, M. Choquet, D. Drolet and M. Viens, “Laser-ultrasonic instection and characterisation of aeronautic materials,” in *ECNDT*, 1998.

[13] A. G. Bell, “The production of sound by radiant energy,” *Science,* Vols. OS-2, no. 49, pp. 242-253, 1881.

[14] R. M. White, “Elastic wave generation by electron bombardment or electromagnetic wave absorption,” *Journal of Applied Physics,* vol. 34, no. 7, pp. 2123-2124, 1963.

[15] R. M. White, “Generation of elastic waves by transient surface heating,” *Journal of Applied Physics,* vol. 34, no. 12, pp. 3559-3567, 1963.

[16] S. J. Davies, C. Edwards, G. S. Taylor and S. B. Palmer, “Laser-generated ultrasound: its properties, mechanisms and multifarious applications.,” *Journal of Physics D: Applied Physics,* vol. 26, pp. 329-348, 1993.

[17] S. G. Pierce, A. Cleary, I. A. Veres, B. Culshaw, G. Thursby, C. McKee, C. Swift and I. Armstrong, “Low peak-power laser ultrasonics,” *Nondestructive Testing and Evaluation,* vol. 26, no. 3 - 4, 2011.

[18] C. B. Scruby, “Some Applications of Laser Ultrasound,” *Ultrasonics,* vol. 27, pp. 195-209, 1989.

[19] J. F. Ready, Effects of High Power Laser Radiation, New York: Academic Press, 1971.

[20] Y. Matsuda, H. Nakano and S. Nagai, “Precise laser ultrasonic technique with appliocation to silicon velocity measurements,” *Jpn. J. Appl. Phys.,* vol. 39, pp. L59-L61, 2000.

[21] S. B. Palmer and S. Dixon, “Industrially viable non-contact ultrasound,” *Insight,* vol. 45, no. 3, 2003.

[22] S. Dixon, C. Edwards and S. B. Palmer, “Generation of ultrasound by an expanding plasma,” *Journal of Physics D: Applied Physics,* vol. 29, pp. 3039-3044, 1996.

[23] D. R. Lide, Ed., CRC Handbook of Chemistry and Physics, CRC Press, 2005.

[24] R. A. Paquin, “Properties of Metals,” in *Handbook of Optics*, 3rd ed., Vols. IV Optical Properties of Materials, Nonlinear Optics, Quantum Optics, McGraw Hill, 2010.

[25] S.-F. Wang, Y.-F. Hsu, J.-C. Pu, J. C. Sung and L. G. Hwa, “Determination of acoustic wave velocities and elastic properties for diamond and other hard materials,” *Materials Chemistry and Physics,* vol. 85, pp. 432-437, 2004.

[26] G. Busse and A. Rosencwaig, “Subsurface imaging with photoacoustics,” *Applied Physics Letters,* vol. 36, no. 10, pp. 815-816, 1980.

[27] G. S. Kino and R. G. Stearns, “Acoustic wave generation by thermal excitation of small regions,” *Applied Physics Letters,* vol. 47, no. 9, pp. 926-928, 1985.

[28] K. Atherton, B. Culshaw, F. Dong, P. Jun, G. Pierce and C. Swift, “Generation and detection of broadband laser generated ultrasound from low power laser sources,” in *Photonics 2000: International Conference on Fiber Optics and Photonics*, Calcutta, India, 2001.

[29] E. Kreyszig, Advanced Engineering Mathematics, 8th ed., Wiley, 1999.

[30] F. A. McDonald, “Practical quantitative theory of photoacoustic pulse generation,” *Appl. phys. Lett.,* vol. 54, no. 16, pp. 1504-1506, 1989.

[31] J. B. Spicer, A. D. McKie and J. W. Wagner, “Quantitative theory for laser ultrasonic waves in a thin plate,” *Appl. Phys. Lett,* vol. 57, no. 18, pp. 1882-1884, 1990.

[32] Y. M. Ali and L. C. Zhang, “Relativistic heat equation,” *International Journal of Heat and Mass Transfer,* vol. 48, pp. 2397-2406, 2005.

[33] R. Domanski, M. Jaworski and M. Rebow, “Laser radiation interaction with solids,” *Journal of Power Technologies,* vol. 79, 1995.

[34] S. Krishnaswamy, “Theory and Applications of Laser-Ultrasonic Techniques,” in *Ultrasonic Nondestructive Evaluation: Engineering and Biological Material Characterization*, T. Kunda, Ed., CRC Press, 2004, pp. 435-494.

[35] I. Arias, T. W. Murray and J. D. Achenbach, "Near field analysis of laser-generated ultrasound: The effects of thermal diffusion and optical penetration," in *Quantitive Nondestructive Evaluation*, Brunswick, Maine, 2001.

[36] F. Enguehard and L. Bertrand, "Effects of optical penetration and laser pulse duration on laser generated longitudinal acoustic waves," *J. Appl. Phys.,* vol. 82, no. 4, pp. 1532-1538, 1997.

[37] S. Krishnaswamy, "Photoacoustic Characterization of Materials," in *Handbook of Experimental Solid Mechanics*, W. N. Sharpe, Ed., Springer, 2008, pp. 769-800.

[38] J. W. Strutt (Lord Rayleigh), "On the free vibrations of an infinite plate of homogeneous isotropic elastic matter," *Proc. Lond. Math. Soc,* vol. 20, no. 357, p. 225, 1889.

[39] H. Lamb, "On waves in an elastic plate," *Proc. Lond. Math. Soc.,* vol. 93, no. 648, p. 114, 1916.

[40] A. E. Love, Some problems of geodynamics, University of Cambridge, 1911.

[41] R. Stoneley, "Elastic waves at the surface of separation of two solids," *Proc. R. Soc. Lond. A.,* vol. 106, no. 738, pp. 416-428, 1924.

[42] T. Figielski, "Photostriction effect in germanium," *Physica Status Solidi,* vol. 1, no. 4, pp. 306-316, 1961.

[43] W. B. Gauster and D. H. Habing, "electronic volume effect in silicon," *Phys. Rev. Lett.,* vol. 18, no. 24, pp. 1058-1061, 1967.

[44] A. N. Dharamsi and A. B. Hassam, "Cold shock waves in semiconductors and insulators," *J. Appl. Phys.,* vol. 65, no. 8, pp. 2998-3005, 1989.

4 Optical Detection of Elastic Waves

4.1 Introduction

Since a laser can be used to generate acoustic waves in a medium in a non-contact way, it is reasonable to suggest that a laser will be able to detect acoustic waves via laser interferometry. Although other methods are available, such as piezoelectric detection, electromagnetic acoustic transducers (EMATS) and various non interferometric techniques, interferometric techniques have become common place when laser generated ultrasound is used. Piezoelectric transducers are by far the most common method, with the most common material being lead zirconate titanate (PZT). One of the initial draw backs of piezoelectric materials was that they cannot be used above around 350°C [1]. At this temperature, the Curie point, the material loses its ferroelectric properties. Other piezoelectric materials can be used above this temperature such as lead metaniobate or lithium niobate [2]. Piezoelectric polymers are being used more frequently now with a common type being polyvinylidene fluoride (PVDF) [3]. Piezoelectric materials, when subjected to a stress or pressure, become electrostatically charged, resulting in a potential difference. For this to happen, the sensing material must be coupled to the sample, using some form of couplant. Apart from the obvious problems associated with this such as being a contact method and contaminating the sample, and indeed the signal detected. Piezoelectric transducers that use air as the coupling medium have also been demonstrated [4]. EMATS detect acoustic waves by detecting an electromotive force which alters a magnetic field in a solenoid within the EMAT [5]. EMATS have the disadvantage that only metallic or ferroelectric materials can be investigated.

Over the other methods available for ultrasonic detection, optical techniques offer the following advantages.

a. They are non-contact; therefore do not disturb the ultrasonic field.
b. The measurement point can be moved as required.
c. There is no restriction on surface temperature.
d. High spatial resolution is obtainable without a reduction in sensitivity
e. A flat broadband frequency response is achievable
f. The measurement is directly related to the wavelength of the light used in the interferometer so no other calibration is required.

4.2 Review of optical methods for ultrasonic wave detection

As stated in the introduction, there are a number of methods used to detect acoustic waves in a material. Optical techniques offer the opportunity to detect acoustic waves not only through a non-contact method, but also to give the possibility of studying elastic wave behavior in structures where the geometries are in the millimeter region typically found in MEMS devices, which would normally be awkward to access. This chapter focuses on non-contact methods, but it is also worth remembering that optical contact methods exist as well. Using optical fibres bonded to or embedded in structures is also a viable method of ultrasonic detection. The fibres could have a fibre Bragg grating written onto them, creating a periodic variation in the optical fibre’s core, where the strain in the material causes a reflection of a particular wavelength of light from the grating corresponding to that strain. Alternatively, changes in the polarisation of the light in the fibre can be used as a measure of strain. This configuration is known as a polarimeter. Further information on these two methods can be obtained from [6]. Optical techniques can fall into two categories [7].

a. Non interferometric techniques
b. Interferometric techniques.

4.2.1 Non interferometric detection of ultrasound

Three optical methods of detecting elastic waves in solids that are not based on interferometry have been previously demonstrated.

a. Knife edge technique – When an elastic wave travels through a medium, the surface is displaced as the wave passes. If a laser beam is incident on the surface, the elastic wave deflects the laser beam. The beam deviation is measured with either a detector with a knife edge in front of it or a position sensitive detector. The spot size of the laser beam has to be focused so that it is smaller than the elastic wave wavelength. Sontag and Tam [8] applied this method for the detection of photoacoustic pulses in thin silicon wafers.

b. Reflectivity technique – By applying a stress to a material, a change in the refractive index is caused and this, in turn changes the specular and diffuse reflectivity of the material. Thomsen *et al.* [9] used this method to detect the effect of ultrasonic strain echoes caused by a picosecond pulse on the optical properties of the thin film surface.

c. Surface Grating Technique – when light is incident, normal to a sample surface, it can be diffracted by a periodic displacement on the sample surface. The diffraction can be into several orders that do not follow the reflected path of the incident light. The angle of the diffracted light is therefore a function of the acoustic wave's wavelength [10].

4.2.2 Interferometric detection of ultrasound

The subject of optical detection of ultrasound has been reviewed by several authors including Scruby and Drain [2], Monchalin [7], Dewhurst and Shan [11] and Wagner [10]. Dewhurst describes three steps that a typical interferometric system should follow:

1 Ultrasonic to optical phase conversion.
2 Optical phase to intensity conversion.
3 Intensity to electronic signal conversion.

To understand these steps, the basic principles of interferometry must be considered (the theory of interferometry will be described in more detail in the next section). When a beam is split using a beamsplitter, the beams travel in different directions, with each component incident on a sample and reference mirror and returning to the beamsplitter where they recombine. If the sample is being excited by a harmonic wave or otherwise, then the phase of the return beam will be altered with respect to the beam from the reference mirror. This means any displacement (*i.e.* change of phase) detected on the sample can be referenced to the wavelength of the light used in the interferometer. It should be noted that interferometers need a coherent light source. Once the beams have recombined in the beamsplitter, the interference between the reference beam and the phase altered sample beam causes fluctuations in the beams intensity. Some form of photodetector finally converts this intensity to a voltage.

There are a large number of interferometers, designed and developed for many applications. For the purpose of elastic wave detection, derivations of four main types of interferometer are common place. These are the Michelson interferometer, the Mach-Zehnder interferometer, the Fabry-Pérot interferometer and the photorefractive interferometer.

The Michelson interferometer and the Mach-Zehnder interferometer are examples of two beam interferometers where the laser beam is divided into two beams with one beam propagating to the sample while another propagates to a reference mirror. Two beam interferometers can further be divided into two categories. The homodyne interferometer where no frequency shift is introduced into either beam path, or the heterodyne interferometer, where the reference path is frequency shifted by some sort of acousto-optical (or electro-optic) modulator such as a Bragg cell. The

heterodyne Mach-Zehnder interferometer is the basis for the single point and scanning vibrometers produced by Polytec [12]. The Michelson interferometer has been used by a number of research groups. Kokkonen *et al.* [13] used a heterodyne Michelson interferometer for both phase and amplitude measurements of surface waves. They later show the same instrument could be used to measure amplitudes down to ≈1 pm [14]. Hernandez *et al.* [15] used a Michelson interferometer for the characterisation of thin films and Murray and Balogun [16] constructed an acoustic microscopy based on the Michelson principle. Hurley *et al.* [17] used a Michelson interferometer for the characterisation of thin films.

The Fabry-Pérot interferometer, or more commonly, the confocal Fabry-Pérot interferometer is made up of two concave mirrors facing each other and separated by a distance roughly equal to their common radius of curvature [18]. Unlike the Michelson interferometer, which is sensitive to surface displacements, the Fabry-Pérot is sensitive to the surface velocity making it insensitive to background vibrations. Monchalin modified this interferometer in the 1980s [19], coupling it with a heterodyne Michelson interferometer to measure ultrasound from a diffuse surface, typically encountered in industrial applications.

Ultrasonic waves have also been detected using the photorefractive effect. This type of interferometer use photorefractive crystals to compensate for distorted wavefronts usually associated with rough surfaces, a rusted surface for example [11]. This principle is the basis for the interferometers developed by Intelligent Optical Systems (IOS) [20].

4.3 The path stabilised Michelson interferometer

Interferometers, when used for elastic wave detection, are designed to measure small displacements (picometres to nanometres). If the interferometer is in a mechanically noisy environment, *i.e.* one where there are a lot of background vibrations and turbulence, this could cause the sample to vibrate with displacements on the order of micrometres [2] as shown in Figure 4.1

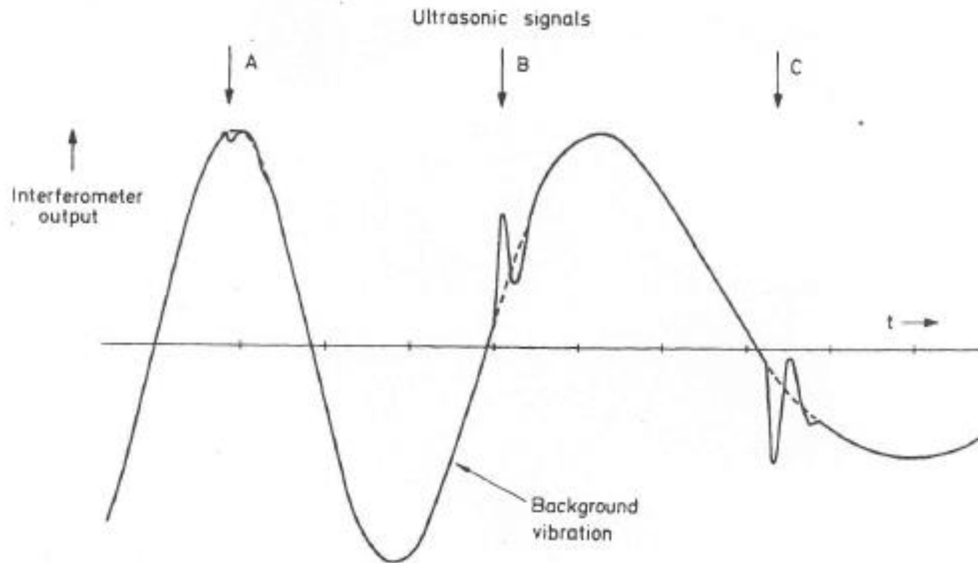

Figure 4.1:Ultrasonic signals superimposed on a low frequency background from an unstabilised interferometer [2].

To eliminate this problem, active stabilization is required. In the case of the Michelson interferometer, this is achieved by altering the optical path length of the reference arm compensating for the low frequency components of the motion of the surface. Ultimately, this should be the final stage of a vibration reduction scheme, where all unnecessary sources of vibration are previously removed. It was found in the course of this work that two major sources of mechanical noise were air turbulence caused by conditioning ducts and the low level train network. Conducting the experiments in the evenings and at weekends reduced the background vibration temporarily ignoring any stabilisation scheme. Altering the optical path length is achieved by using a feedback scheme that drives a piezoelectric (in this case,) or electro –mechanical or electro-optic phase shifting device in the reference arm. With the optical path lengths held in a balanced state, any deviation from this, results in an output from a circuit of the correct sign to change the phase of the reference beam restoring the balanced state.

The basic layout of a Michelson interferometer is shown in Figure 4.2 When light is reflected from a moving or vibrating object, the displacement of the surface will

produce a change in the optical path length between the mirror arm (known as reference arm) and the sample arm (known as signal arm). If the surface of a sample is displaced by an amount d, the optical path is reduced (or increased) by $2d$. This change to path length corresponds to a change in optical phase, φ of

$$\varphi = 2(2\pi)\left(\frac{2d}{\lambda}\right) \tag{4. 1}$$

where λ is the wavelength of the interferometer laser. This change in phase cannot be measured directly however an interferometer can convert the phase change to an intensity variation which can be measured. In the Michelson interferometer, a beamsplitter splits the beams in a 50/50 ratio, (other ratios are available) sending one beam to each arm. Depending on the application, a different ratio in a beamsplitter may be preferred or more commonly to use a half wave plate to adjust the polarization of the light entering the beamsplitter. In not doing so, a reduction in fringe visibility is observed. The reference mirror will return ~ 99% of the incident light while the signal arm may only return 35%. A half wave plate becomes the obvious choice. This example is based on using a source wavelength of 633 nm on single crystal silicon. The beams reflect off the sample and reference mirror and return to the beamsplitter where they recombine. The beam then travels to the photodetector which detects the change in intensity. The intensity I_D on the detector varies according to the relationship

$$I_D = I_R + I_S + 2\sqrt{I_R I_S}\,cos(\varphi_R - \varphi_S) \tag{4. 2}$$

where I_R and I_S are the intensities in the reference and signal arms respectively and φ_R and φ_S are the phases in each arm. This means that an interferometer converts a surface displacement to a change in optical power.

The optical intensity varies as an offset cosine function affecting the depth of modulation on the amplitudes of the reference and signal beams. Consider the case

where the change in intensity is plotted as a function of optical path length (or change in phase), as in Figure 4.3. When the optical path length is zero, $\lambda/_2$ or λ, *i.e.* when I_R and I_S are equal, the slope in the intensity variation is zero, so any small change in d will result in little or no change in intensity and the interferometer would be insensitive to displacements on the surface sample. If however the optical path length is held at the $\lambda/_4$ or $3\lambda/_4$ point, *i.e.* where the slope of the intensity variation is at a maximum, the sensitivity is at its greatest.

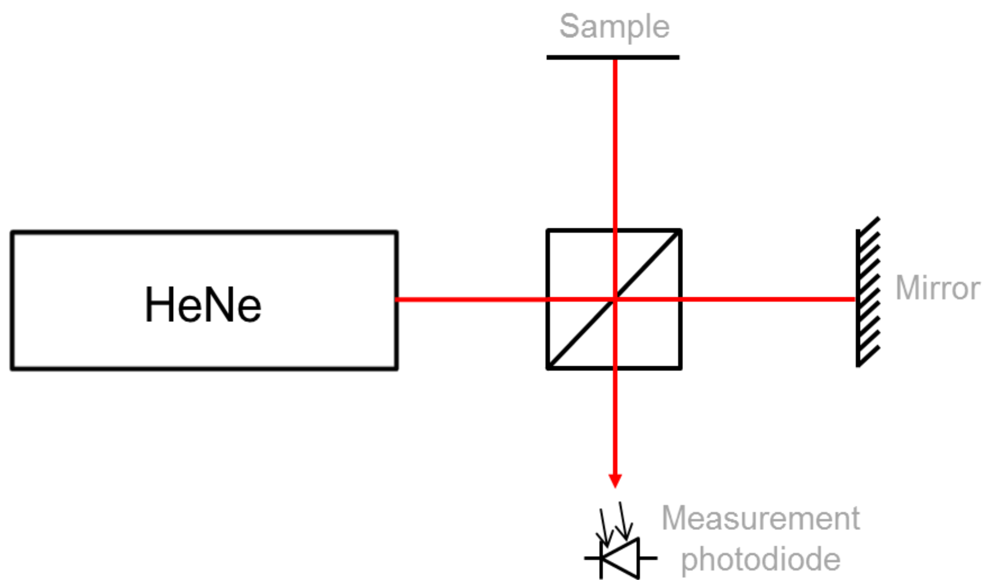

Figure 4.2: Schematic layout of Michelson interferometer.

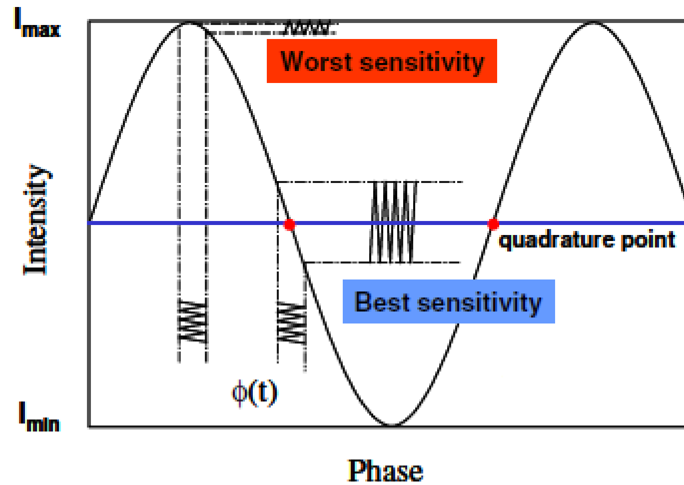

Figure 4.3: Two beam interferometer output intensity as a function of phase change. The largest variation in output intensity for a small phase change occurs at the quadrature point [21].

The path stabilized Michelson interferometer constructed for this project was a joint effort by myself, Dr Ian Armstrong and Dr Alison Cleary. The interferometer is shown schematically in Figure 4.4 and pictorially in Figure 4.5. The interferometer was constructed using the Linos Microbench components and optics such as beamsplitters, waveplates, mirrors, positioners, etc. The laser beam was produced by a 633 nm Thorlabs HRP120-1 linearly polarized laser [22] and after refection from the beam steering mirror, passes through the first half waveplate ($\lambda/_2$). When aligning the interferometer, this waveplate is used to ensure a 50/50 split after the beam has passed through the first polarising beam splitter (PBS 1). Once the interferometer is aligned and measurements are being conducted, this waveplate is used to balance the intensities of the return beam from the reference mirror and sample. While the reflectivity of the reference mirror will not change, the reflectivity of the sample will change. This reflectivity is a function of combinations of various functions, such as wavelength (633 nm for HeNe laser), temperature, residual stress etc. Reflectivity as a function of wavelength is described in Chapter 3 when discussing absorption of electromagnetic energy. The two quarter waveplate ($\lambda/_4$) are used to ensure the polarisations of the two beams returning to the polarising beam splitter are orthogonal. The second half waveplate just after the beam splitter, is used

to rotate the polarization angel by 45° to make sure an even split in the two arms exiting the second polarising beam splitter. The third half waveplate rotates the polarization so that when the beam is incident on the two BK7 windows, the polarization states are the same and remain that way up to the feedback photodetectors. These windows reflect approximately 4% of the incident light so as not to saturate the photodetectors. Reflections from within the window are masked by placing pinholes in front of the two photodetectors. The ×5 microscope objective (Nikon LU Plan Fluor) is used to focus the beam onto the measurement photodiode while the other microscope objective is used to visualize the interference fringes on a screen. The two microscope objectives used to focus the beams onto the sample and reference mirror were ×20 microscope objectives (Olympus Plan N FN22).

It was discovered that these objectives gave a focused spot size of approximately 50 μm. A spot size of 50 μm, can be used to measure a minimum wavelength of 100 μm. Assuming a longitudinal acoustic wave velocity of 9000 ms^{-1} (approximate value in silicon), only acoustic waves up to a frequency of approximately 90 MHz can be detected. The focusing objective in the sample arm was changed to a ×100 microscope objective (Nikon LU Plan EPI).

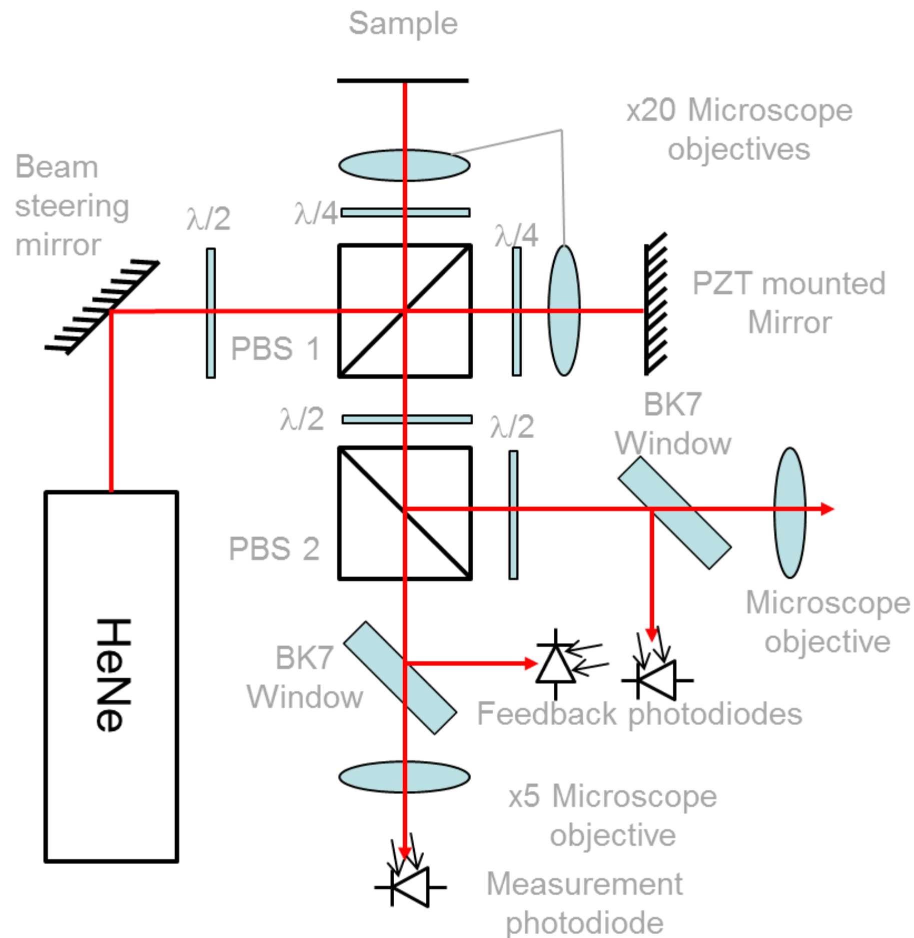

Figure 4.4: Schematic layout of the path stabilised Michelson interferometer constructed for the detection of acoustic waves.

The spot size was measured to have a FWHM value of 8.6 μm increasing the detectable frequency to well in excess of 200 MHz. This value of 8.6 μm is visible in Figure 4.6. It was in fact the signal amplifier (Fempto DHPCA-100 Amplifier) that limited the upper frequency limit. The beam profile was measured using a Thorlabs beam profiler (BP104-IR) and is shown in Figure 4.6. The wavelength range of the beam profiler is 700 nm to 1800 nm with a peak response (A/W) value at 1550 nm of approximately 0.85. Extrapolating below 700 nm to the 633 nm region gives a response value of 0.15. This means that although the system is not optimized for this wavelength, it is still able to give an accurate reading for the spot size.

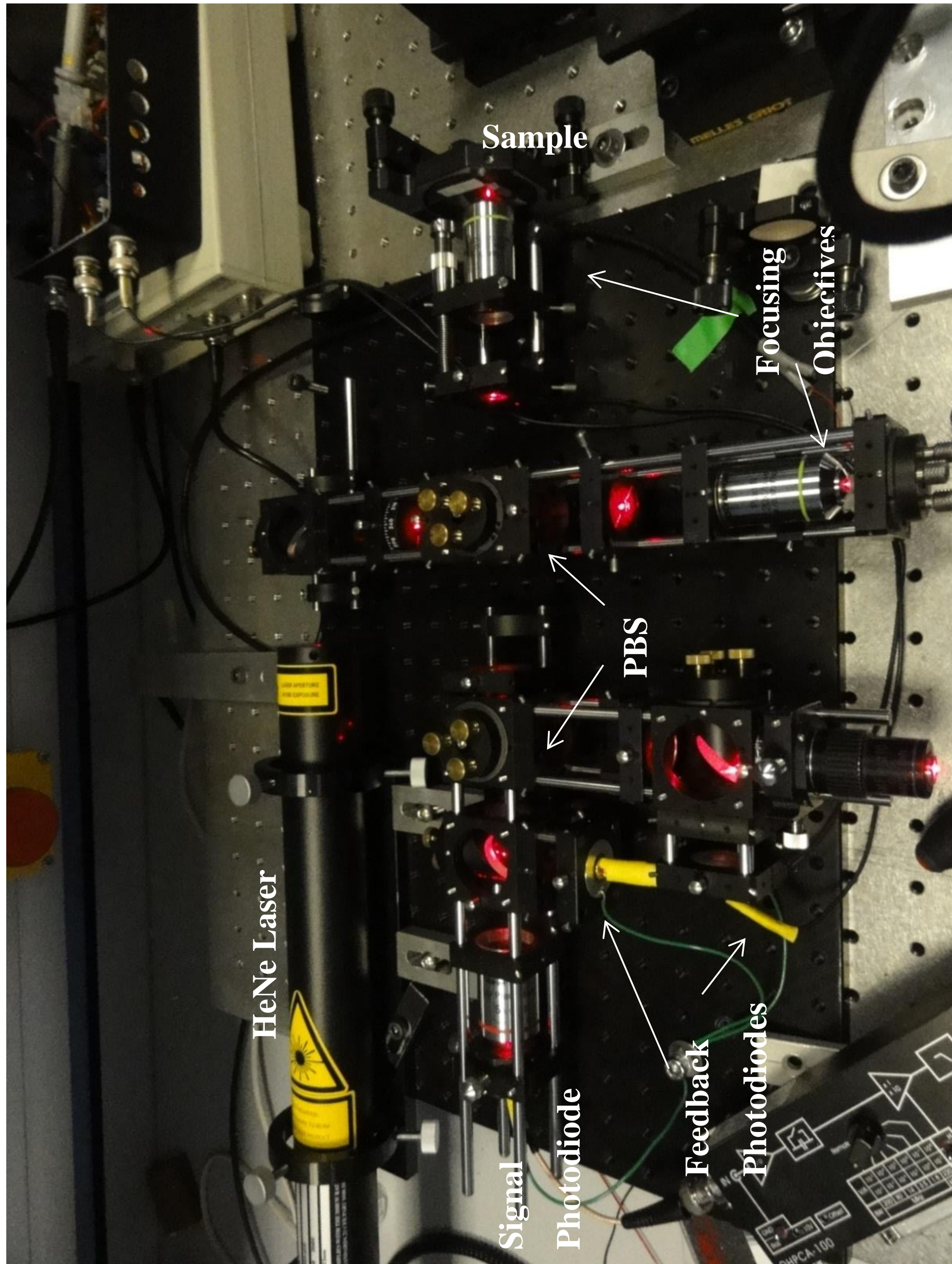

Figure 4.5: The Michelson interferometer.

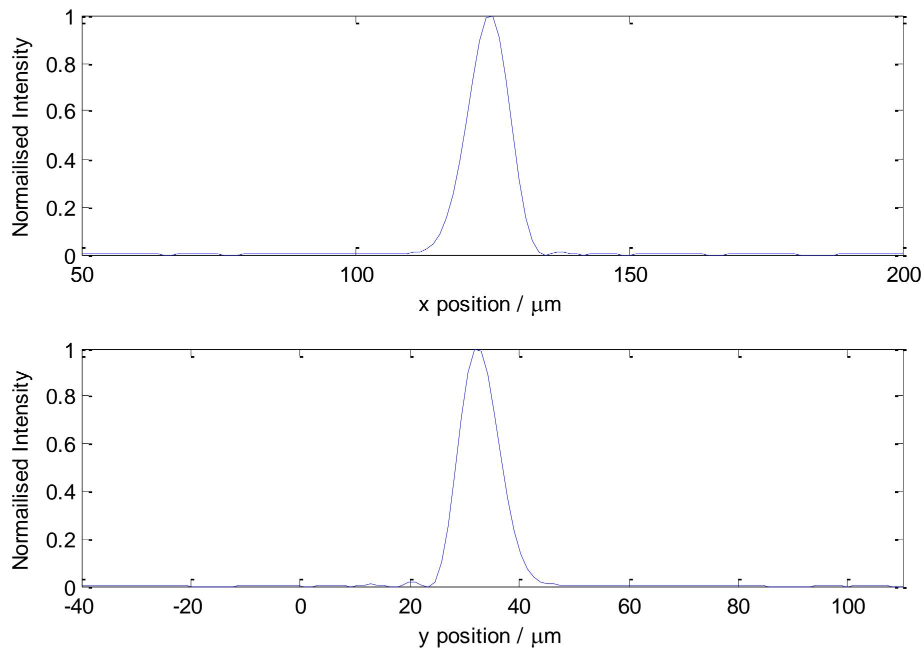

Figure 4.6: Beam profile of HeNe laser and ×100 microscope objective.

4.3.1 Calibration of the Michelson interferometer.

The output of the Michelson interferometer, through the amplifier electronics is given in Volts. This needs some proportionality constant to convert it to a displacement. Ultimately, the work in this thesis does not depend on displacement outputs, only frequency content of the measured signals. However, time domain results are shown, so the calibration method will be described here.

The proportionality constant does depend on the light return to the detection electronics. The equation to convert output voltage to displacement is given in equation 4.3 [2].

$$d = \frac{\lambda}{4\pi} sin^{-1}\left(\frac{V}{V_0}\right) \qquad \textbf{4.3}$$

where d is the surface displacement, λ is the optical wavelength, V is the detector output and V_0 is the amplitude of the interference.

To obtain a value for V_0, the feedback electronics are switched off and the reference mirror is driven through a number of cycles. The peak to peak signal voltage is parameter V_0.

4.3.2 Electronic stabilisation of the Michelson interferometer to compensate for background vibrations

Piezoelectric stabilisation schemes have been utilized by a large number of researchers and the principle can be applied to both free space and optical fibre interferometers. In an optical fibre interferometer, the reference arm fibre is wrapped around a piezoelectric ring which expands, changing the length of the fibre. A major advantage of using this method in a free space configuration is that the piezoelectric material can accept applied negative voltages so the mirror can be moved in both directions. Jackson *et al.* [23], Fritsch and Adamovsky [24] and Xie *et al.* [25-29] used this type of stabilisation principle and the circuit shown in Figure 4.7 is based on the work presented by the above authors.

It was discussed in section 4.3 that a change in phase cannot be directly measured, but the phase change resulting from a sample displacement can be measured as a change in intensity. This prevents effects such as background mechanical vibrations and drift from affecting the detected signal via changes in phase. The best sensitivity comes from ensuring that the static phase change is maintained at quadrature as shown in Figure 4.3

The sensitivity of the instrument to the acoustic waves will vary and the best sensitivity is achieved at the quadrature points. Likewise, signals occurring near the least sensitive range are hardly detected and this is known as the fade out problem where the signal will vanish. This can be avoided by holding the instrument at the quadrature point. To achieve this, one of the arms of the interferometer is adjusted in length to maintain the phase difference at the quadrature point.

Due to the setup of the interferometer, the relative phase of the interference is 180° out of phase on each photodiode. The currents from the two photodiodes are linearly proportional to the optical signals. Referring to Figure 4.7, PD1 and PD2 are connected to two current to voltage convertors U1 and U2. Potentiometers R3 and R4 balance the offset of the convertors and potentiometer R1 is used to match the outputs of the two convertors. The bandwidth of the circuit is determined by the RC value set in the current to voltage convertors and is approximately 800 Hz. The outputs from these two convertors are combined through difference amplifier U3. This locates the quadrature point and is dependent on the phase difference of the light incident on the two photodiodes and the contrast of the interference pattern. Any deviation from the quadrature point is integrated using integrator U4 and after passing through a gain stage (U5 and U6) this is fed back to the piezoelectric element. It is the nature of an electronic integrator to drift [30] and for this reason a reset switch is added. All op-amps are connected to a ±12 V power supply and decoupled using 100 nF and 10 µF capacitors.

Figure 4.7: Schematic diagram of the electronic feedback stabilisation circuit.

4.4 Noise considerations, sensitivity and sources of error

When measuring displacements (out of plane displacements in this case) of the order of picometres, such as those produced by elastic waves, one must be very wary of sources of noise and errors in an interferometric system. When an optical system is

stabilised electronically, the reference arm varies the optical path length and so varies the intensity of the interference fringes detected on the photodiode. This variation is much less than the wavelength of the laser light used and the sensitivity to this variation depends on the position in the intensity-optical path length curve shown in Figure 4.3 [31].

The wavelength of light used is generally given as 633 nm. However this value is quoted for vacuum. The wavelength for a red HeNe laser in air is given as 632.816 nm [32]. The actual wavelength propagating through the system will depend on the refractive index of air and this itself will depend on air density, pressure, humidity and temperature.

The sensitivity of the interferometer, when measuring picometre displacements is typically much less than that of a piezoelectric transducer. However, one should bear in mind that the laser probe size is much smaller than the area of a piezoelectric transducer and one of comparable size to a laser spot would be no more sensitive [33]. Another reason for low sensitivity in an interferometer is the higher bandwidth compared to piezoelectric sensors. When using laser generated ultrasound, an interferometer is more sensitive to broadband pulses as sensitivity depends on the signal to noise ratio and therefore on the bandwidths of the signal and background noise.

The signal to noise ratio is the desired output signal divided by the total noise in the system [34]. The quantum noise of the detector, or shot noise, is what sets the limit to the ultimate performance of the interferometer. Other sources of noise, *e.g.* thermal (changes in temperature) and low frequency mechanical vibration, can be compensated for.

For a homodyne interferometer, the RMS signal to noise ratio is given by [2]

$$\frac{i_s}{i_n} = \sqrt{\frac{P\eta}{4Bh\upsilon}} \tag{4. 4}$$

where i_s is the photocurrent signal, i_n is the photocurrent noise, P is the power of the light from the sample impinging on the photodiode, η is the quantum efficiency of the detector, B is the detection frequency bandwidth and $h\nu$ is the energy of a quantum of light of frequency ν. From this, it can be seen that the signal to noise ratio is proportional to the square root of the laser power and inversely proportional to the square roots of the detection bandwidth. Improving the signal to noise ratio is possible by increasing laser power and decreasing detection bandwidth.

The minimum detectable displacement, U_{min} can be calculated by setting the signal to noise ratio equal to 1. This is given by

$$U_{min} = \frac{\lambda}{4\pi}\sqrt{\frac{2Bh\nu}{P\eta}} \tag{4. 5}$$

To estimate the signal to noise ratio and minimum detectable displacement for the Michelson interferometer describe above, the values in Table 4.1 are used.

Table 4.1: Signal to noise ratio and minimum detectable displacement parameters.

Parameter	Value
P	10.1 mW
η	0.25
B	199.999 MHz
h	6.626.693 × 10^{-34} Js
ν	4.7233 × 10^{14} Hz
λ	632.816 nm

Laser power was measured using a Gentec Solo PE Power Meter with XLP12-3S-H2-D0 head and taking the $1/_{e^2}$ beam diameter of the laser to be 0.88 mm [22]. The value for quantum efficiency is taken from the detection photodiode datasheet and Planck's constant and speed of light are taken from [35], assuming a refractive index of 1.003 for air. From equations 4. 4 and 4. 5, a signal to noise ratio of ≈3200 and a minimum detectable displacement of 11.2 pm at 1 Hz is calculated.

The signal to noise ratio can be improved further by averaging the signal during data collection. The increase in signal to noise ratio using averaging is given by $\sqrt{n}\frac{S}{\sigma}$ where S is the signal strength, n is the number of measurements taken and σ is the standard deviation of a single measurement.

4.5 Conclusions

There are various methods of detecting ultrasonic waves, both contact and non-contact. This chapter has focused on non-contact optical methods, with interferometry being the most common and useful for MEMS structures. While the knife edge technique can have excellent sensitivity, it isn't suited to small complex structures. Other interferometry techniques are available, for long range applications or rough surfaces but the Michelson interferometer is the simplest and most suitable for a laboratory setting. The construction of the Michelson interferometer used in this work has been described as has the method of stabilisation against background vibrations. Finally, the system performance has been characterised.

4.6 References

[1] A. S. Murfin, R. A. Soden, D. Hatrick and R. J. Dewhurst, "Laser ultrasound detection systems: A comparative study with Rayleigh waves," *Meas. Sci. Technol.,* vol. 11, pp. 1208-1219, 2000.

[2] C. B. Scruby and L. E. Drain, Laser Ultrasonics, Techniques and Applications, Bristol: Taylor & Francis Group, 1990.

[3] H. Kawai, “The Piezoelectricity of Poly (vinylidene Fluoride),” *Japan. J. Appl. Phys.,* vol. 8, pp. 975-976, 1969.

[4] D. A. Hutchins, W. M. Wright, G. Hayward and A. Gachagan, “Air-coupled piezoelectric detection of laser-generated ultrasound,” *IEEE Trans. Ultrason. Ferroelectr. Frequency Control,* vol. 41, pp. 796-805, 1994.

[5] K. Kawashima, “Theory and numerical calculations of the acoustic field produced in metal by an electromagnetic ultrasonic transducer,” *J.Acoust.Soc.Am,* vol. 11, pp. 195-213, 1994.

[6] B. Culshaw, G. Thursby, D. Betz and B. Sorazu, “The detection of ultrasound using fiber-optic sensors,” *IEEE Sensors J.,* vol. 8, no. 7, pp. 1360-1367, 2008.

[7] J.-P. Monchalin, “Optical detection of ultrasound,” *IEEE Trans. Ultrason. Ferroelectr. Frequency Control,* vol. 33, no. 5, pp. 485-499, 1986.

[8] H. Sontag and A. C. Tam, “Optical monitoring of photoacoustic pulse propagation in silicon wafers.,” *Appl. Phys. Letters.,* vol. 46, pp. 725-727, 1985.

[9] C. Thomsen, H. T. Grahn, H. J. Marris and J. Tauc, “Ultrasonic experiments with picosecond time resolution.,” *J. Physique,* vol. 46, no. C10, pp. 765-772, 1985.

[10] J. W. Wagner, “Optical detection of ultrasound,” in *Physical Acoustics*, vol. 19, R. N. Thurston and A. D. Pierce, Eds., New York, Academic, 1990, pp. 201-266.

[11] R. J. Dewhurst and Q. Shan, “Optical remote measurement of ultrasound,” *Meas. Sci. Technol.,* vol. 10, pp. R139-R168, 1999.

[12] “Polytec,” Polytec, [Online]. Available: http://www.polytec.com/uk/.

[13] K. Kokkonen, J. V. Knuuttila, V. P. Plessky and M. M. Salomaa, “Phase-sensitive absolute-amplitude measurements of surface waves using heterodyne interferometry,” in *IEEE Ultrasonics Symposium*, 2003.

[14] K. Kokkonen and M. Kiavola, “Scanning heterodyne laser interferometer for phase-sensitive absolute-amplitude measurements of surface vibrations,” *Appl. Phys. Lett.,* vol. 92, p. 063502, 2008.

[15] C. M. Hernandez, T. W. Murray and S. Krishnaswamy, “Photoacoustic characterisation of the mechanical properties of thin films,” *Appl. Phy. Lett.,* vol. 80, no. 4, pp. 691-693, 2002.

[16] T. W. Murray and O. Balogun, “High-sensitivity laser-based acoustic microscopy using a modulated excitation source,” *Appl. Phys. Lett.,* vol. 85, no. 14, pp. 2974-2976, 2004.

[17] D. C. Hurley, V. K. Tewary and A. J. Richards, “Thin-film elastic-property measurements with laser ultrasonic SAW spectrometery,” *Thin Film Solids,* Vols. 398-399, pp. 326-330, 2001.

[18] R. J. Dewhurst and Q. Shan, “Modelling of confocal Fabry-Pérot interferometers for the measurement of ultrasound,” *Meas. Sci. Technol.,* vol. 5, pp. 655-662, 1994.

[19] J.-P. Monchalin, “Optical detection of ultrasound at a distance using a confocal Fabry-Perot interferometer,” *Appl. Phys. Lett.,* vol. 47, pp. 14-16, 1985.

[20] Intelligent Optical Systems, [Online]. Available: http://www.intopsys.com/laserultrasound.html.

[21] D. H. Kim, B. Y. Koo, C. G. Kim and C. S. Hong, “Damage detection of composite structures using a stabilized extrinsic Fabry–Perot interferometric sensor system,” *Smart Materials and Structures,* vol. 13, pp. 593-598.

[22] “ThorLabs,” [Online]. Available: http://www.thorlabs.com/Thorcat/12100/HRP120-SpecSheet.pdf.

[23] D. A. Jackson, R. Priest, A. Dandridge and A. B. Tveten, “Elimination of drift in a single mode optical fiber interferometer using a piezoelectrically stretched coiled fiber,” *Applied Optics,* vol. 19, no. 17, pp. 2926-2929, 1980.

[24] K. Fritsch and G. Adamovsky, “Simple circuit for feedback stabilisation of a single mode optical fiber interferometer,” *Rev. Sci. Instrum.,* vol. 52, no. 7, pp. 996-1000, 1981.

[25] F. Xie, X. Chen and L. Zhang, "High stability interleaved fiber Michelson interferometer for on-line precision displacement measurements," *Optics and Lasers in Engineering,* vol. 47, pp. 1301-1306, 2009.

[26] F. Xie, Z. Chen and J. Ren, "Stabilisation of an optical fiber Michelson interferometer measurement system using a simple feedback circuit," *Measurement,* vol. 42, pp. 1335-1340, 2009.

[27] F. Xie, J. Ren and Z. Chen, "Design and analysis of a highly stabilised optical fiber Michelson interferometer measurement system," *Sensors and Actuators A: Physical,* vol. 152, pp. 176-181, 2009.

[28] F. Xie, J. Ren, Z. Chen and Q. Feng, "Vibration-displacement measurements with a highly stabilised optical fiber Michelson Interferometer system," *Opt. Laser Technol.,* vol. 42, no. 1, 2009.

[29] F. Xie, Z. Chen, J. Ren and Q. Feng, "Vibration displacement measurements based on the phase tracking of an optical fiber Michelson interferometer," *Optical Engineering,* vol. 48, no. 4, 2009.

[30] P. Horowitz and W. Hill, "Feedback and Operational Amplifiers," in *The Art of Electronics*, 2nd ed., Cambridge University Press, 1989, pp. 175-261.

[31] T. Kwaaitaal, B. J. Luymes and G. A. van der Pijll, "Noise limitations of Michelson interferometers," *J. Phys. D: Appl. Phys.,* vol. 13, pp. 1005-1015, 1980.

[32] *HeNe Laser Overview,* ThorLabs.

[33] C. B. Scruby, "Some applications of laser ultrasound," *Ultrasonics,* vol. 27, pp. 195 - 209, 1989.

[34] J. W. Wagner and J. B. Spicer, "Theoretical noise limited sensitivity of clasical interferometry," *J. Opt. Soc. Am. B.,* vol. 4, no. 8, pp. 1316-1326, 1987.

[35] D. R. Lide, Ed., CRC Handbook of Chemistry and Physics, CRC Press, 2005.

5 Guided Elastic Waves in Anisotropic Media and the Mechanical Properties of Silicon

5.1 Introduction

Since the theoretical treatments of elastic waves performed by Lord Rayleigh [1] and Horace Lamb [2] resulted in what is now known as Rayleigh waves and Lamb waves, there has been an explosion of interest in these types of elastics waves for material characterisation and non-destructive testing. Rayleigh waves and Lamb waves are only two, perhaps the most common two, of a large list of elastic waves possible. This thesis is only interested in Lamb waves, or more correctly guided waves in thin plates[4]. At first, Lamb waves did not appear to have a use, other than of theoretical interest. It wasn't until the works completed by Mindlin [3],Worlton [4] and Viktorov [5], that the full potential of Lamb waves as a tool for material characterisation and non-destructive evaluation was realised.

This chapter gives a brief overview of Lamb waves in plates, similar to the membrane within a MEMS pressure sensor. Examples of the Lamb wave phase and group velocities are provided and a comparison of two different crystal orientations are demonstrated.

5.2 Guided elastic waves in plates

Lamb waves are waves that occur in thin plates, where the planar dimensions are much greater than the thickness and where the wavelength is of the order of the thickness. This provides upper and lower boundaries for the continuous propagation of the waves through the plate [6].

[4] The term "Lamb waves" strictly refers to guided waves in isotropic media. However the term is generally used to describe guided waves in any plate (or rod) regardless of plate configuration and as such, will continue to be used to describe these elastic waves.

Lamb waves are formed by the interference of multiple reflections and mode conversion of longitudinal and transverse waves at the surface of the plate. After some travel within the plate, these superpositions cause the formation of *wavepackets* or Lamb waves [6]. Three types of wave modes are possible in plates:

- Longitudinal waves
- Shear vertical waves
- Shear horizontal waves

Here, only the longitudinal and shear vertical waves are of interest. The shear horizontal waves contain no out of plane displacement and so can be neglected. The longitudinal (or compressional) waves are referred to as symmetric waves while the shear vertical (or flexural) waves are referred to as anti-symmetric waves. Each wave type can propagate independently of the other. To explain this in a different way, consider Figure 5.1 and Figure 5.2.

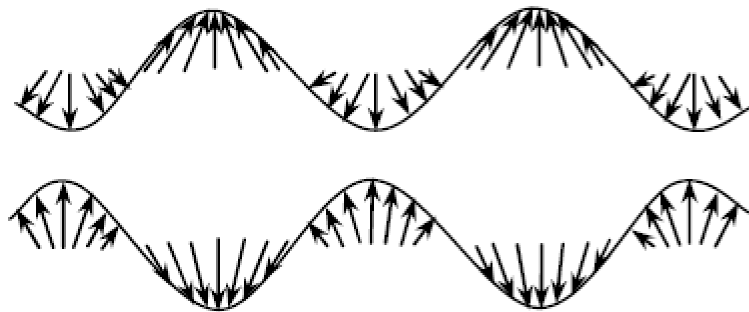

Figure 5.1: Symmetric Lamb wave modes [7].

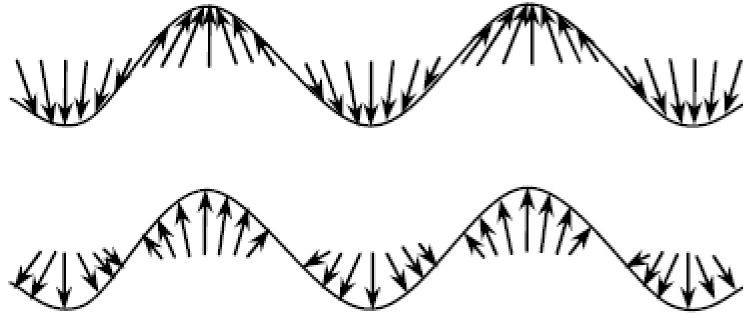

Figure 5.2: Anti-symmetric Lamb wave modes [7].

Figure 5.1 and Figure 5.2 show schematically a representation of the particle motion in the material. The symmetric and anti-symmetric modes are normally abbreviated to S_i and A_i (i=0, 1, …) respectively. The symmetric modes normally have a dominant in plane motion compared to the anti-symmetric modes dominant out of plane motion.

Each of these waves modes are governed by their own equation [8]. These equations are the well know Rayleigh-Lamb dispersion equations and are given below.

Symmetric modes

$$\frac{\tan(qh)}{\tan(ph)} = -\frac{4k^2qp}{(k^2-q^2)^2} \tag{5.1}$$

Anti-symmetric modes

$$\frac{\tan(qh)}{\tan(ph)} = -\frac{(k^2-q^2)^2}{4k^2qp} \tag{5.2}$$

Within these two equations, $h = {}^{d}/_{2}$ where d is the plate thickness, k is the wavenumber ($k = {}^{\omega}/_{c_p}$), ω is the angular frequency, c_p is the Lamb wave phase velocity and p and q are

$$p^2 = \frac{\omega^2}{C_L^2} - k^2 \qquad q^2 = \frac{\omega^2}{C_T^2} - k^2 \tag{5.3}$$

where C_L and C_T are the longitudinal and transverse wave velocities respectively. The velocities are a function of the wave's frequency and the plate thickness, making Lamb waves dispersive.

The longitudinal and transverse wave velocities can be related to the material elastic properties by [8, 9]

$$C_L = \sqrt{\frac{\lambda + 2\mu}{\rho}} = \sqrt{\frac{E}{\rho}\frac{(1-\nu)}{(1+\nu)(1-2\nu)}} \quad \textbf{5.4}$$

$$C_T = \sqrt{\frac{\mu}{\rho}} = \sqrt{\frac{E}{\rho}\frac{1}{2(1+\nu)}} \quad \textbf{5.5}$$

where λ and μ are the Lamé constants, and can be expressed as

$$\lambda = \frac{\nu E}{(1-2\nu)(1+\nu)} \qquad \mu = \frac{E}{2(1+\nu)} \quad \textbf{5.6}$$

E is Young's modulus, ρ is the material density and υ is Poisson's ratio. If C_L, C_T and ρ are known, Poisson's ratio and Young's modulus are given by [8]

$$\upsilon = \frac{1 - 2\left(\frac{C_T}{C_L}\right)^2}{2 - 2\left(\frac{C_T}{C_L}\right)^2} \quad \textbf{5.7}$$

$$E = 2\rho C_T^2(1+\upsilon) \quad \textbf{5.8}$$

The Rayleigh-Lamb wave equations are used to obtain velocity dispersion curves. These dispersion curves can either be phase velocity or group velocity dispersion curves and the choice of which to use ultimately depends on the measurement type and experimental set up. Lamb waves, like all waves can travel with both a phase and group velocity. The phase velocity is the velocity at which an individual component

of a wave propagates and is given as $c_p = {}^{\omega}/_{k}$ whereas the group velocity is the velocity of the guided wave packet and is given as $c_g = {}^{\delta\omega}/_{\delta k}$. The group velocity, which is also the direction of energy flow, is usually what is measured in experiments and is sometimes viewed as the velocity of the energy of the wave [10].

Figure 5.3 shows an example of a Lamb wave measured in a 50 μm thick silicon wafer (averaged 4096 times at a repetition rate of 10 Hz) using the experimental configuration detailed in Chapter 7. Figure 5.4 shows an example of a phase velocity dispersion curve while Figure 5.5 shows an example of the group velocity dispersion curve. dispersion curves were produced using a MATLAB program developed within the Centre for Ultrasonic Engineering [17]. It is clear that as the frequency increases, as do the number of modes, and so, theoretically, an infinite number of modes can exist in a plate, all of which are dispersive at some point. However, below a certain cut off threshold, only the two fundamental modes can propagate. This means the propagating wave spreads in space and time and close to the source, the detected signal is of similar shape to the input. Over time (and therefore distance) the signal spreads out and the peak amplitude decreases.

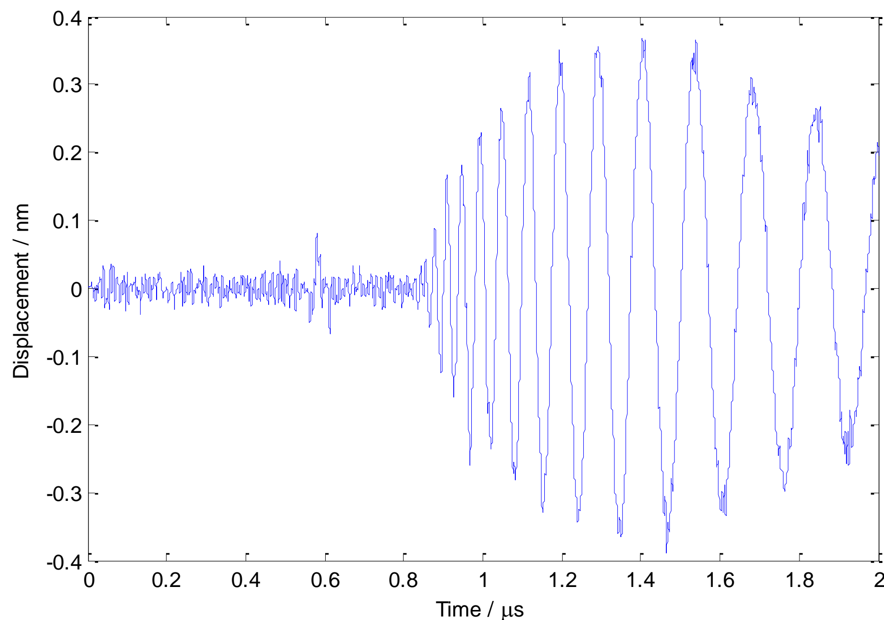

Figure 5.3: Example of a lamb wave measured in a 50 μm silicon wafer. Calibration procedure given in section 4.3.1.

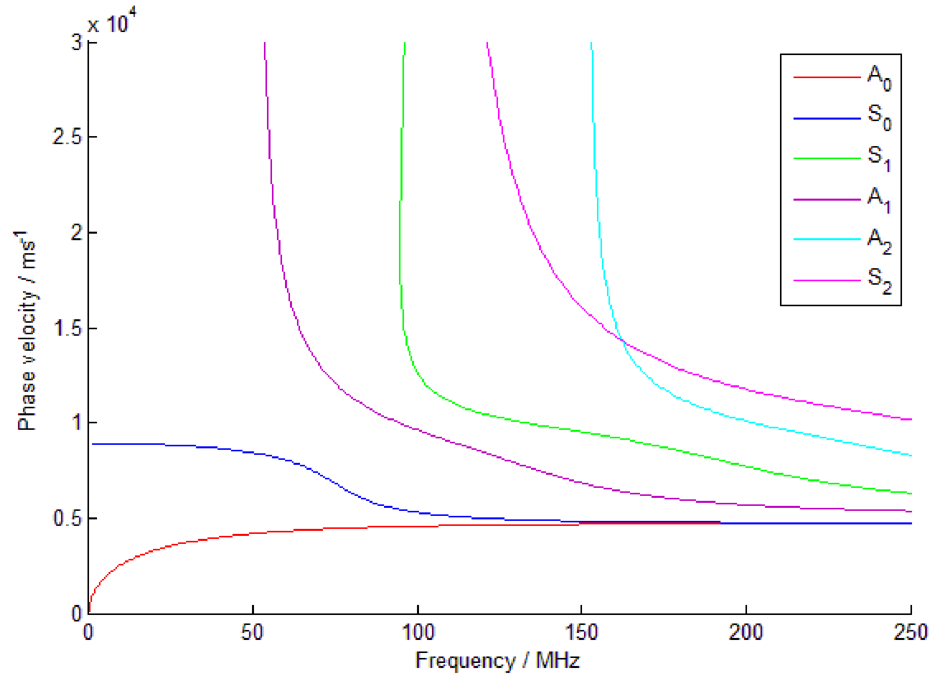

Figure 5.4: Lamb wave phase velocity dispersion curves for a 50 µm silicon wafer in the [110] direction.

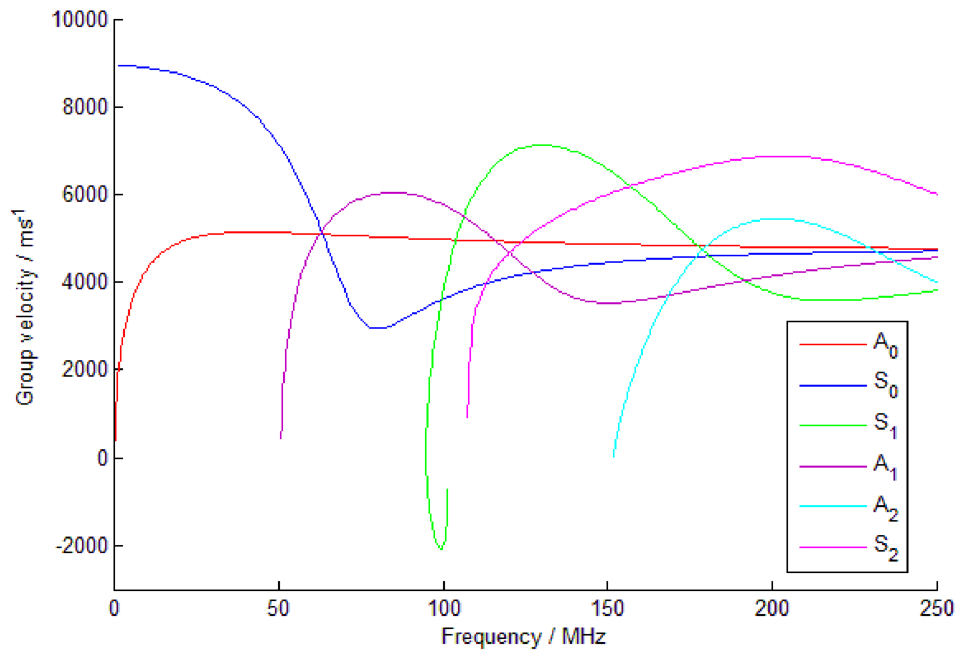

Figure 5.5: Lamb wave group velocity dispersion curves for a 50 µm silicon wafer in the [110] direction.

Normally the dispersion curves show the frequency thickness product on the x-axis. However the main objective of this thesis is to ultimately determine the thickness of a sample so only frequency is shown. It is clear to see in this case that with a thickness of 50 μm, the frequency thickness product of the onset of the Raleigh wave (*i.e.*, where the fundamental symmetric and anti-symmetric modes converge) would be approximately 5 MHzmm.

The non-dispersive, low frequency component of the S_0 mode is known as the plate wave velocity and is given by

$$\lim_{fd \to 0} c_s = \sqrt{\frac{E}{\rho(1-\upsilon^2)}} \qquad \textbf{5.9}$$

where c_s is symmetric Lamb wave velocity or plate wave velocity. As the frequency increases, the fundamental symmetric and antisymmetric modes converge to the Rayleigh wave velocity, C_R and the other non zero modes approach the shear wave velocity, C_T [8].

The dispersion equations and the resulting dispersion curves are used to describe the relationship between frequency, sample thickness and phase or group velocity. Figure 5.4 and Figure 5.5 show that

- The wave modes are a function of the product of the frequency and sample thickness.
- The lower order modes (A_0 and S_0) exist for all frequencies and the higher order modes (A_i and S_i (i = 1, 2, …)) appear with increasing frequency.
- There are regions of low dispersion for the lower order modes (≈50 MHz), before the higher order modes begin to appear.

5.3 A note on silicon crystal orientation

One surprising observation is that there is a continued variability in the measured values of basic properties such as Young's modulus in silicon. The title of a very

recent paper published in the Journal of Microelectromechanical Systems by Hopcroft *et al.* sums up the problem [11]. The paper entitled "*What is the Young's Modulus of Silicon?*" states that even with silicon being the most common single crystal material used in MEMS structures, the value of Young's modulus can vary by up to 45% depending on crystal orientation (E = 130 GPa for (100), 169 GPa for (110) and 188 GPa for (111)) however, many researchers have over simplified this problem resulting in inaccuracies in many models and designs.

The two most common orientations are the [100] and [111] orientations, however, for micromachining purposes, the [110] (Figure 5.6) is often used as this cleaves more cleanly than other orientations. [111] wafers are used less frequently as they cannot easily be etched using wet anisotropic methods. To contradict this Kim *et al.* explains that (111) silicon may be a better material for MEMS [12]. They point out that the mechanical properties are transversely and vertically isotropic for silicon (111) compared to the anisotropic nature of (100) and (110) silicon, showing that (111) is less sensitive to device orientation with respect to crystallographic orientation.

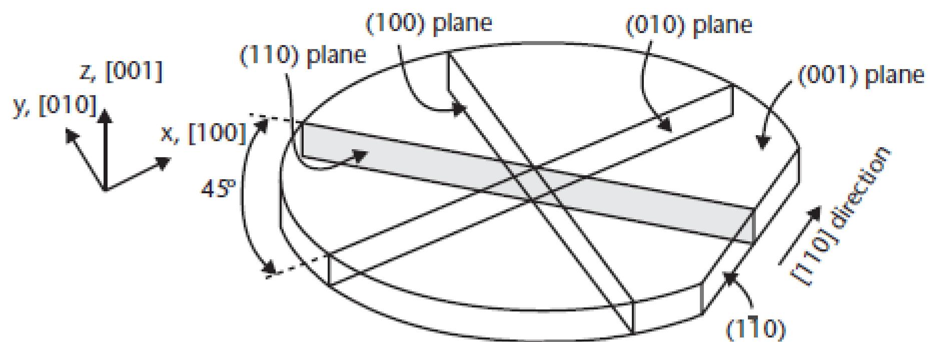

Figure 5.6: Image identifying various planes in a wafer of (100) orientation [16].

When silicon wafers are manufactured, flats are cut into the wafers, known as *orientation flats*. This flat has a precision of approximately 3° [13]. Figure 5.7 shows four examples of primary and secondary flats cut into (100) and (111) wafers with

different dopant types. The primary flats are used to help orientate the wafers in the cassettes and the secondary flats are used to identify conductivity type.

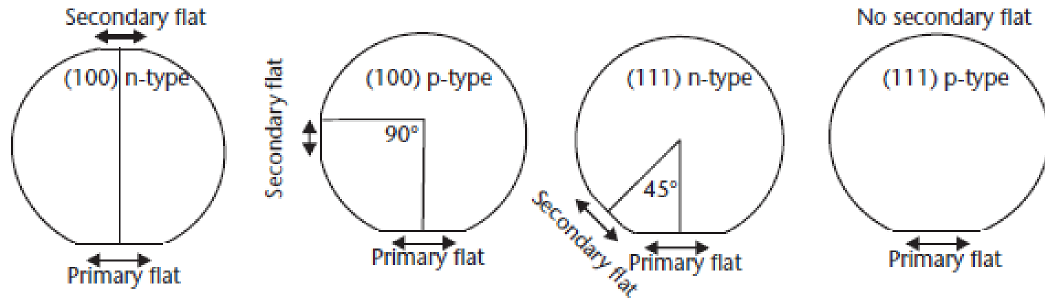

Figure 5.7 The primary and secondary flats of {100} and {111} wafers for both n-type and p-type doping [16].

.

Ultimately, the three properties of interest in MEMS structures are Young's modulus, Poisson's ratio and thickness. It should be noted that when discussing material properties, the measured value should be independent of the test method.

In order to measure the mechanical properties of a MEMS structure, a number of challenges must be overcome [14]:

1. The specimen must be mounted.
2. Its dimensions must be measured.
3. A force or displacement must be applied to deform the structure.
4. The resulting displacement must be measured.

The American Society for Testing and Materials (ASTM) does have a standard (ASTM E-345-93) [15] that describes the procedure for measuring metallic foils of thickness less than 150 µm, with large length and width dimensions. However, this standard can only be used as guidance as it does not apply to MEMS structures or indeed anisotropic materials.

Considering the statement above regarding the variation in Young's modulus with respect to crystal orientation, the obvious question is, how does this affect the dispersion curve? Figure 5.8 shows phase velocity dispersion curves for Lamb waves in the [100] and [110] directions in a silicon wafer.

Table 5.1 gives the material properties used to produce the dispersion curves.

Table 5.1: Material properties used for dispersion curve analysis [11].

	[100]	[110]
Young's modulus, E	130 GPa	169 GPa
Poisson's ratio, υ	0.28	0.36
Shear modulus, μ	79.6 GPa	50.9 GPa

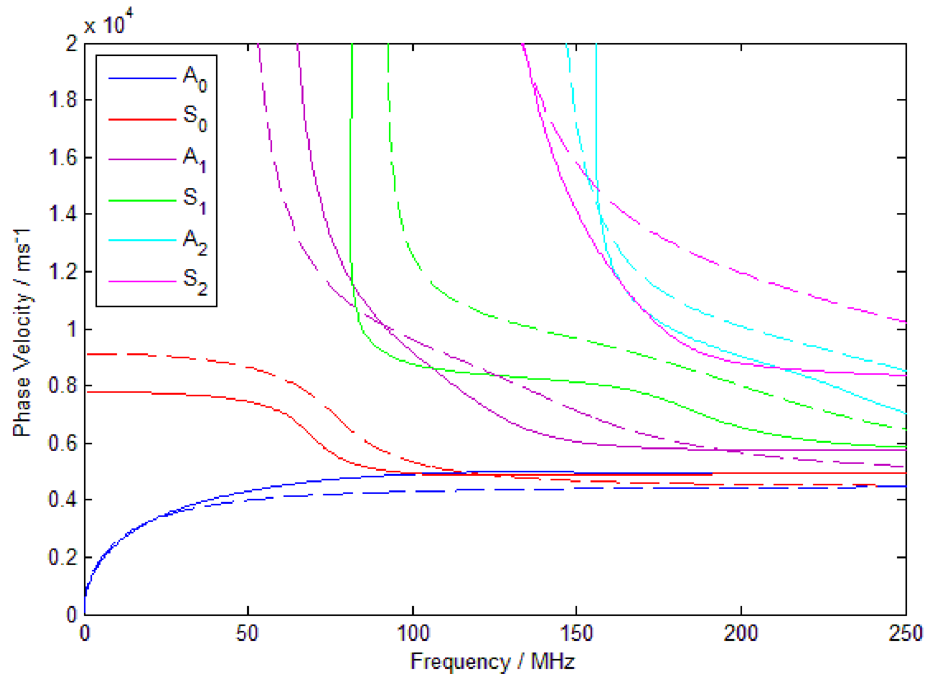

Figure 5.8: Lamb wave phase velocity dispersion curves for a 50 µm silicon wafer in the [100] and [110] direction. Solid lines refer to the [100] direction and dashed lines refer to the [110] direction.

Probably the most striking feature in Figure 5.8 is that there is a huge variation in the dispersion curves with a change of material properties, contained within the same material sample. Two very clear observations are:

- The plate velocity is ≈7800 $ms^{-1}$for the [100] direction, compared with ≈9100 ms^{-1} for the [110] direction, which is a 14% increase.
- The Rayleigh velocity is ≈4900 ms^{-1} for the [100] direction, compared with ≈4500 ms^{-1} for the [110] direction, which is a 8% decrease.

While there are other noticeable differences in the dispersion curves between the two orientations, the two listed above prove the importance of the correct knowledge of crystal orientation before beginning any characterisation experiments on silicon wafers or MEMS structures.

5.4 Conclusions

The propagation of Lamb waves within a structure is demonstrated and the equations for the determination of material properties are presented. The dispersive nature of Lamb waves is discussed and the importance of crystal orientation is illustrated in an example, which shows the effect on the dispersion curves within a silicon wafer. It is shown that to be able to accurately obtain and use a dispersion curve for material characterisation, the knowledge of crystal orientation is critical. This is the focus of the paper by Hopcroft *et al* [11] and the criticality of this is demonstrated.

5.5 References

[1] Lord Rayleigh, “On the free vibrations of an infinite plate of homogeneous isotropic elastic matter,” *Proc. Lond. Math. Soc.,* vol. 20, pp. 225 - 237, 1889.

[2] H. Lamb, “On waves in an elastic plate,” *Proc. R. Soc. Lond. A,* vol. 93, no. 648, pp. 114 - 128, 1917.

[3] R. D. Mindlin, “Waves and vibrations in isotropic elastic plates,” in *First Symposium on Navel Structural Mechanics*, J. N. Goodier and N. J. Hoff, Eds., Oxford: Pergamon, 1960, pp. 199 - 232.

[4] D. C. Worlton, “Experimental confirmation of Lamb waves at megacycle frequencies,” *J. Appl. Phys.,* vol. 32, pp. 967 - 971, 1961.

[5] I. A. Viktorov, Rayleigh and Lamb Waves: Physical Theory and Applications., New York: Plenum Press, 1967.

[6] J. L. Rose, Ultrasonic Waves in Solid Media, Cambridge University Press, 2004.

[7] Z. Su and L. Ye, "identification of damage using lamb waves: from fundamentals to applications," in *Lecture Notes in Applied and Computational Mechanics*, vol. 48, F. Pfeiffer and P. Wriggers, Eds., Springer, 2009, pp. 15 - 53.

[8] W. P. Rogers, "Elastic property measurement using Rayleigh-Lamb waves," *Res. Nondestr. Eval,* vol. 6, pp. 185 - 208, 1995.

[9] S. Timoshenko and J. N. Goodier, Theory of Elasticity, McGraw-Hill, 1951.

[10] D. E. Chimenti, "Guided waves in plates and their use in materials characterizations," *Appl. Mech. Rev.,* vol. 50, no. 5, pp. 247-284, 1997.

[11] M. A. Hopcroft, W. D. Nix and T. W. Kenny, "What is the Young's modulus of silicon?," *Journal of Microelectromechanical Systems,* vol. 19, no. 2, p. 229, 2010.

[12] J. Kim, D. Cho and R. S. Muller, "Why is (111) silicon a better mechanical material for MEMS?," in *Proceedings of the 11th International Conference on Solid-state Sensors and Actuators (Transducers' 01)*, Munich, Germany, 2001.

[13] M. J. Madou, "Fundamentals of Microfabrication: The Science of Miniaturization," 2nd ed., CRC Press, 2002.

[14] W. N. Sharpe, "Mechanical Properties of MEMS Materials," in *The MEMS Handbook*, M. Gad-el-Hak, Ed., CRC Press, 2002.

[15] "Standard Test Methods of Tension Testing of Metallic Foil," ASTM International, ASTM E-345-93, 2008.

[16] N. Maluf and K. Williams, An Introduction to microelectromechanical systems engineering, 2nd ed., Artech House, 2004.

[17] I. Veres, *Private Communication.*

6 Dependence of Optical Wavelength on Laser Generated Ultrasound

6.1 Introduction

The first stage in the generation of acoustic waves using pulsed lasers is the absorption of energy by the material under investigation. For metals, such as steel or aluminium, the optical properties are fairly similar and well known. But what about materials used in MEMS structures? For the majority of MEMS devices, silicon is the material of choice. However, this can be doped, in some cases quite heavily, affecting absorption characteristics. Also, metallic films, such as aluminium, chromium or copper, on silicon substrates are increasingly common, with copper overtaking aluminium as the primary metal in semiconductor devices. These materials all have different optical and thermal properties and it is not a simple case of "picking" a laser off a shelf and assuming it will efficiently generate acoustic waves. This chapter investigates the dependence of optical wavelength on the relative efficiency of ultrasonic generation. Three wavelengths are investigated, the fundamental (1064 nm), second (532 nm) and third (355 nm) harmonics of a Q-switched Nd:YAG laser. One similar study has been previously performed by Flannery *et al.* [1]. However, they studied surface waves in bulk samples of steel, silicon nitride and silicon carbide.

This chapter builds on the principal research published by Flannery *et al.* and concentrates on materials used within the MEMS industry, namely silicon, aluminium, copper and chromium.

6.2 Materials under investigation

While there is an increasingly large number of materials used in MEMS devices, such as silicon, silicon dioxide, silicon nitride, quartz, silicon carbide, diamond,

gallium arsenide and aluminium nitride to name a few [2], this study is only concerned with basic elements. Both bulk materials in the form of plates and thin films on silicon were studied. All bulk materials were purchased from Goodfellow Materials [3] and details of each are shown in Table 6.1

Table 6.1: Specification of materials studied.

Material	Thickness	Preparation
Aluminium	320 µm	Polished
Copper	300 µm	Polished
Chromium	500 µm	None
n-type Silicon (100)	381 µm	None

Various metals were also evaporated onto 381 µm thick n-type silicon (100) wafers using an Edwards E306 Coating System. Details of these samples are given in Table 6.2

Table 6.2: Specification of thin films studied.

Material	Thickness	Preparation
Aluminium film on silicon substrate	118 nm / 381 µm	Film evaporated onto silicon wafer
Chromium film on silicon substrate	97 nm / 381 µm	Film evaporated onto silicon wafer
Copper film silicon substrate	188 nm / 381 µm	Film evaporated onto silicon wafer

The thicknesses of the thin films were measured with an Alpha Step IQ stylus surface profiler and are shown below in Figure 6.1 to Figure 6.3. The surface profiler scanned the surface at a rate of 10 μms^{-1} and sampled at 1000 Hz with a resolution of 10 nm.

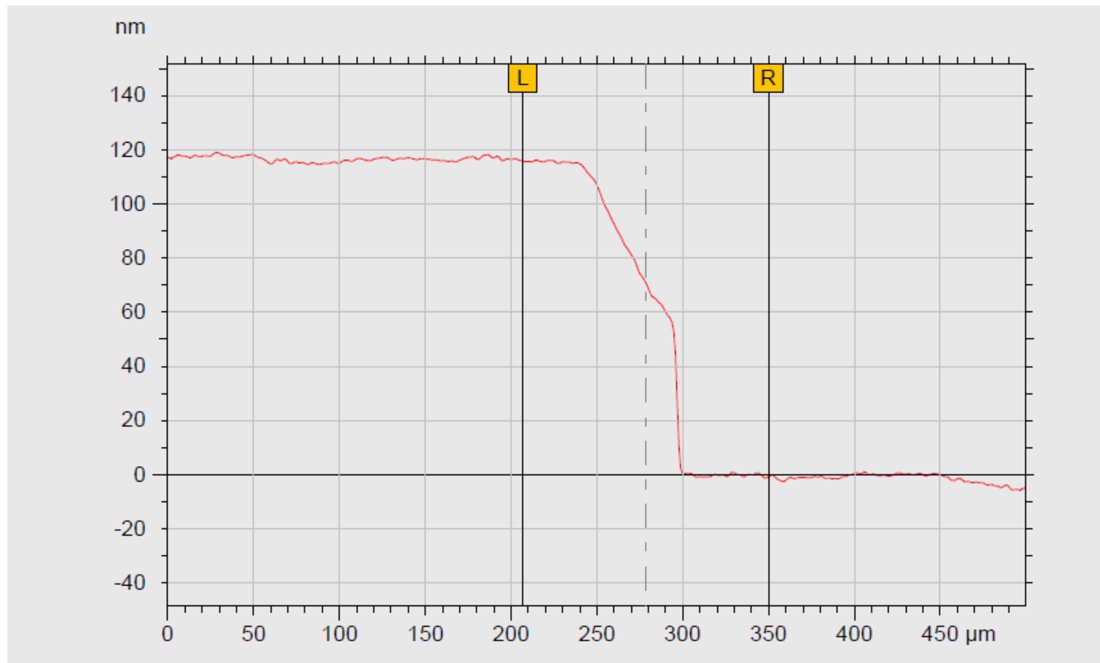

Figure 6.1: Stylus profile measurement of aluminium film on silicon substrate, thickness = 118 nm.

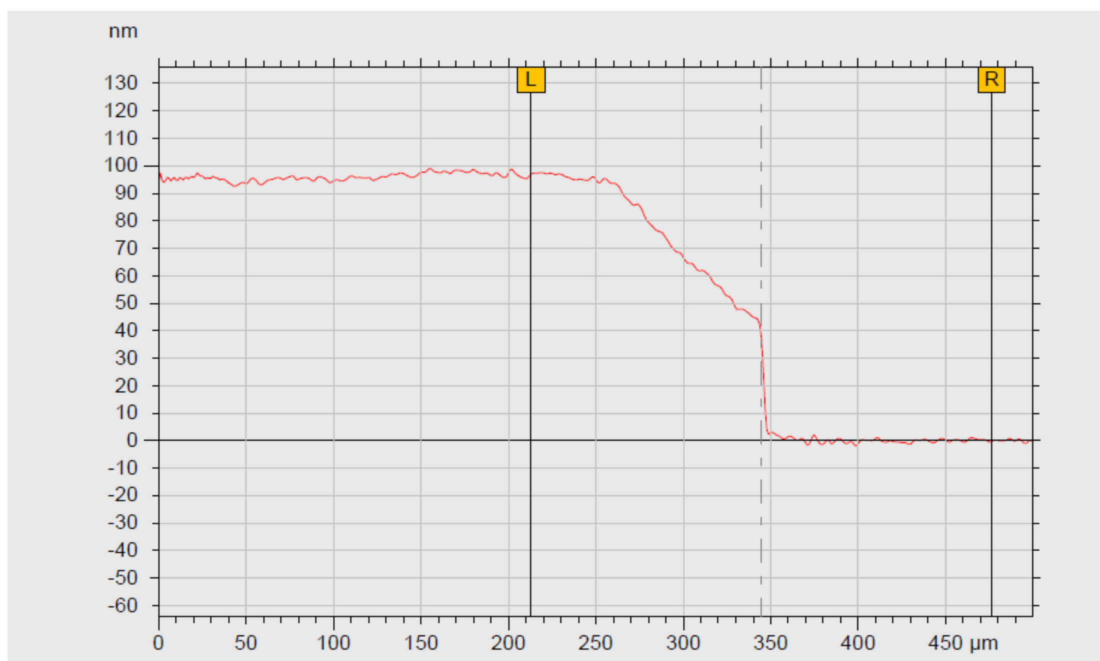

Figure 6.2: Stylus profile measurement of chromium film on silicon substrate, thickness = 97 nm.

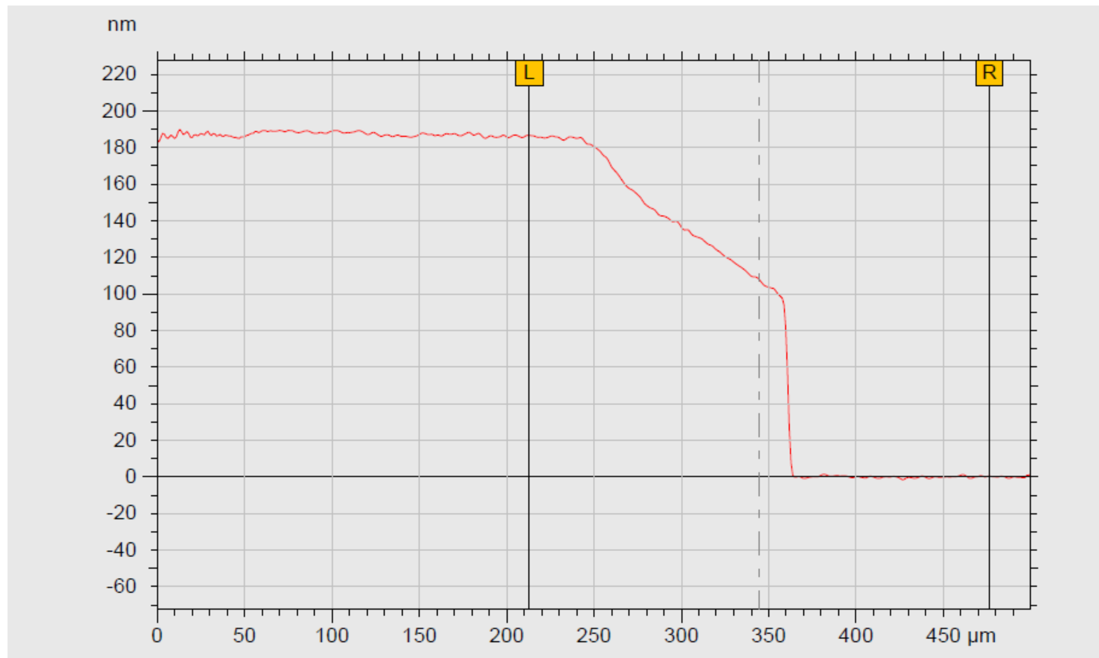

Figure 6.3: Stylus profile measurement of copper film on silicon substrate, thickness = 188 nm.

All samples were protected as much as possible, using gloves when handling samples and returning each sample to its protective case, but ultimately were subjected to atmospheric contamination.

6.3 Experimental Method

Guided acoustic waves were generated in the samples described above using a Q-switched Nd:YAG laser. The laser was a Quantel Brilliant B laser system. The laser operated at a wavelength of 1064 nm, with a maximum pulse energy of 850 mJ. Three additional bolt-on modules were also available. The first was a beam attenuator. This basically consisted of a half waveplate and a polariser, which could be rotated to reduce the output power of the laser. The work in this thesis was only concerned with ultrasonic generation in the thermoelastic regime, so the peak output power used was approximately 2 MW and lower. The other two modules were the 2nd and 3rd harmonic generator modules producing 532 nm and 355 nm respectively. A conversion efficiency of approximately 1:0.4:0.1 was obtained with the two harmonic generators. The laser beam was directed and focused onto the surface of

the samples using a cylindrical lens of focal length equal to 150 mm, as shown in Figure 6.4. The advantage of using a cylindrical lens is enhanced directionality of the acoustic wave, perpendicular to the major axis of the irradiated area. This increases the signal to noise ratio at the detector and also lowers the energy density, avoiding ablation [4]. The focused line width is dependent on wavelength, and so the focus was adjusted with the different wavelengths to keep power density constant. The pulse energies were measured using a Gentec Solo PE power meter with a XLP12-3S-H2-D0 head. The pulse energies used are shown in Table 6.3 as follows:

Table 6.3: Laser pule energies used at each wavelength.

	1064 nm	532 nm	355 nm
1	13.17 mJ ± 0.17 mJ (1.3%)	12.00 mJ ± 0.27 mJ (2.2%)	12.29 mJ ± 0.20 mJ (1.3%)
2	10.77 mJ ± 0.18 mJ (1.7%)	9.42 mJ ± 0.15 mJ (1.6%)	9.35 mJ ± 0.20 mJ (1.3%)
3	7.68 mJ ± 0.13 mJ (1.7%)	7.19 mJ ± 0.17 mJ (2.4%)	7.32 mJ ± 0.13 mJ (1.3%)
4	5.35 mJ ± 0.10 mJ (1.8%)	4.89 mJ ± 0.11 mJ (2.2%)	4.70 mJ ± 0.12 mJ (1.3%)
5	3.14 mJ ± 0.09 mJ (2.8%)	2.39 mJ ± 0.11 mJ (4.6%)	2.42 mJ ± 0.10 mJ (4.1%)

The line widths with cylindrical lens focus were marked on burn paper and using an optical microscope, were measured to be approximately 100 µm in width and 8 mm in length. Due to slight misalignment, although the line width was adjusted to compensate for the change in wavelength, the distance between the generation source and detector was also consequently adjusted. The acoustic waves were detected using a Poytec OFV 512 fibre laser vibrometer with a Polytec OFV 2700 ultrasonics vibrometer controller, shown schematically in Figure 6.4. The vibrometer has a displacement bandwidth of 20 MHz. Since the thickness of the silicon wafer was

approaching millimetre thickness, the acoustic waves generated were of a lower frequency. This made the Polytec laser vibrometer a better choice than the Michelson interferometer described in chapter 4. The signals were captured and recorded using an Agilent Infiniium 54832D MSO oscilloscope. For the case of the thin films, the silicon substrate was half coated with each of the metals as illustrated in Figure 6.5.

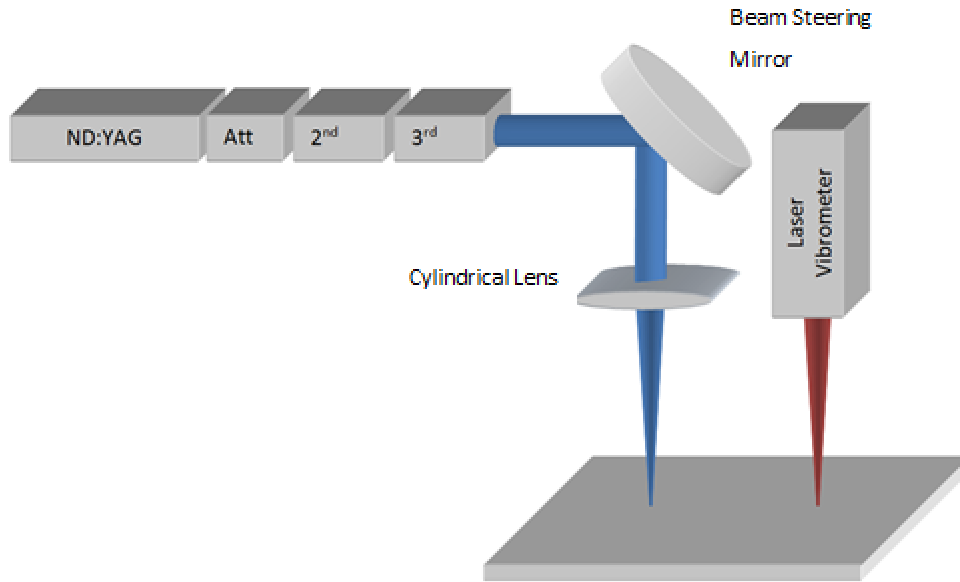

Figure 6.4: Schematic of experimental setup showing generation laser with attenuator, 2nd and 3rd harmonic generator, focusing the beam onto the surface with a cylindrical lens. Also shown is the detection system, a laser vibrometer.

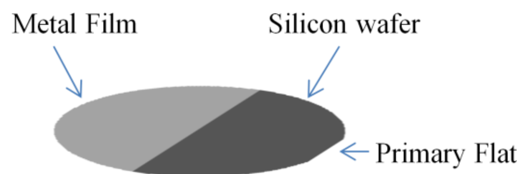

Figure 6.5: Metallic thin film coating on silicon substrate.

An example of a typical Lamb wave is shown in Figure 6.6. In this particular example, the Lamb waves were generated in a silicon wafer with a 100 nm thin film coating half of the wafer using the 2nd harmonic generator. The pulse energies were varied from approximately 13 mJ to 5 mJ (see

Table 6.3) and the amplitudes of the detected waves were measured. The results presented were obtained by measuring the peak amplitude of the dominant A_0 mode. As an example and to provide a rough estimate, in Figure 6.6, the maximum amplitude of the A_0 mode produced with pulse energy of approximately 12 mJ is approximately 0.7 nm.

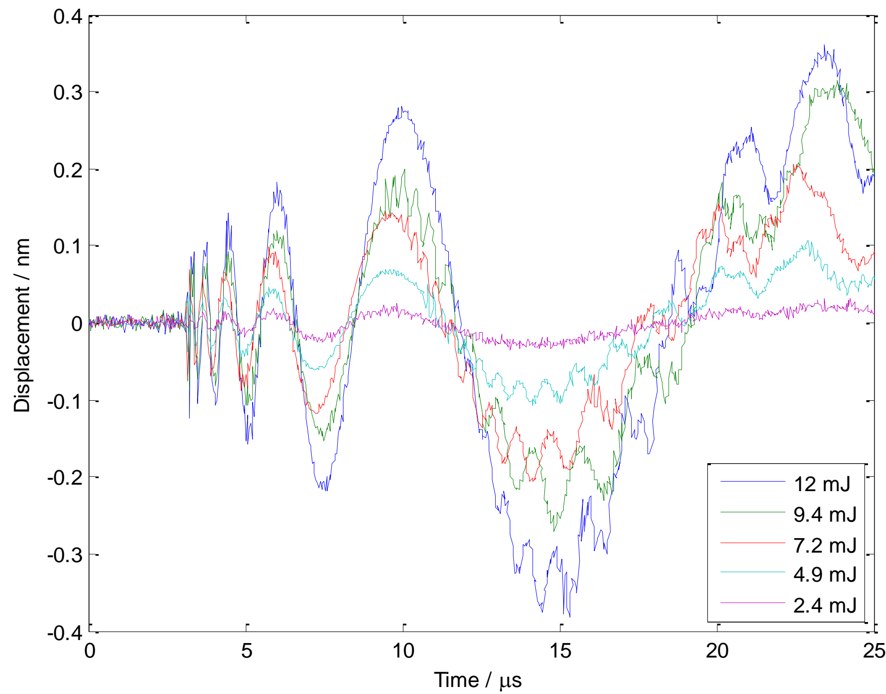

Figure 6.6: Lamb waves generated in a silicon wafer with chromium thin film at differing pulse energies using 532 nm light.

Figure 6.7 shows how the amplitude of the generated Lamb waves varies with optical excitation wavelength. Again, these measurements were taken using a 9.8 mJ pulse. The DC offsets are for presentation purposes only. Both Figure 6.6 and Figure 6.7 were averaged 4096 times with a repetition rate of 20 Hz.

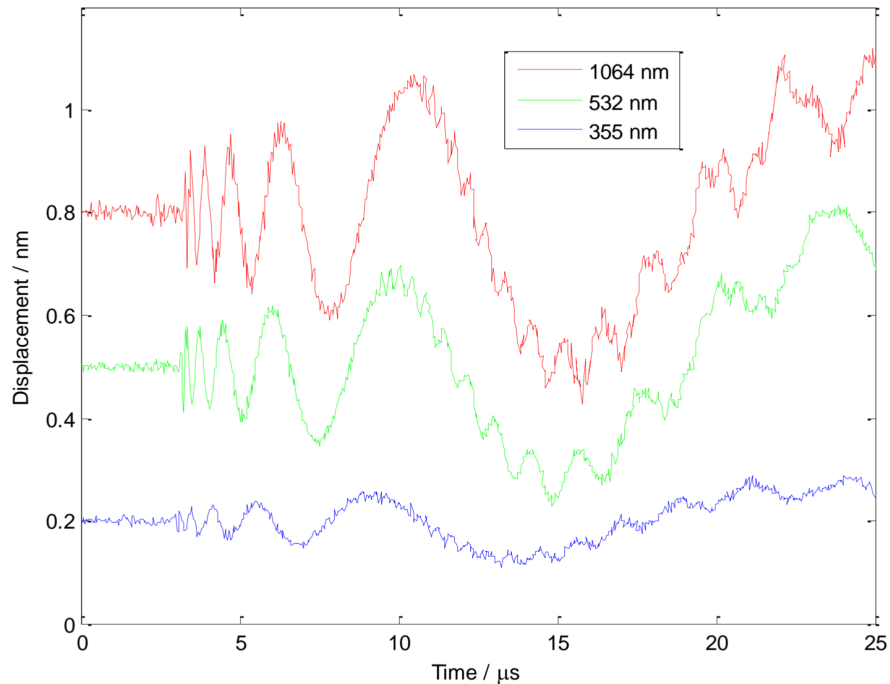

Figure 6.7: Lamb waves generated in a silicon wafer with chromium thin film using three different wavelengths, 1064 nm, 532 nm and 355 nm, with a pulse energy of 9.8 mJ.

6.3.1 Errors in the Measurement Process

The experiments detailed in section 6.3 were subject to a number of experimental errors that either could not be controlled or were not considered until later. These errors are outlined below.

- While every effort was made to keep the line width equal when the second and third harmonic generators were added, the measurement of line width was made using an optical microscope. Each width corresponding to a different wavelength was based on the width obtained at the fundamental wavelength, *i.e.* 1064 nm and every effort was made to normalise the other widths to this, but in practice, this would never have been fully achievable. Relative to the line produced by the fundamental wavelength, the line width tolerance was ≈80 µm ± 20%.

- Trying to optimise the line width meant slightly adjusting the focus of the lens used to direct the beam to the sample. Referring to Figure 6.4 shows that the beam travelled horizontally before being directed downwards to the sample surface. It was noticed afterwards that this caused a slight deviation in the incident angle of the beam. This was first noticed when comparing acoustic waveforms at each wavelength, *i.e.* the arrival times were slightly different. However, more importantly, this would have had an effect on the value of the optical properties, namely the refractive index and the extinction coefficient. The deviation in angle was less than 1° and this is not considered large enough to have an observable effect on the results.
- The third error is in the preparation of the sample prior to the experiments. For obvious reasons, the thin films and silicon sample could not be polished, but every effort was made to polish the aluminium and copper plates before experimentation. The polish used was a 6 μm diamond grit followed by a 1 μm diamond grit. In the case of the chromium sample, polishing had no effect on the surface. As a result, the return beam of the vibrometer was of a lower quality than the other samples studied.

6.4 Results and Discussion

6.4.1 Acoustic wave generation in the metals

Three metallic plates were studied to investigate the effects of optical wavelength on the acoustic waves generated. Each metal will be treated individually with the results being presented below[5].

As previously stated, the first stage in generating acoustic waves using pulsed lasers is the absorption of electromagnetic energy. The main driver of how much energy is absorbed by a material at a particular wavelength is the reflectivity of the material. Although reflectivity can be measured using ellipsometry, for example, that option

[5] It needs to be stated that the laser used for acoustic wave generation developed a fault nearing the end of the experiments for this work. Because of this it was not possible to obtain a result at 355 *nm* for chromium. This was the last material to be tested.

was not available, so values for reflectivity were taken from the literature and will be referenced where required.

The optical properties of metals are determined by their conduction electrons. These electrons move freely through the ion lattice and can be thought of as a plasma and as such will respond to incident electromagnetic radiation, depending on frequency.

The dielectric constant obtained from the Drude theory is directly related to the optical properties of materials and is defined as follows

$$\epsilon = \epsilon_1 + i\varepsilon_2 = (n + ik)^2 \quad \textbf{6.1}$$

where $$\epsilon_1 = n^2 - k^2 \quad \textbf{6.2}$$

and $$\epsilon_2 = 2nk \quad \textbf{6.3}$$

ε_1 and ε_2 are the real and imaginary parts respectively of the dielectric constant and n and k are the real and imaginary parts respectively of the complex refractive index of a material. The real part of the complex refractive index, known as the refractive index and the imaginary part, known as the extinction coefficient together make up the complex refractive index, defined below.

$$N = n + ik \quad \textbf{6.4}$$

ε_1, ε_2, n and k are all frequency dependant.

Reflectivity[6] is a function of the materials' refractive index, n (phase velocity) and its extinction coefficient, k (amount of absorption loss) and is given by

[6] All values for reflectivity assume normal incidence.

$$R = \frac{(1-n)^2 + k^2}{(1+n)^2 + k^2} \quad \textbf{6.5}$$

A consequence of the Drude theory is that for longer wavelengths, materials with high numbers of free carriers (*e.g.* metals) are almost perfect reflectors. Reflectivity must not be confused with reflectance, where reflectivity is a function of the refractive index and extinction coefficient values at the surface of a material and reflectance is a function of both these and sample thickness. This is not relevant in the discussion of acoustic waves in metallic sample where the skin depth is on the order of 10's of nanometers, but it will be discussed in the acoustic waves in semiconductor section.

The extinction coefficient is related to the absorption coefficient by

$$\alpha = \frac{4\pi k}{\lambda} \quad \textbf{6.6}$$

and the optical penetration depth (or skin depth) δ by

$$\delta = \frac{1}{\alpha}\left(or\ \frac{\lambda}{4\pi k}\right) \quad \textbf{6.7}$$

The radiation that is incident on the material has an energy that is transferred to the lattice upon absorption. This energy transfer generates heat through lattice collisions. The heat, as described in Chapter 3 is the thermal diffusion length and is independent of optical frequency. This is due to the wavelength dependence of the effective diffusion length. The extinction coefficient defines how much light is absorbed by a particular material and this, through equation 6.6 and equation 6.7 also determines the average distance travelled by a photon before getting absorbed. δ is also the distance where the intensity of radiation is reduced by $1/e$ (≈36%) of its original intensity, as a function of depth, x_3. The thermal diffusion length is independent of

optical frequency. However, if the optical penetration depth is large, this will in turn increase the thermal diffusion length.

It was mentioned above that the electrons can be treated as a plasma and respond to electromagnetic radiation depending on frequency. To expand on this, metals have a characteristic frequency, known as the plasma frequency, ω_p. This plasma frequency relates electron density to optical properties and determines the point at which the electrons cannot respond fast enough to the frequency of the incident radiation, screening the electric field from the material, in other words, it determines the point at which the metal becomes transparent to the incoming radiation. The plasma frequency is given by

$$\omega_p = \sqrt{\frac{N_e q^2}{m_e \varepsilon_0}} \qquad \textbf{6.8}$$

where N_e is the material's electron density, q is the electronic charge, m_e is the mass of the electron and ε_0 is the permittivity of free space. The plasma frequency is the point at which the square of the refractive index is equal to the square of the extinction coefficient (*i.e.* $n^2 = k^2$) or when the real part of the dielectric constant, ε_1 is equal to zero. This is illustrated in Figure 6.8 which shows the point where $n^2 = k^2$ and ε_1 crosses the zero axis in copper. Below the plasma frequency, the real part of the dielectric constant is negative.

The plasma frequency can be thought of as dividing the frequency range into two parts. The first is the low frequency (increasing wavelength) part where the complex refractive index has an imaginary part and waves are attenuated. This occurs above 155 nm in copper. The second part is where the refractive index is real and the material becomes transparent (below 155 nm in copper). For metals, the plasma frequency occurs in the ultraviolet range of the electromagnetic spectrum.

This immediately tells us that the plasma frequency is much higher than the frequency of radiation used in metal samples detailed in this work, *i.e.* below our wavelength range of interest.

Table 6.4: Plasma frequencies for selected metals

Material	Plasma frequency / Hz	Wavelength corresponding to plasma frequency / nm
Aluminium[7]	3.61×10^{15}	83
Chromium [5]	1.69×10^{15}	177
Copper[7]	1.93×10^{15}	155

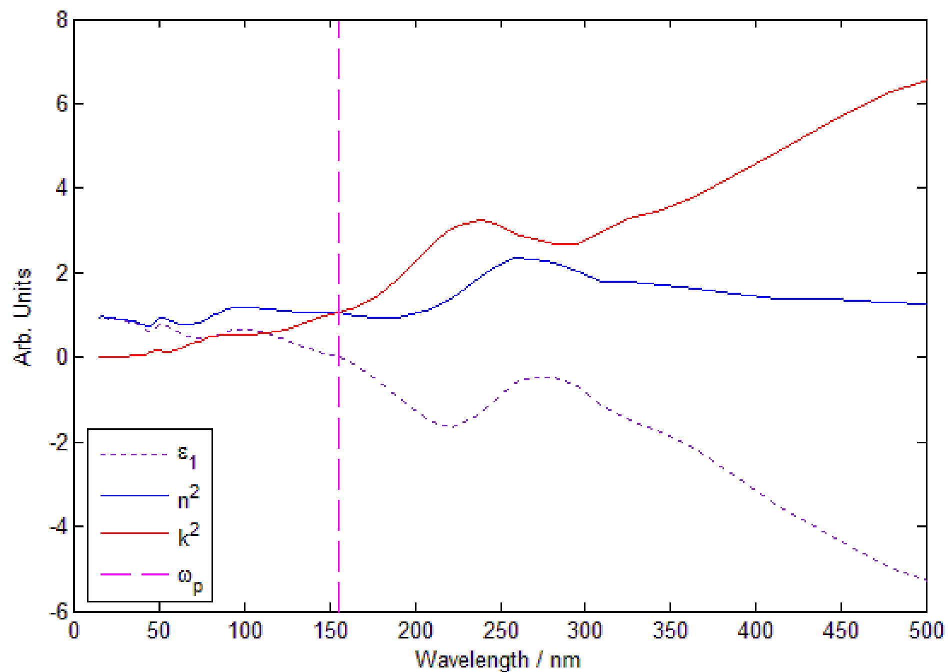

Figure 6.8: Relationship between plasma frequency, refractive index, extinction coefficient and real part of the dielectric constant in copper.

[7] Calculated from [6]

6.4.1.1 Aluminium

Figure 6.10 illustrates the increase in acoustic wave amplitude as a function of optical energy. Across the wavelength range of interest, aluminium has a very high reflectivity, demonstrated in Table 6.5. This can be further seen in Figure 6.9. It can be seen that this results in large changes in absorbed power. The data used to produce Figure 6.9 is taken from [6] (ref [7]).

Table 6.5: Percentage of absorbed energy into aluminium.

	1064 nm	532 nm	355 nm
Aluminium	5%	8%	8%

From Figure 6.9, it is clear that aluminium is highly reflective across the near UV – visible – near IR region. It is also clear the reflectivity drops off extremely rapidly at approximately 83 nm. This is the plasma frequency for aluminium and the gradient is related to the relaxation time.

From this information, one can begin to build up a picture of what kind of acoustic wave amplitudes would be expected.

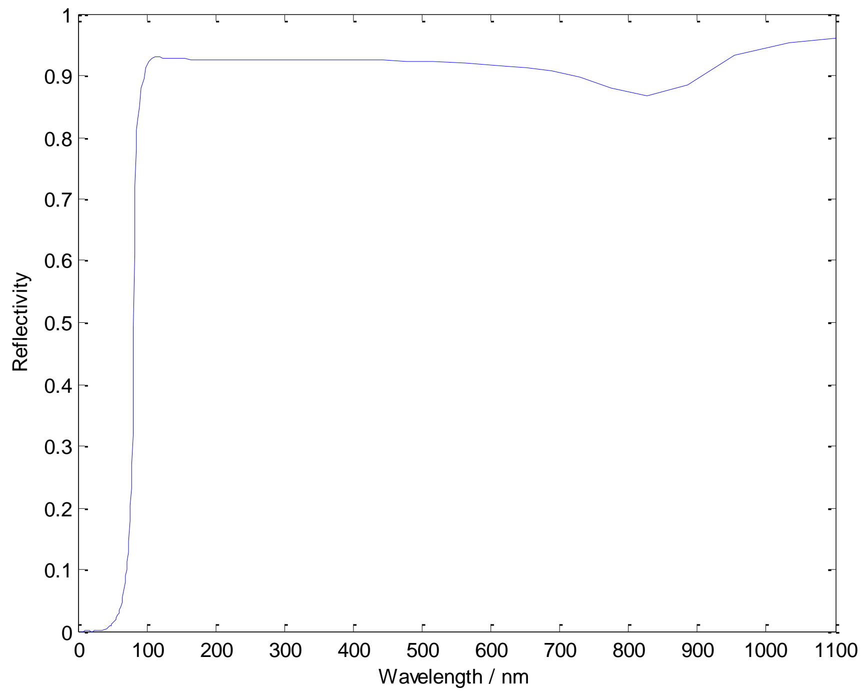

Figure 6.9: Reflectivity of aluminium in vacuum.

Due the relatively flat nature of aluminium's reflectivity over the wavelength range of interest, it would be expected that the choice of optical wavelength used to generate acoustic waves would not matter. As can be seen in Figure 6.10 this is the case.

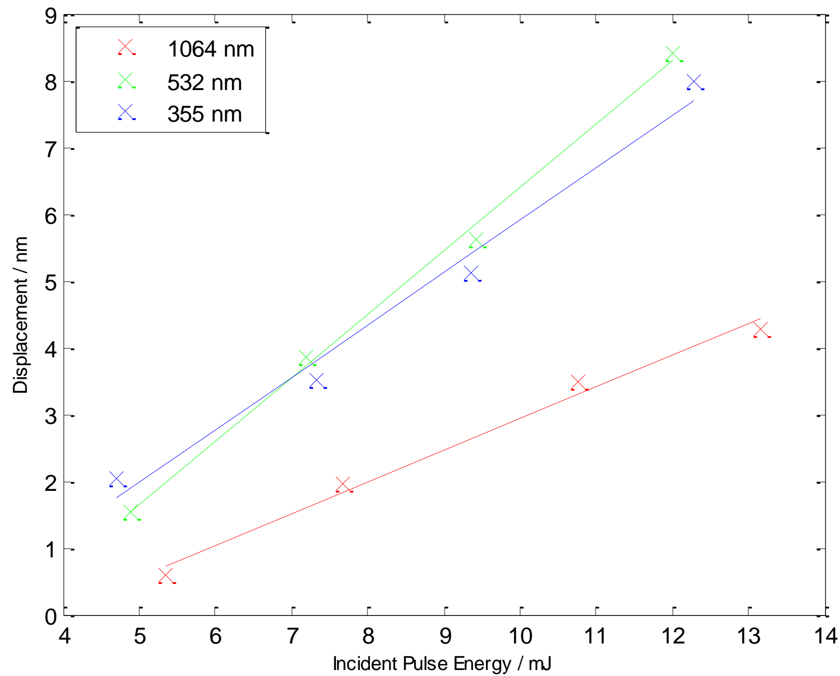

Figure 6.10: Peak to peak amplitude representation of acoustic waves generated in an aluminium plate at three optical wavelengths and varying pulse energies.

Figure 6.10 needs to be corrected to account for the fact that only a percentage of the incident radiation is absorbed into the material, contributing to heating and thermal stresses as shown in Figure 6.11.

Figure 6.10 and Figure 6.11 shows the amplitudes of the acoustic waves vary linearly with pulse energy. The fitted trendlines give an indication of the linearity of the measurements, but also highlight the errors within each measurement, discussed in section 6.3.1.

Table 6.6 shows the results at each specific wavelength of interest. The relative efficiency value quoted is the gradient of the 1064 nm line (baseline) divided by the gradient of the other two lines. From this, the reciprocal is taken. A result of >1indicates a higher relative efficiency, *i.e.* more efficient compared to the 1064 nm baseline. The amplitude of the waves generated using 1064 nm light is less than the other two however, less energy is absorbed at this wavelength. Taking the

measurements at 1064 nm as a baseline, it is clear that light at 532 nm and 355 nm is slightly more efficient at generating acoustic waves. Bearing in mind that the values for reflectivity and optical penetration depth are all nearly equal across the spectrum of interest, this result is not surprising. It would be expected that the efficiency of the 532 nm and 355 nm wavelengths to be slightly lower than they were, but due to the very similar nature of the optical constants, the slightest misalignment in the experimental setup will affect this. It is easy to conclude that the choice of optical wavelength is not critical for generating acoustic waves in aluminium.

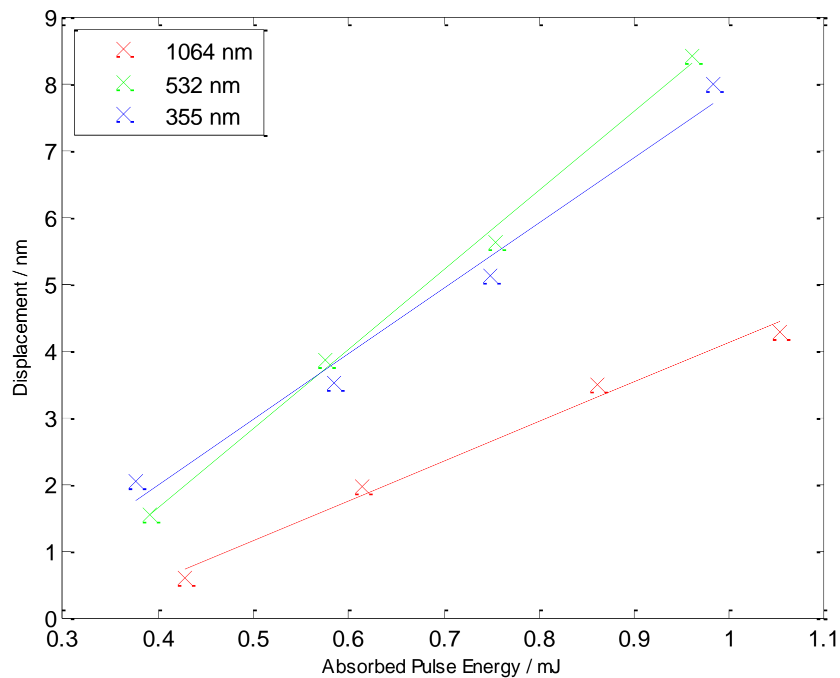

Figure 6.11: Generated acoustic wave amplitudes in aluminium, compensated for optical reflectivity.

Table 6.6: Characterisation of acoustic waves as a function of wavelength in aluminium.

Wavelength	1064 nm	532 nm	355 nm
% Energy Absorbed	5%	8%	8%
Extinction Coefficient[8]	10.01	6.28	4.43
Optical Penetration Depth[9]	8.5 nm	6.7 nm	6.4 nm
Relative Efficiency[10]	1	2.04	1.67

6.4.1.2 Chromium

The surface quality of the chromium was poor and also difficult to improve. While this would have led to increased absorption, it made getting a return signal beam to the vibrometer difficult. The percentage of radiation absorbed is given in Table 6.7.

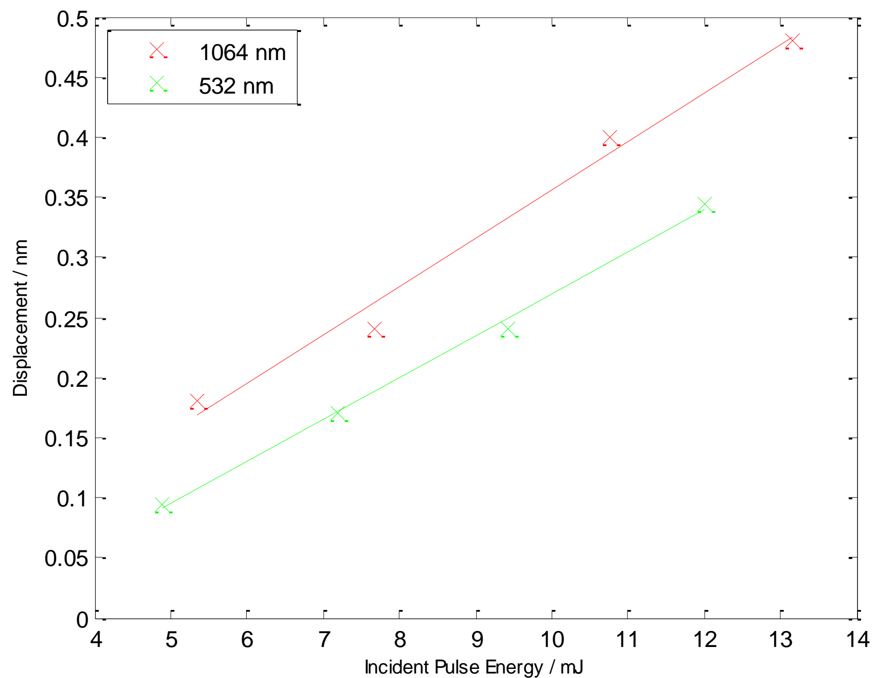

Figure 6.12: Peak to peak amplitude representation of acoustic waves generated in a chromium plate at two optical wavelengths and varying pulse energies.

[8] Taken from [6].
[9] Calculated from data in [6].
[10] Calculation performed on incident energy values.

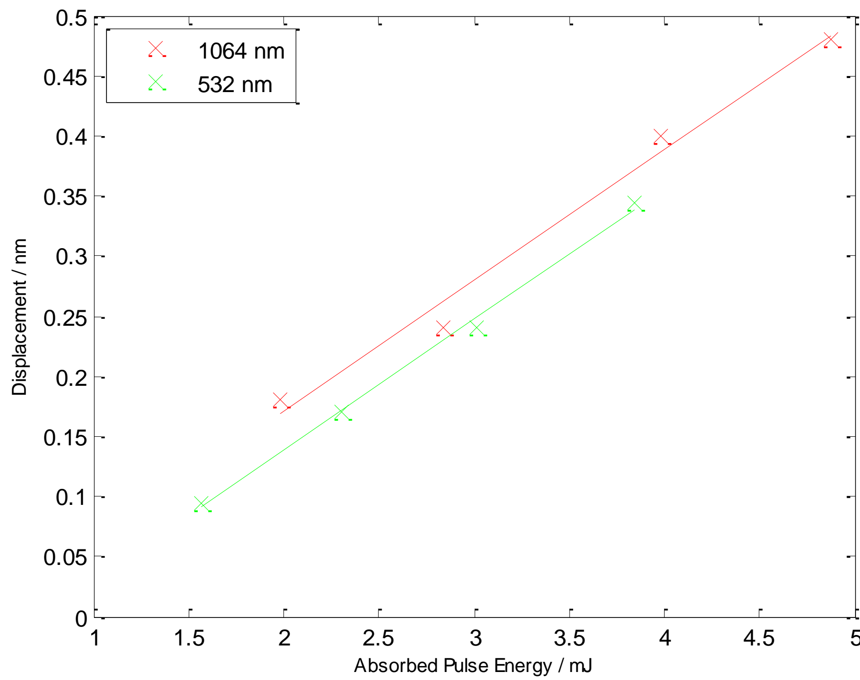

Figure 6.13: Generated acoustic wave amplitudes in Chromium, compensated for optical reflectivity.

Table 6.7: Percentage of absorbed energy into chromium.

	1064 nm	532 nm	355 nm
Chromium	37%	32%	35%

Table 6.8: Characterisation of acoustic waves as a function of wavelength in chromium.

Wavelength	**1064 nm**	**532 nm**	**355 nm**
% Energy Absorbed	37%	32%	*35%*
Extinction Coefficient	4.31	4.46	*3.24*
Optical Penetration Depth	19.6 nm	9.5 nm	8.7 nm
Efficiency	1	0.87	0.83*

Like aluminium, chromium has a silvery appearance and as illustrated by its reflectivity curve (Figure 6.14), there are relatively large changes in absorbed power. The data used to produce Figure 6.14 is taken from [6] (ref [8]).

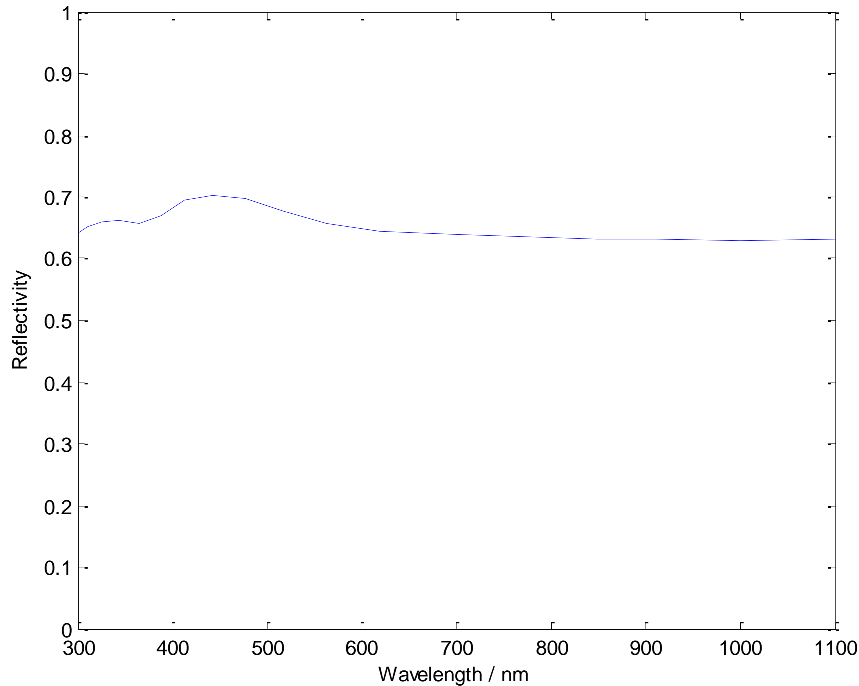

Figure 6.14: Reflectivity of chromium in vacuum.

Referring to Table 6.8, the optical penetration depth at 1064 nm is larger than at 532 nm and 355 nm and although the amount of absorbed energy is much greater than aluminium, it is evident from the results in Figure 6.12 and Figure 6.13 that 1064 nm is more efficient at generating acoustic waves, but again the difference between the two wavelengths is minimal. From the information shown in Table 6.8, (355 nm results given in italics), it is reasonable to estimate that the acoustic waves generated by 355 nm light would be of a lower efficiency than both 1064 nm light and 532 nm light. A number has been assigned to the efficiency section of Table 6.8 (marked with *). This fits with the reduction in extinction coefficient and optical penetration depth.

6.4.1.3 Copper

Optical absorption in metals such as aluminium and chromium is straight forward to explain in terms of the optical constants in the wavelength range considered here. However, unlike aluminium and chromium, copper has a distinct colour (reddish in appearance), indicating high reflectivity in the upper part of the visible spectrum as illustrated in Figure 6.15. The data used to produce Figure 6.15, Figure 6.18 and Figure 6.19 is taken from [6] (ref [9]).

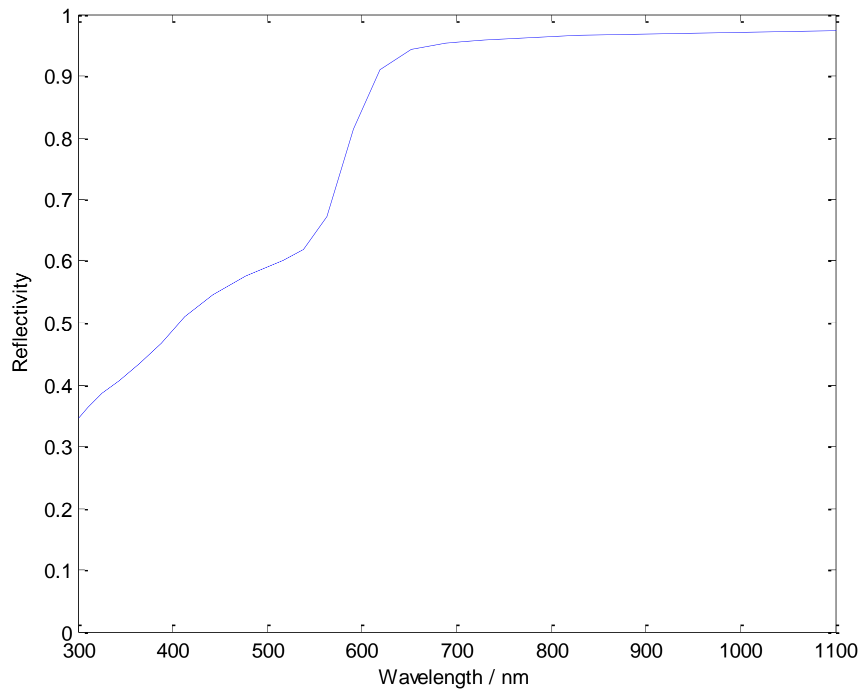

Figure 6.15: Reflectivity of copper in vacuum.

The percentage of radiation absorbed is given in Table 6.9

Table 6.9: Percentage of absorbed energy into copper.

	1064 nm	532 nm	355 nm
Copper	3%	38%	57%

Figure 6.16 shows the measured acoustic wave amplitudes as a function of wavelength and Figure 6.17 shows the corrected amplitudes. Once again, the results are as expected based on optical penetration depth and reflectivity, given in Table 6.10. It is interesting to note that if generation efficiency of acoustic waves in terms of just reflectivity is assumed, we would very quickly arrive at the wrong conclusion in the case of copper, due to intraband transitions discussed next.

Table 6.10: Characterisation of acoustic waves as a function of wavelength in copper.

Wavelength	1064 nm	532 nm	355 nm
% Energy Absorbed	3%	38%	57%
Extinction Coefficient	8.48	2.59	1.95
Optical Penetration Depth	9.9 nm	16.3 nm	14.5 nm
Efficiency	1	14.29	10

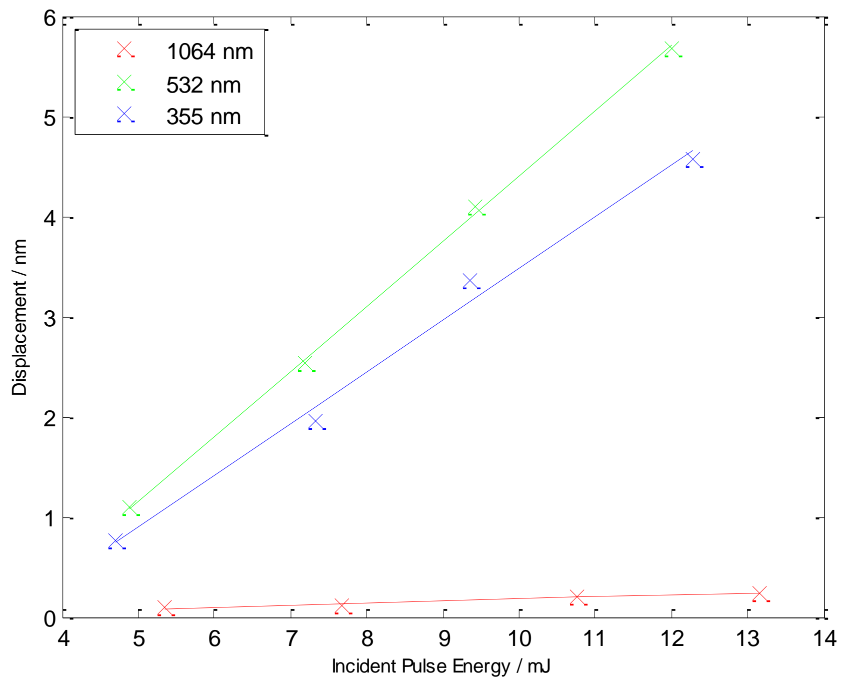

Figure 6.16: Peak to peak amplitude representation of acoustic waves generated in a copper plate at three optical wavelengths and varying pulse energies.

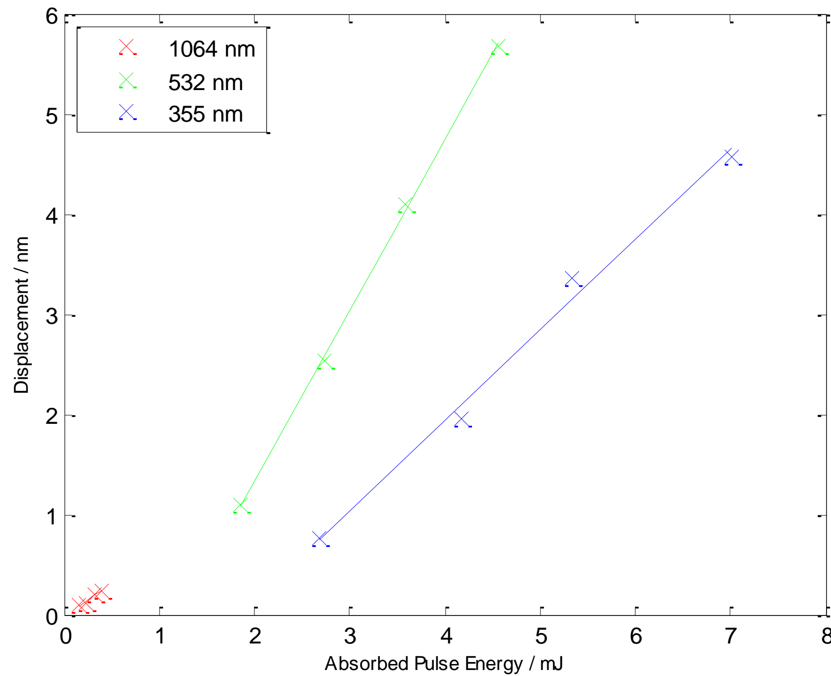

Figure 6.17: Generated acoustic wave amplitudes in copper, compensated for optical reflectivity.

Intraband absorption (free carriers) is adequate to explain absorption and hence generation efficiency of acoustic waves in aluminium. To explain why green or UV light is considerably more efficient than IR light at generating acoustic waves in copper, interband absorption must also be considered. This is where light is absorbed by an electron in an occupied state below the Fermi level, resulting in a transition to an unoccupied state in a higher band [10]. The Fermi level in copper is quoted in the literature to be approximately 2.1 eV (corresponding to a wavelength of 590.4 nm) [11, 12]. This point corresponds to an electron transition between specific energy states. As a side note, the interband transition threshold in chromium is at 0.8 eV (corresponding to a wavelength of 1549.8 nm) [13]. This can explain why the reflectivity of chromium is lower than aluminium and has not been mentioned until now as interband transition in chromium is beyond the wavelength of interest in this thesis.

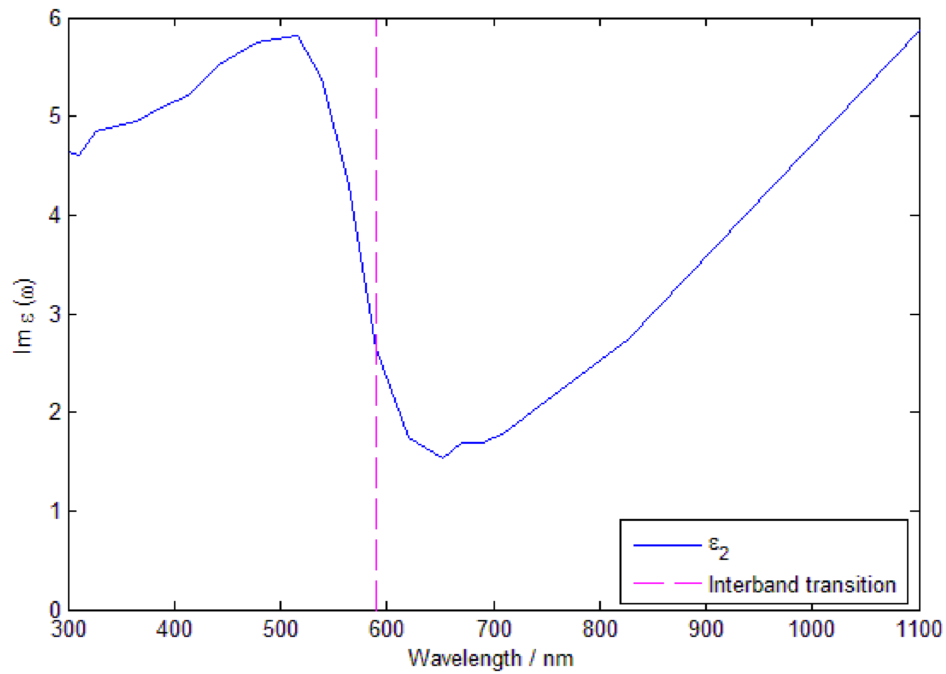

Figure 6.18: Imaginary part of the dielectric constant for copper.

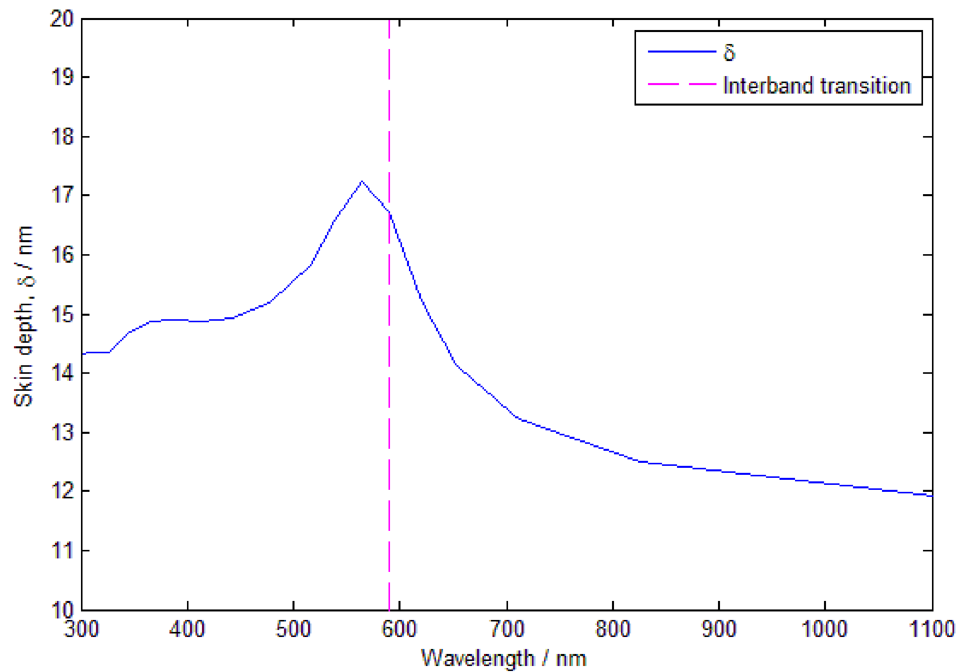

Figure 6.19: Optical penetration depth of radiation in copper as a function of wavelength.

In copper, the onset of interband absorption can be identified by a sharp rise in the imaginary part of the dielectric constant (ε_2) as illustrated in Figure 6.18. Since ε_2 is

dependent on both n and k, the rise at the interband transition threshold will decrease the reflectivity at this point. The extinction coefficient approaches a minimum, resulting in an increased skin depth as evident in Figure 6.19.

6.4.2 Acoustic wave generation in the silicon

Silicon was also studied to investigate the wavelength dependence on laser generated ultrasound. The details of the material are given in Table 6.1. The data used in this section was obtained from [14, 15]. This reference refers to intrinsic silicon and while the samples studied in this work are not guaranteed to be pure, the supplier quoted a purity of 99.999%. The reflectivity of silicon is shown in Figure 6.20, however, in the case of silicon, the situation is more complicated at our wavelength of interest.

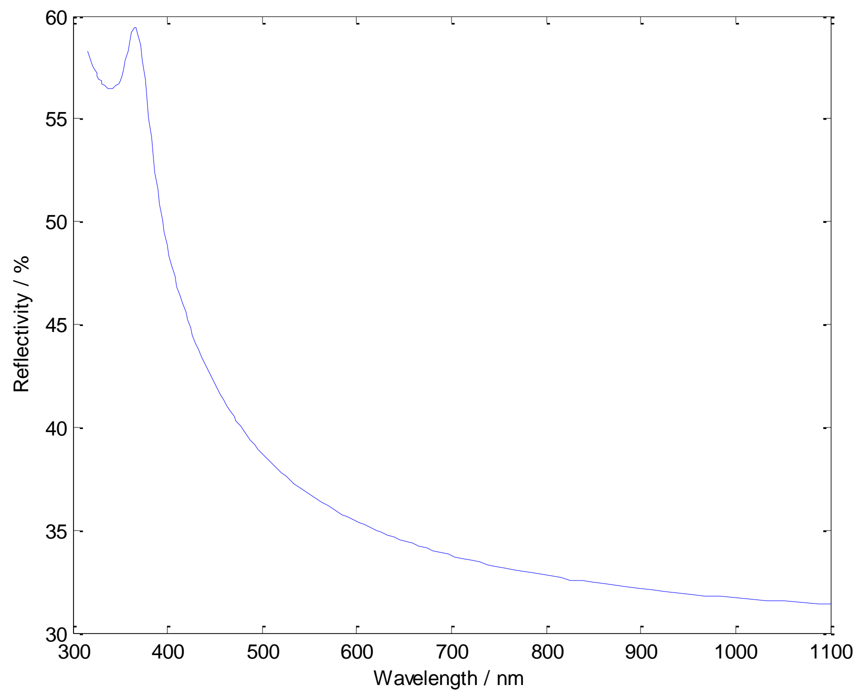

Figure 6.20: Reflectivity of silicon in vacuum.

The efficiency of acoustic wave generation is illustrated in Figure 6.21 and the reflectivity corrected values are shown in Figure 6.22.

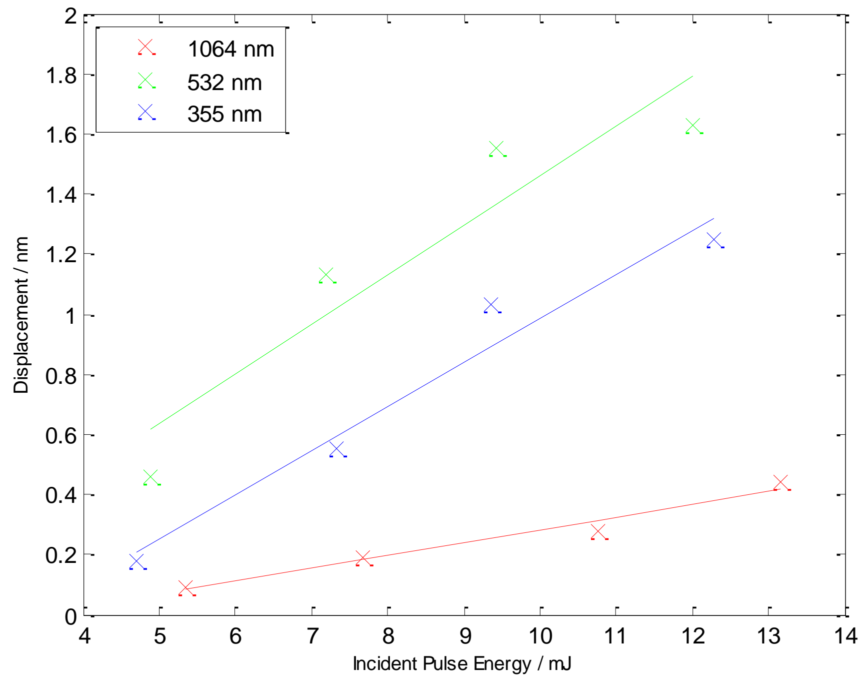

Figure 6.21: Peak to peak amplitude representation of acoustic waves generated in a silicon wafer at three optical wavelengths and varying pulse energies.

The band gap (or interband transition) for silicon is generally accepted to be 1.12 eV (or occurring at 1107 nm) at 300 K [16] and is the energy difference between the valance band and conduction band. At this point, silicon starts to become transparent to electromagnetic radiation. Of the light entering the sample, some will be reflected, some absorbed and some transmitted. This is illustrated in Figure 6.23. While reflectivity shows the amount of light reflected from the surface of a material, reflectance (and hence absorption and transmission are a function of material thickness. In Figure 6.23, the thickness was taken to be 381 μm. From this, it is clear that light of energy approximately equal to the bandgap energy penetrates much deeper into the material and at the thickness of a standard silicon wafer, some is transmitted through it. Reflectance is also increased, but the amount of energy absorbed greatly decreases.

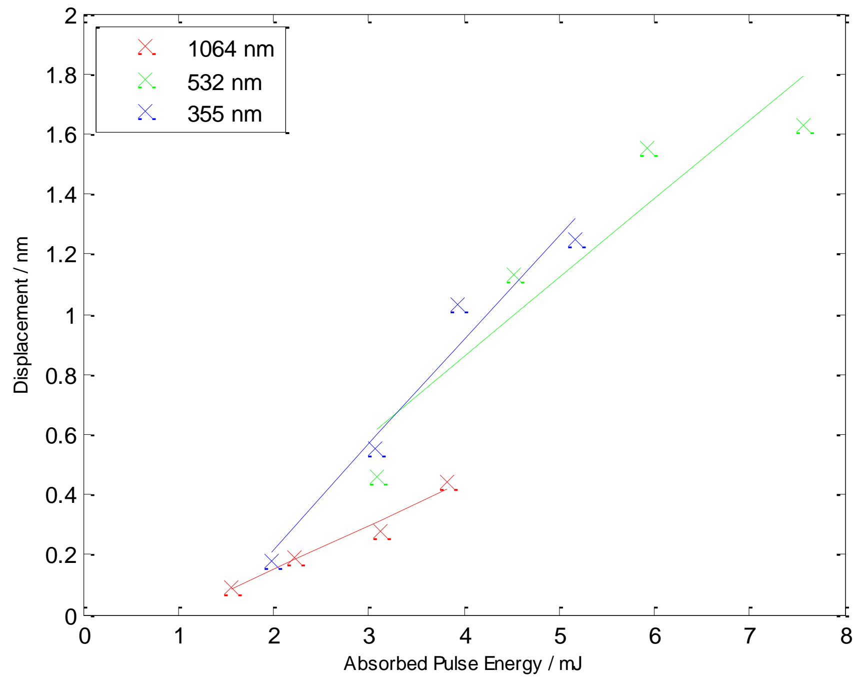

Figure 6.22: Generated acoustic wave amplitudes in silicon, compensated for optical absorption.

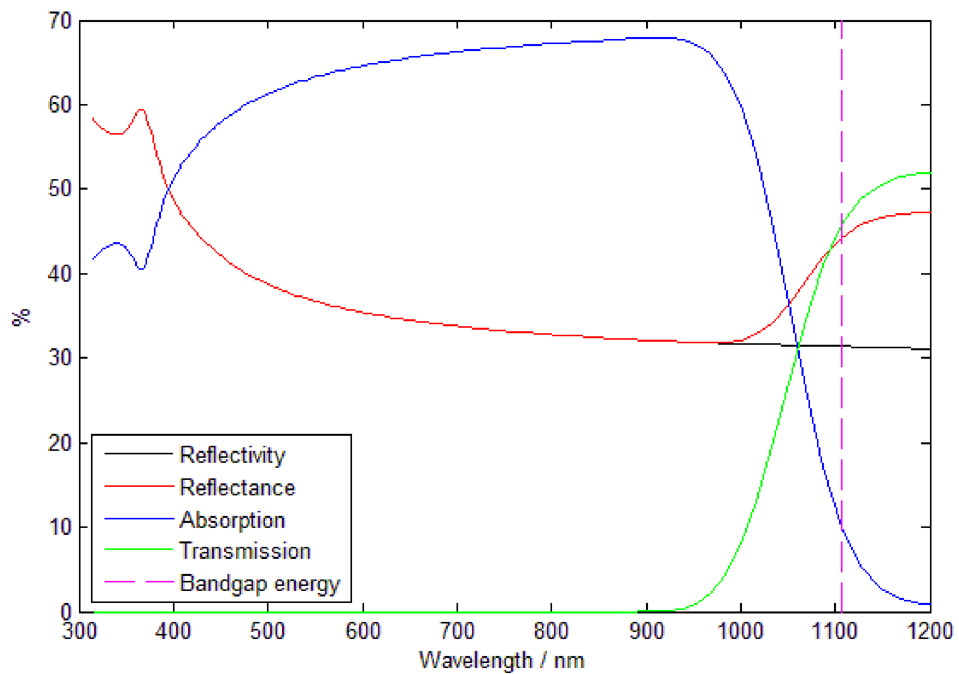

Figure 6.23: Reflectivity, reflectance, absorption and transmission on silicon in vacuum.

There is still some absorption, so there is still the generation of acoustic waves and as expected, the amplitudes of these waves are much smaller compared to those at 532 nm and 355 nm.

Considering the skin depth (Figure 6.24) it can be seen that the penetration depth at 532 nm is nearly 1500 nm, however this rises to over 1 mm at 1064 nm, which is just below the band edge.

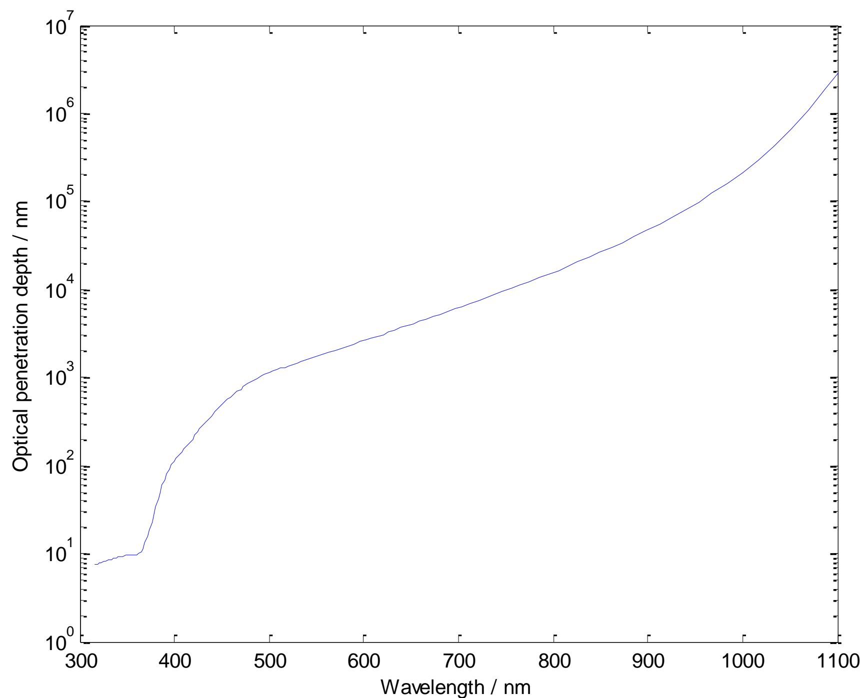

Figure 6.24: Optical penetration depth of silicon.

Normally it would be expected that 1064 nm would be more efficient at generating ultrasound due to the energy being absorbed into a larger volume and distributed over a larger depth *i.e.* a “buried source” but this would only apply to samples over 2 mm thick.

Table 6.11 shows the calculated efficiency of the acoustic waves in silicon. The absorbed energy at 1064 nm (marked with **) is calculated taking into account transmission of energy as well as reflectance.

Table 6.11: Characterisation of acoustic waves as a function of wavelength in silicon.

Wavelength	1064 nm	532 nm	355 nm
% Energy Absorbed	29%**	63%	42%
Extinction Coefficient	0.00008	0.02828	2.9636
Optical Penetration Depth	1.06×10^6 nm	1497 nm	10 nm
Efficiency	1	3.85	3.45

A sharp increase is observed in the extinction coefficient from the near IR to the visible region, resulting in a sharp decrease in the optical penetration depth. Comparing the penetration depths of the 532 nm light and 355 nm light to the generation efficiency, considering more energy was distributed over a larger volume, the acoustic amplitudes produced by 355 nm light are slightly larger than expected.

6.4.3 Acoustic wave generation in the semiconductors with thin metallic films

Following the work done on metal plates and silicon, the materials used were a blank n-type silicon wafer and wafers with aluminium, copper and chromium films evaporated onto them as detailed in Table 6.2. Thin films generally have a lower density, thermal conductivity and refractive index than bulk materials. However for this analysis the optical properties used for the corresponding bulk materials will be used. The results are shown in Figure 6.25 to Figure 6.30 and Table 6.12.

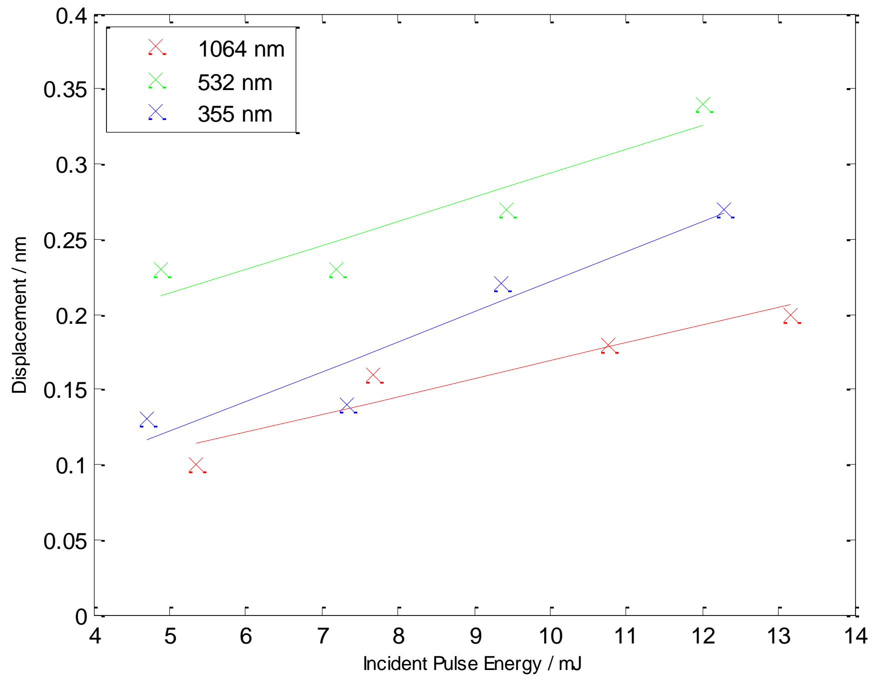

Figure 6.25: Peak to peak amplitude representation of acoustic waves generated in a silicon wafer with an aluminium film at three optical wavelengths and varying pulse energies.

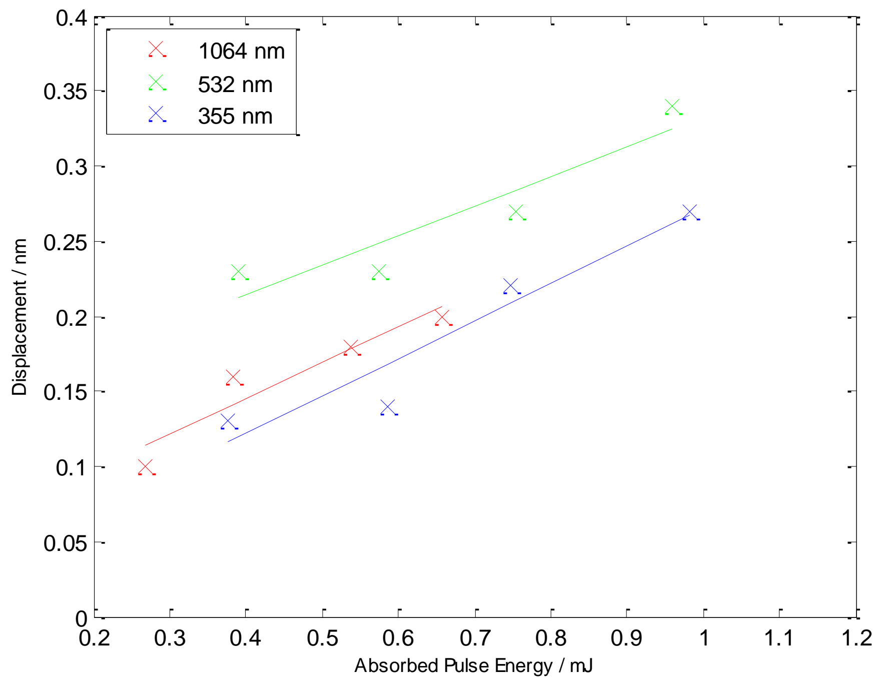

Figure 6.26: Generated acoustic wave amplitudes in silicon with an aluminium film, compensated for optical absorption.

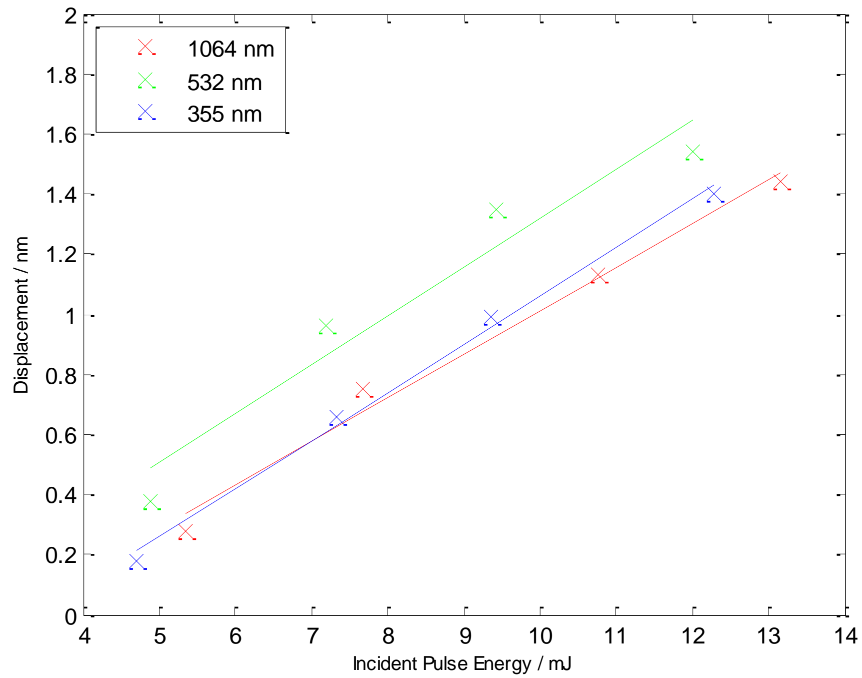

Figure 6.27: Peak to peak amplitude representation of acoustic waves generated in a silicon wafer with a chromium film at three optical wavelengths and varying pulse energies.

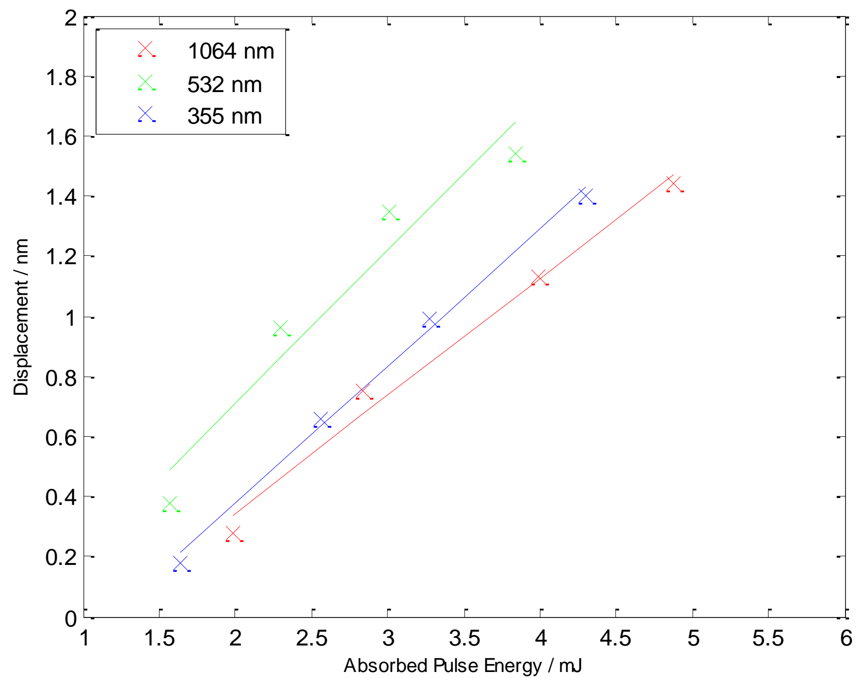

Figure 6.28: Generated acoustic wave amplitudes in silicon with a chromium film, compensated for optical absorption.

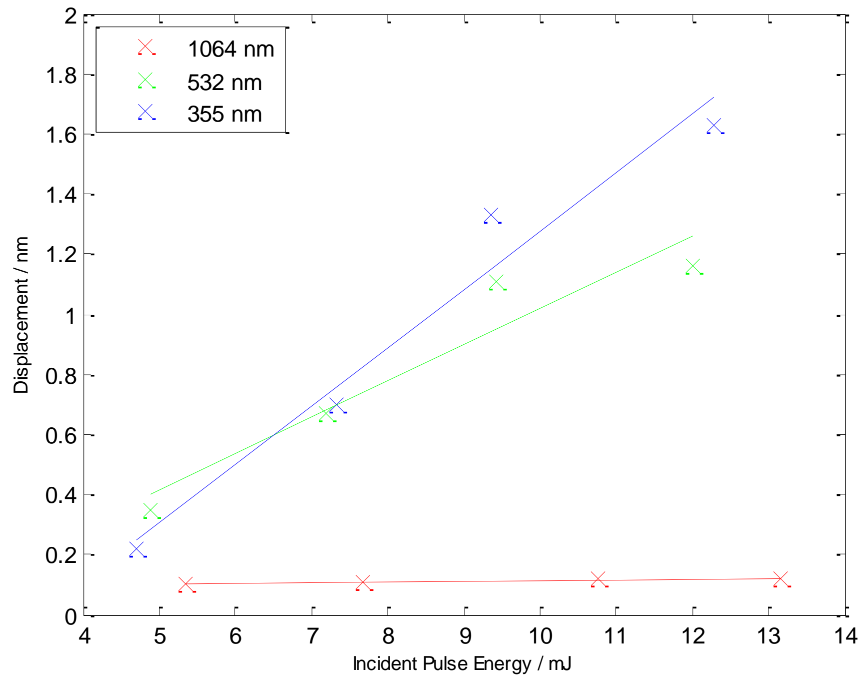

Figure 6.29: Peak to peak amplitude representation of acoustic waves generated in a silicon wafer with a copper film at three optical wavelengths and varying pulse energies.

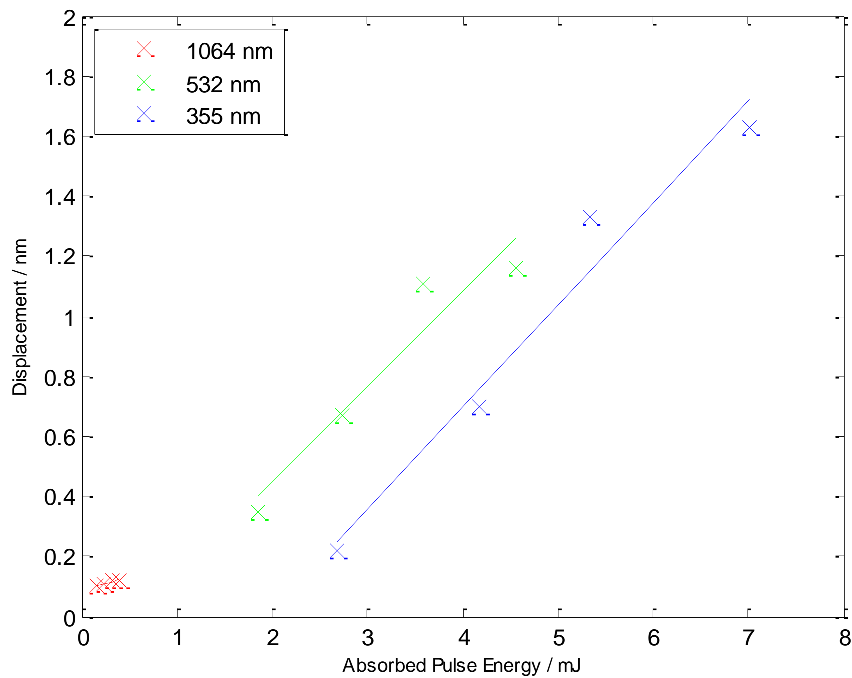

Figure 6.30: Generated acoustic wave amplitudes in silicon with a copper film, compensated for optical absorption.

Table 6.12: Characterisation of acoustic waves as a function of wavelength in silicon and silicon with various metallic thin films.

	Wavelength	1064 nm	532 nm	355 nm
Silicon wafer	% Energy Absorbed	29%	63%	42%
	Extinction Coefficient	0.00008	0.02828	2.9636
	Optical Penetration Depth	1.06×10^6 nm	1497 nm	10 nm
	Efficiency	1	3.85	3.45
Silicon wafer with aluminium film	% Energy Absorbed	5%	8%	8%
	Extinction Coefficient	10.01	6.28	4.43
	Optical Penetration Depth	8.5 nm	6.7 nm	6.4 nm
	Efficiency	1	1.33	1.67
Silicon wafer with chromium film	% Energy Absorbed	37%	32%	35%
	Extinction Coefficient	4.31	4.46	3.24
	Optical Penetration Depth	19.6 nm	9.5 nm	8.7 nm
	Efficiency	1	1.14	1.11
Silicon wafer with copper film	% Energy Absorbed	3%	38%	57%
	Extinction Coefficient	8.48	2.59	1.95
	Optical Penetration Depth	9.9 nm	16.3 nm	14.5 nm
	Efficiency	1	50	100

The light incident on each surface will not penetrate the thickness of the films so the source can be considered a disk as is the case with the metal plates. The heating effect (thermal diffusion length) will extend into the silicon wafer, in effect crossing the film/substrate boundary. This boundary condition, along with the knowledge of Lamb wave amplitudes measured can be compared to that of the silicon wafer with no film to give an indication of generation efficiency from the film to the substrate.

Considering Figure 6.31 to Figure 6.33, the most striking observation is that the efficiency of acoustic wave generation is very low across the wavelength range for aluminium films. The chart showing the results at 1064 nm also proves again that copper has low generation efficiency at this wavelength.

The rest of the results show that, depending on the film, acoustic wave generation efficiency can be enhanced, producing larger amplitudes with a thin film than without. Particularly, the chromium film radiated by 1064 nm and 355 nm radiation, and the copper film at 355 nm. It is well known that chromium develops a strong adhesive bond with silicon and silicon dioxide so this result is not surprising [17]. The other point to note is that the amplitude of the acoustic waves in silicon generated using light at 532 nm (Figure 6.32) is larger due to the fact that the source in this wavelength is more of a buried source.

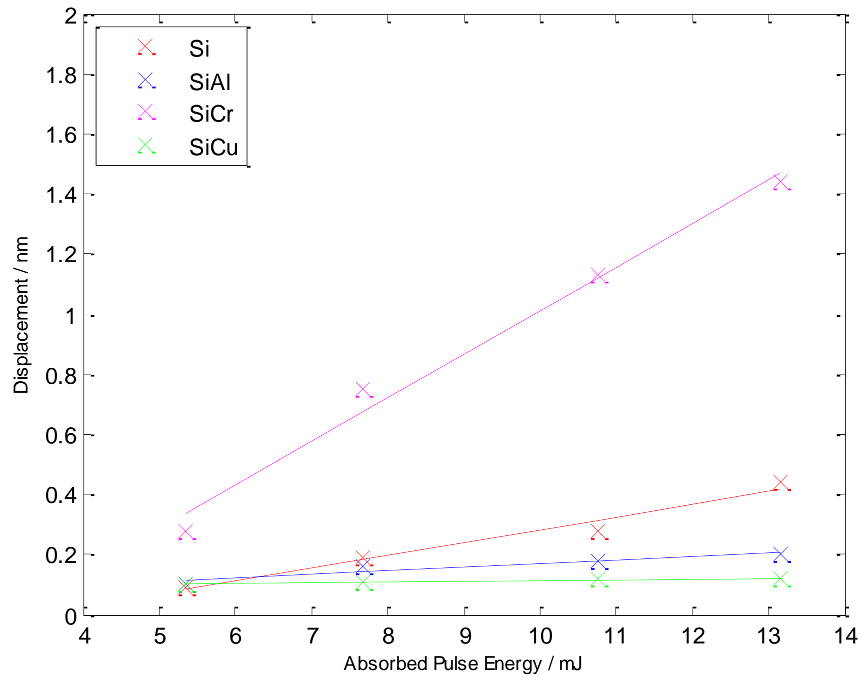

Figure 6.31: Comparison of acoustic generation efficiency, comparing the three thin films, Al, Cr and Cu on a silicon substrate to that of a blank silicon wafer at 1064 nm.

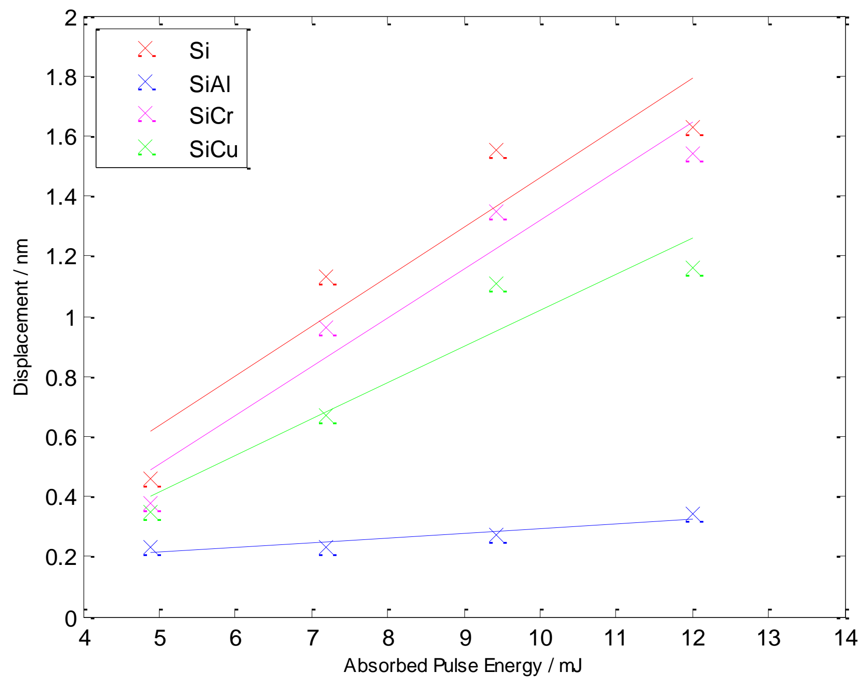

Figure 6.32: Comparison of acoustic generation efficiency, comparing the three thin films, Al, Cr and Cu on a silicon substrate to that of a blank silicon wafer at 532 nm.

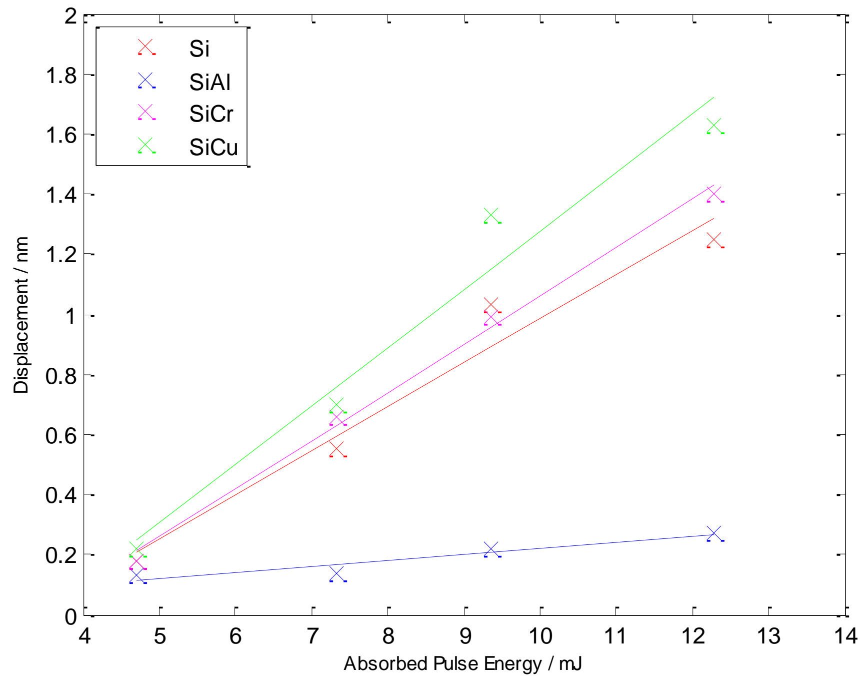

Figure 6.33: Comparison of acoustic generation efficiency, comparing the three thin films, Al, Cr and Cu on a silicon substrate to that of a blank silicon wafer at 355 nm.

To fully understand this observation the thermal boundary resistance across the metal – silicon interface must be included. When light is absorbed, heat is generated and carried through the boundary at the interface. The heat transfer across this boundary will impact the amplitude of the acoustic waves generated. There are three effects which will reduce the transfer of heat across the interface: interface scattering, grain boundary scattering and interface roughness [18]. The heat carriers in metals are mainly electrons, and each of the three effects listed above will act to reduce the transfer of heat across the interface. In addition, the thermal conductivity decreases as the lateral dimension decreases, often referred to as the size effect [19]. This can cause the values of thermal conductivity to drop by ≈20% or less for thin films compared to the bulk material values. At the micro level, thermal conductivity is related to material structure, *i.e.* grain size. With a large reduction in thermal conductivity of aluminium in film form, the reduced amplitude values shown are reasonable, compared to that of a blank silicon wafer. Likewise, the results for

chromium are reasonable, due the excellent bonding with the silicon substrate and while there will be a reduction in thermal conductivity, there will also be a reduction in the loss of energy from interface scattering.

6.5 Photostriction as a method of generating acoustic waves in silicon

All the work in this thesis up to this point, and indeed from the next chapter onwards has dealt with incident radiation being absorbed by a material, resulting in a localised heating, causing a thermal expansion and subsequent thermal stress resulting in the propagation of an elastic wave. This however is not the only way to generate elastic waves using light.

An alternative method is to use the photostrictive effect. This was first demonstrated by Figielski [20] using germanium sample and was later repeated by Gauster and Habing [21] for silicon samples.

Like the description of optical absorption above, light is absorbed into a semiconducting material, in this case, silicon and penetrates to a depth dictated by the absorption coefficient. In metals, this leads to a thermal expansion, but in silicon, the light also generates free charge carriers (electron-hole pairs), producing a local mechanical strain. The mechanical strain is a result of a contraction in silicon (expansion in germanium) up to a depth equal to the skin depth. The contraction is caused by an increase in electron concentration which also increases the pressure of the electron gas. The volume changes to minimise the energy. The pressure dependence of the bandgap, given by $\frac{d\varepsilon_g}{dP}$ is negative in silicon and so the effect is much easier to observe. Charge carriers also form much faster than the thermal stresses so the contraction will appear much sooner than the thermal expansion stress wave. Light incident on the silicon surface must meet the condition $\lambda < \lambda_{\epsilon_g}$ where λ_{ϵ_g}corresponds to the wavelength of the bandgap energy.

To illustrate this effect, a simple experiment was set up. Using the silicon wafer with an aluminium thin film, mounted vertically, light at 532 nm and peak power 200 kW was incident on the surface of the wafer. The detection beam was incident on the opposite side of the wafer, in effect detecting the bulk wave through the material. The experiment was performed twice. The first experiment had the excitation beam on the aluminium film and the second one had the excitation beam on the silicon surface. The result is shown in Figure 6.34. Note the offset is for presentation purposes only. Some very obvious features can be extracted from this plot. The first is the onset of the thermally induced stress wave in the aluminium/silicon sample at 0.22 μs. This stress wave can also be seen in the silicon sample at the same time, however, there is also some other structure present. This other structure is the expansion caused in response to the contraction visible from 0.13 μs to 0.24 μs.

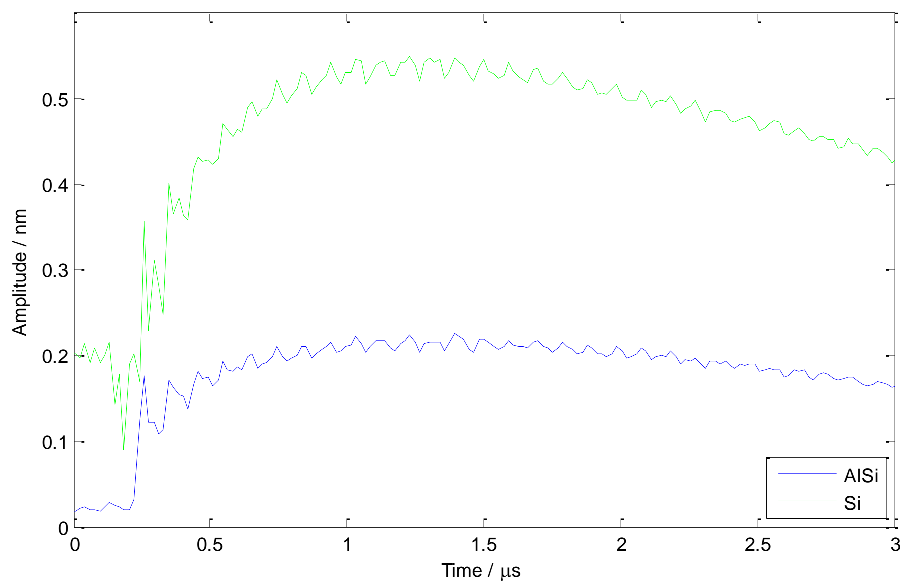

Figure 6.34: Acoustic bulk waves generated in silicon and silicon with an aluminium thin film.

From Figure 6.34, a contraction of 0.11 nm in the uncoated silicon (green line) is visible at 0.19 μs. No thermal stress contributes to this, concluding that this is purely an electronic effect and so using a modified version of the expression in [22], a value for Poisson's ratio can be obtained.

$$x_3 = \frac{(1-\nu)l^2}{\delta}\frac{d\varepsilon_g}{dP}\Delta n \quad \textbf{6.9}$$

For this equation, x_3 is the value of the contraction (0.11 nm), l is the length of the source (100 μm), δ is the skin depth (≈1500 nm), $\frac{d\varepsilon_g}{dP}$ is the pressure dependence of the bandgap (-2.9×10^{-24} cm^3, given in [22]) and Δn is the excess charge carriers ($\approx 8.7 \times 10^9$). From this, a value of 0.27 is obtained for Poisson's ratio.

6.6 Conclusions.

In other works [1], authors have stated that the efficiency of optically generated acoustic waves is related to the extinction coefficient. It has been demonstrated here that although this is partly the case, the optical penetration depth must also be taken into account. The extinction coefficient is a function of optical wavelength, but the optical penetration depth is a function of extinction coefficient and optical wavelength. It has also been observed, both in this work and by others [1] that the fitted trendlines do not go through the origin. This can mainly be attributed to systematic errors. However, in the case of the copper samples, intraband transitions may have an effect. Based on the materials studied in this work, the optimum conclusion to draw is that light at 532 nm is best for acoustic wave generation. Due to the high reflectivity in metals in the near IR and the onset of transmission in silicon, 1064 nm light can easily be ruled out. In most cases there is little difference between light at 532 nm and light at 355 nm, however, safety must always be taken into consideration with any experimental work and for this reason light at 532 nm is the better wavelength to use.

One major disadvantage in presenting the results in this chapter was the reliance on optical property values obtained from the literature, such as the refractive index or extinction coefficient. It was not considered at the time of the measurements but a more reliable and sample specific picture could have been drawn had measurements of refractive index and extinction coefficient been obtained. This applies to all materials studied. It would also have been interesting to compare optical properties

of corresponding bulk and thin film materials. Although a surface profiler was used to obtain values of film thickness, it would also have been interesting to obtain SEM images of a cross section of each thin film. Not only would this have given information on the thickness of the film, but also on the formation of it. Details of thin film formation and/or grain size may possibly have helped to explain the effects of elastic wave generation in the thin film on silicon samples.

In addition, with a very small modification to the experimental set up, it has been shown that light can be used to generate an elastic response due to the photostrictive effect. It has also been demonstrated how this could be used to obtain Poisson's ratio, a fundamental material property of interest to the engineering community. With the continued development of MEMS structures and their characterisation, this could, along with thermally generated ultrasound, become a viable tool for measuring Poisson's ratio.

6.7 References.

[1] C. M. Flannery, P. V. Kelly, J. T. Beechinor and G. M. Crean, "Obervation of wavelength dependent generation efficiency of laser induced ultrasonic surface acoustic waves on ceramic materials," *Appl. Phys. Lett.,* vol. 71, no. 26, pp. 3767-3769, 1997.

[2] N. Maluf and K. Williams, An Introduction to Microelectromechanical Systems engineering, 2nd ed., Artech House, 2004.

[3] "Goodfellow," [Online]. Available: http://www.goodfellow.com/.

[4] I. Arias and J. D. Achenbach, "Thermoelastic generation of ultrasound by line-focused laser irradiation," *International Journal of Solids and Structures.,* vol. 40, no. 25, pp. 6917-6935, 2003.

[5] P. Romaniello, P. L. de Boeij, F. Carbone and D. van der Marel, "Optical properties of bcc transtion metals on the range 0 - 40 eV," *Phys. Rev. B,* vol. 73, p. 075115, 2006.

[6] D. R. Lide, Ed., CRC Handbook of Chemistry and Physics, CRC Press, 2005.

[7] E. Shiles, T. Sasaki, M. Inokuti and D. Smith, “Self-consistency and sum-rule tests in the Kramers-Kronig analysis of optical data: Applications to aluminum,” *Phys. Rev. B.,* vol. 22, pp. 1612-1628, 1980.

[8] L. W. Bos and D. W. Lynch, “Optical properties of antiferromagnetic chromium and dilute Cr-Mn and Cr-Re alloys,” *Phys. Rev. B,* vol. 2, pp. 4567-4577, 1970.

[9] H. J. Hagemann, W. Gudat and C. Kunz, “Optical constants from the far infrared to the x-ray region: Mg, Al, Cu, Ag, Au, Bi, C, and A12O3,” *J. Opt. Soc. Am.,* vol. 65, no. 6, pp. 742-744, 1975.

[10] M. S. Dresselhaus, MIT, [Online]. Available: http://web.mit.edu/course/6/6.732/www/6.732-pt2.pdf.

[11] S. Roberts, “Optical properties of copper,” *Phys. Rev.,* vol. 118, no. 6, pp. 1509-1518, 1960.

[12] H. Ehrenreich and H. R. Phillipp, “Optical Properties of Ag and Cu,” *Phys. Rev.,* vol. 128, no. 4, pp. 1622-1629, 1962.

[13] P. E. Hopkins, J. C. Duda, R. N. Salaway, J. L. Smoyer and P. M. Norris, “Effects of intra- and interband transitions on electron-phonon and electron heat capacity after short pulse laser heating,” *Nanoscale and MicroscaleThermophysical Engineering,* vol. 12, pp. 320-333, 2008.

[14] M. H. Jones and S. H. Jones, Virginia Semiconductor Inc., [Online]. Available: https://www.virginiasemi.com/.

[15] D. E. Aspnes, “Optical Properties,” in *Properties of Crystalline Silicon*, R. Hull, Ed., Inspec, 1998.

[16] S. M. Sze, Physics of Semiconductor Devices, 2nd ed., John Wiley & Sons, 1981, p. 849.

[17] P. E. Hopkins, P. M. Norris, R. J. Stevens, T. E. Beechem and S. Graham, “Influence of interfacial mixing on thermal boundary conductance aross a chromium/silicon interface,” *J. Heat Transfer,* vol. 130, p. 062402, 2008.

[18] X. Lu, "Thermal conductivity modelling of copper and tungsten damascene structures," *J. Appl. Phys.,* vol. 105, p. 094301, 2009.

[19] B. Feng, Z. Li and X. Zhang, "Prediction of size effect on thermal conductivity of nanoscale metallic films," *Thin Solid Films,* vol. 517, pp. 2803-2807, 2009.

[20] T. Figielski, "Photostriction effect in Germanium," *Physica Status Solidi (B),* vol. 1, no. 4, pp. 306-316, 1961.

[21] W. B. Gauster and D. H. Habing, "Electronic volume effect in Silicon," *Phys. Rev. Lett.,* vol. 18, pp. 1058-1061, 1967.

[22] P. G. Datskos, S. Rajic and I. Datskou, "Photoinduced and thermal stress in silicon microcantilevers," *Appl. Phys. Lett.,* vol. 73, no. 16, pp. 2319-2321, 1998.

7 Characterisation of the MEMS Pressure Sensor

7.1 Introduction

One commonly used method for obtaining Lamb wave dispersion curves from plates is by using the method proposed by Alleyne and Cawley [1]. When excited by a broadband source, more than one propagating mode is generated. These propagating modes are considered sinusoidal in nature and the method proposed in [1] takes the two dimensional Fourier transform of the time domain Lamb waves. First, a Fourier transform is applied to the time domain to give frequency, followed by a Fourier transform to the spatial domain, giving wavenumber. Multiple signals are captured, each at an equal distance from the previous and the wavenumber bandwidth is set by the distance between each successive measurement, while the resolution is set by the total distance measurements are taken over. This signal processing method requires 100s of measurements, taken at equally spaced distances and it is clear that this is really only applicable to large structures. It is possible to use this technique for structures of the scale of the MEMS pressure sensor, using piezo nano-positioning equipment such as that provided by Attocube [2], for example However, this adds another level of complexity and expense to the experimental set up. A much simpler solution would be to use a signal processing technique that only requires one measurement. Using a single measurement to characterise the MEMS pressure sensor is the focus of this chapter.

7.2 Time–frequency analysis of Lamb Waves.

While investigating signal analysis, when applied to communications, Dennis Gabor [3] stated that signals can be displayed as a function of time or a function of frequency. He goes on to say that signals can be presented in two dimensions, with time and frequency acting as coordinates. In other words, they map a one dimensional time domain signal into a two dimensional time and frequency signal

which represents the variation of spectral energy over time [4]. This area of signal processing collectively became known as time-frequency analysis with the output of the analysis known as time-frequency representations (TFR). The techniques can be applied to any non-stationary signal, *i.e.* one that changes as a function of time, so there is an endless list of systems that could be analysed in this way. Multimode Lamb waves are one of many systems that are suitable for time-frequency analysis. Time-frequency representations operate on time domain signals and are able to resolve individual Lamb modes, leading to a group velocity representation [5].

7.3 Short Time Fourier Transform.

The time domain of a signal gives information on the how the signal evolves with time and the frequency domain shows the spectral content of a signal. However, what happens if one wants to see how the spectral content of the signal evolves over time? This is what can be achieved with time-frequency analysis and the first method to show this was the short time Fourier transform (STFT) [6]. The STFT contains a windowing function that, when applied to a signal, breaks the signal into segments, where a Fourier transform is performed. This is illustrated in Figure 7.1 [7] and is mathematically defined as

$$STFT(x;\omega,t) = \int_{-\infty}^{\infty} x(\tau)\, h(\tau - t) e^{-i2\pi\omega\tau}\, d\tau \qquad \textbf{7.1}$$

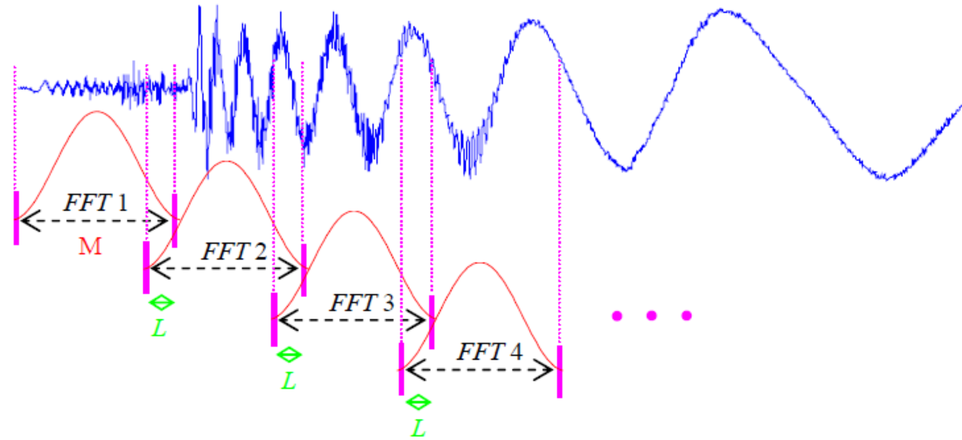

Figure 7.1: Time frequency analysis splits the time domain waveform into overlapped windowed sections before performing an FFT on them [7].

The window, $h(\tau\text{-}t)$ suppresses the signal around the analysis time point $\tau=t$ and the STFT gives a local spectrum of the signal $x(\tau)$ around t. the output of the STFT is the spectrogram and is the energy density spectrum of the STFT. This is given as [8]

$$E(\omega, t) \propto |S(\omega, t)|^2 \qquad \textbf{7.2}$$

The short time Fourier transform, like all time-frequency representations suffer from what is [incorrectly] referred to as the Heisenberg uncertainty principle. A more appropriate name would be the Heisenberg-Gabor uncertainty principle. This states that it is impossible to simultaneously get good resolution in time and frequency at the same time. The resolutions in time and frequency are related and limited by the inequality

$$\sigma_t^2 \sigma_\omega^2 \geq \frac{1}{4} \qquad \textbf{7.3}$$

Where σ_t is the standard deviation for time and σ_ω is the standard deviation for frequency. The resolution in time and frequency of the spectrogram is dictated completely by the window size and type used. A narrow window will give good time resolution and poor frequency resolution while a wide window gives good frequency

resolution and poor time resolution. This applies to a Gaussian window such as $h(\tau\text{-}t)$ given above in equation 7.3. Different windows have slightly different inequalities, such as the Hanning window, which has the inequality [8]

$$\sigma_t^2\sigma_\omega^2 = 0.2635 \quad (7.4)$$

To demonstrate this, let us consider an example. The waveform shown in Figure 7.2 was measured with a source detector separation distance of 5 mm and averaged 4096 times. The acoustic wave generation source and detector arrangement will be described later in section 7.5. Finally, the wafer thickness was quoted by the supplier [9] as 50 µm.

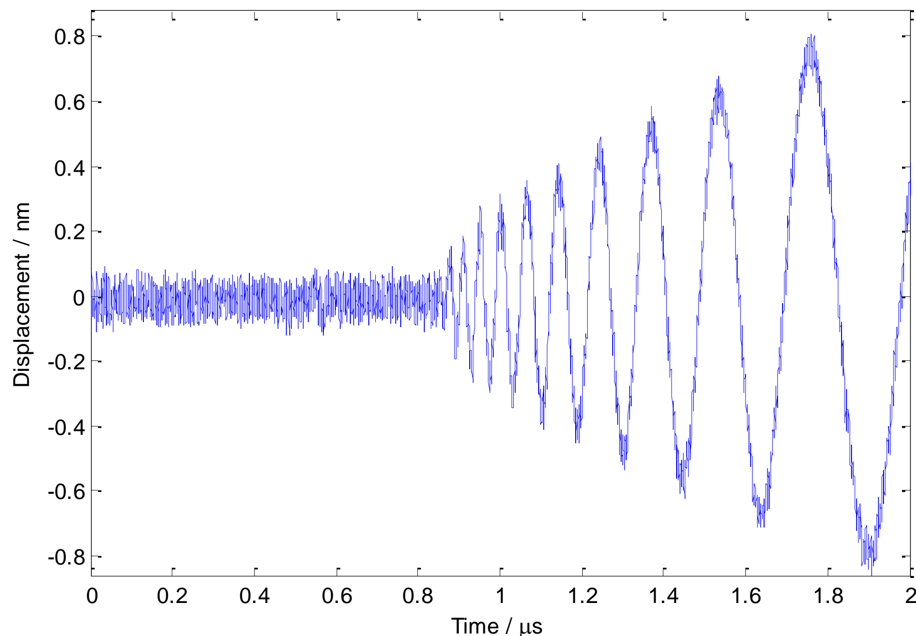

Figure 7.2: Lamb wave measured in 50 µm silicon wafer.

If the signal has a Chebyshev type II bandpass filter applied to it, between 5 MHz and 200 MHz, the waveform shown in Figure 7.3 is obtained. The file contained 8192 data points and to demonstrate the effect of window length, two windows will be chosen, one at each extreme. One will be 1% of the file length and one will be 99% of the file length. The results of this are shown in Figure 7.4 and Figure 7.5.

Figure 7.4 used the narrow time window, *i.e.* 1% of the file size and it is clearly evident that the time resolution is excellent where the low frequency part of the S_0 mode is visible along with the dominant A_0 mode. Figure 7.5 shows that with a wide time window, *i.e.* 99% of the file size, the frequency resolution is excellent. However, the information seems completely dominated by the A_0 mode and the information regarding the S_0 mode is lost in this. Applying a realistic window width, such as 385 points, to the same signal gives the result shown in Figure 7.6. The length of the window cannot be determined mathematically. Rather, it is through a process of trying to find the optimal frequency and time resolution suitable to the dataset being monitored. Figure 7.6 shows a more accurate representation of a time frequency plot for a dispersive multimode signal, with the A_0 and S_0 Lamb modes clearly visible. It is clear that the A_0 mode is non dispersive between approximately 1.2 μs and 2 μs and dispersive between 0.8 μs and 1.2 μs. The non dispersive component of the S_0 mode appears at approximately 0.6 μs. This does illustrate the problem of the STFT giving an output of limited resolution. This is addressed in the next section.

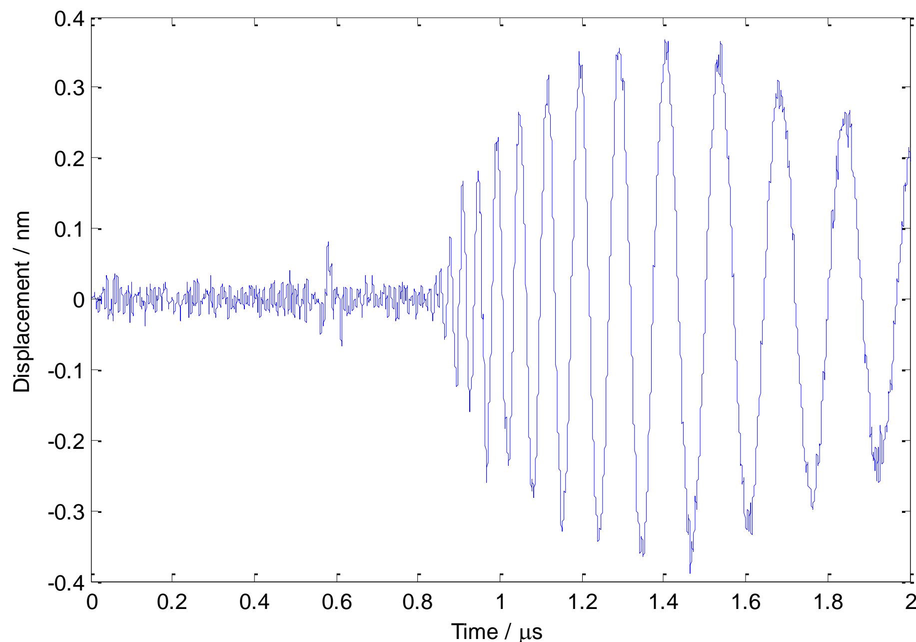

Figure 7.3: Bandpass filtered Lamb wave.

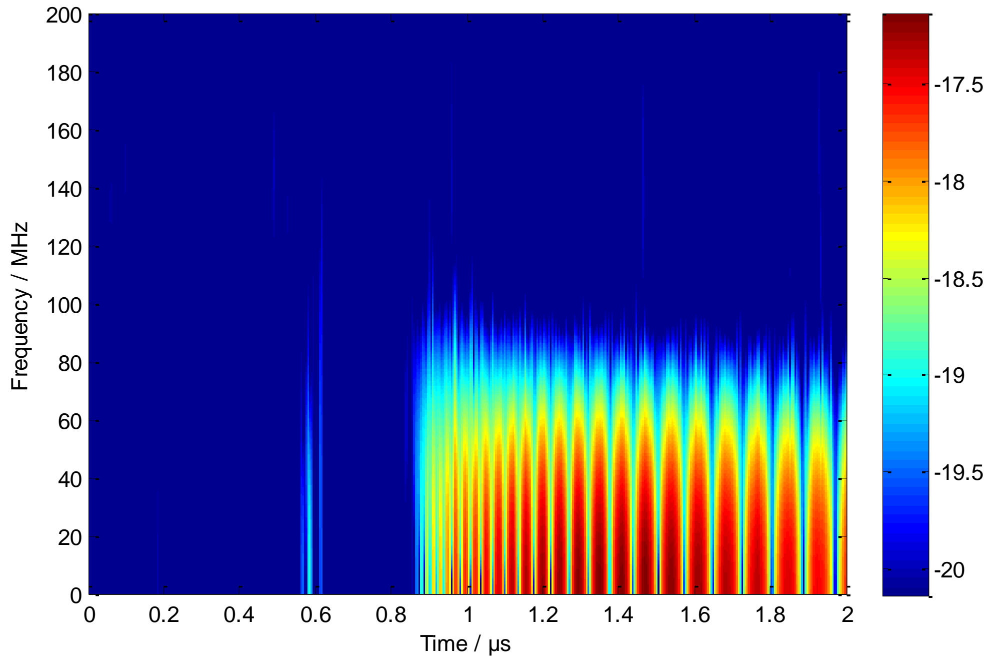

Figure 7.4: Spectrogram obtained using a narrow time window.

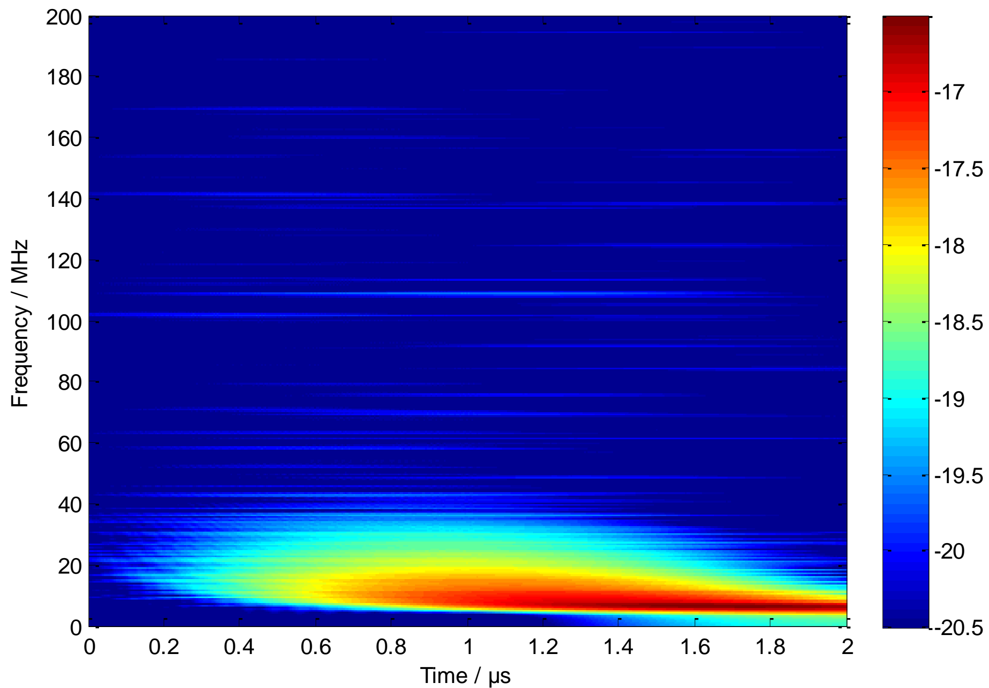

Figure 7.5: Spectrogram obtained using a wide time window.

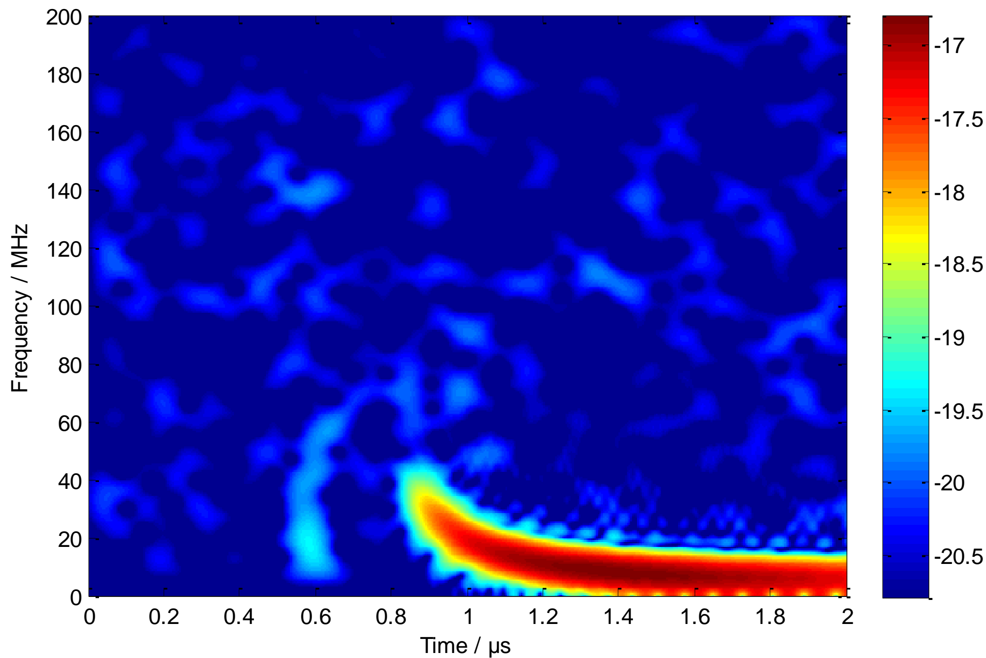

Figure 7.6: Realistic spectrogram of Lamb wave.

7.4 The Reassignment Method.

Section 7.3 showed how the spectrogram can be applied to a multimode Lamb wave to give information on the group velocity, but it is also evident from Figure 7.6 that the spectrogram resolution is limited. This is due to the trade-off between time and frequency resolution and while a window size can be chosen that gives the best compromise, what is produced is still a somewhat blurry image.

The reassignment method goes a step further and focuses the energy in the time-frequency data to a central point. To use a mechanical analogy, it can be considered as focusing the mass of an object to its geometric centre.

The reassignment method was first developed by Auger and Flandrin [10] and provides a method for "cleaning up" the spectrogram. In the reassignment method, energy of the signal is moved from its original location (t, ω) to a new location $(\hat{t}, \widehat{\omega})$ reducing the spread of the spectrogram and improving its resolution by

concentrating its energy at a "centre of gravity" [8]. It was shown in [8, 10] that the reassigned coordinates $\hat{t}$ and $\widehat{\omega}$ for a spectrogram are

$$\hat{t} = t - \Re\left(\frac{S_{\mathcal{T}h}(x,t,\omega).\overline{S_h(x,t,\omega)}}{|S_h(x,t,\omega)|^2}\right) \quad 7.5$$

and

$$\widehat{\omega} = \omega - \Im\left(\frac{S_{\mathcal{D}h}(x,t,\omega).\overline{S_h(x,t,\omega)}}{|S_h(x,t,\omega)|^2}\right) \quad 7.6$$

where $S_h(x,t,\omega)$ is the standard STFT of the signal *x* using window function *h(t)* and $S_{\mathcal{T}h}(x,t,\omega)$ is the STFT using a time ramped version of the window, $t \cdot h(t)$ and $S_{\mathcal{D}h}(x,t,\omega)$ is the STFT using the first derivative of the window function, $\frac{dh(t)}{dt}$ [11]. These are shown in Figure 7.7. it should be noted that *t=0* occurs at sample number 1000.

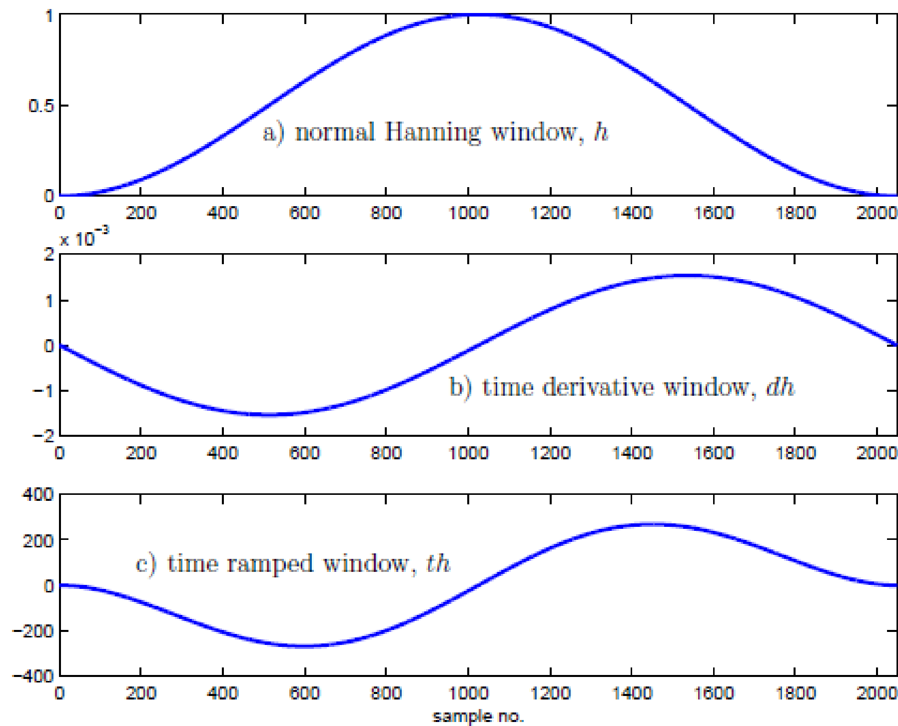

Figure 7.7: The three windows used for reassignment, (a) the normal Hanning window, (b), the time derivative window and (c) the time ramped window [11].

The reassignment method can be considered a two step process:

- Smoothing – the purpose is to smooth oscillatory interference but has the disadvantage of smearing localised components.
- Squeezing – the purpose is to refocus the contributions that survived the smoothing.

The result of this is illustrated in Figure 7.8. This is the reassigned version of the spectrogram given in Figure 7.6 and it is immediately clear that the detail within the visible modes is much sharper. Both the A_0 and S_0 modes are visible and there is also clear higher frequency structure.

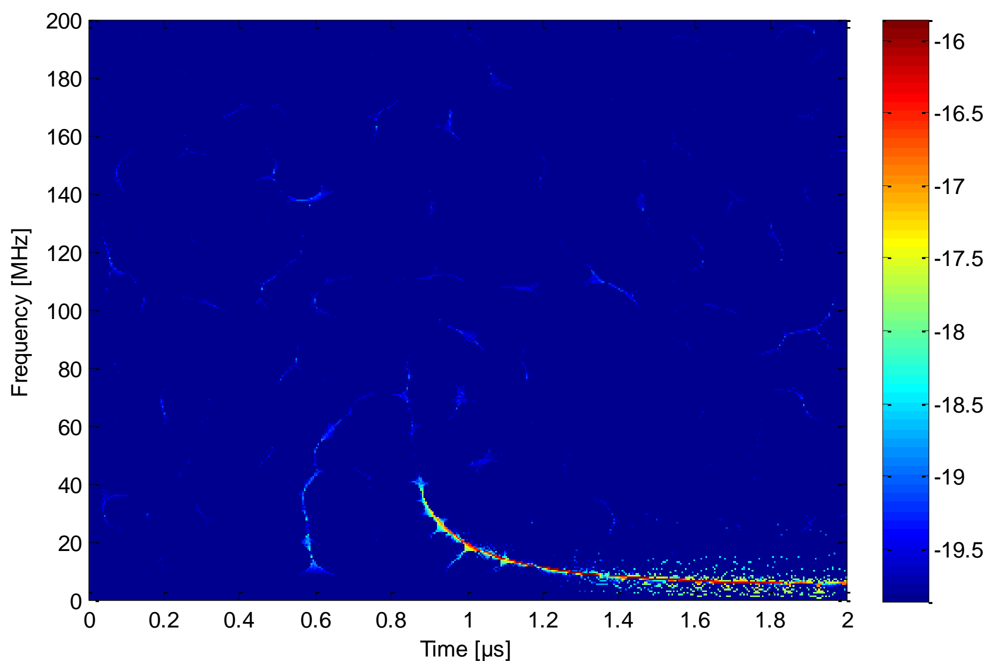

Figure 7.8: Reassigned spectrogram of Lamb wave.

7.5 Generating Guided Elastic Waves in a MEMS Pressure Sensor

The Lamb waves were excited in the membrane of a MEMS pressure sensor using a broadband laser source. The pressure sensors were discussed previously in Chapter 2 and are shown in Figure 7.9.

Figure 7.9 shows the pressure sensor diaphragms etched into a (100) n-type silicon wafer with stiffening boss. Also visible is a blank test plate which was used for the majority of measurements. The sample was mounted vertically in between the generation source laser and the Michelson interferometer, and was held in place using magnetic strips as shown in Figure 7.10. The generation source used was a Teem Photonics Powerchip PB Nano UV 355 laser (PowerChip-PNV-B25010-130) with pulse energy of 28 uJ, pulse width of 400 ps and repetition rate of 10 Hz. It was shown in Chapter 6 that a laser of wavelength 532 nm is more efficient at generating acoustic waves in silicon. However, the relative efficiency for 355 nm light given in Chapter 6 was 3.45, compared to 3.85 for 532 nm light. Therefore the difference between these two values can be considered negligible. Secondly, the laser quoted above was already available. The laser was mounted on a Newport motion controller translation stage (MM4005) which was used to adjust the laser in the y-axis, to adjust the source- detector distance and in the x-axis, to adjust the focusing of the laser beam. The beam was focused onto the sample using a UV cylindrical lens from Thorlabs and the optimal focus was obtained by firing the laser and finely adjusting the translation stage until the signal with the maximum signal to noise ratio was observed on an oscilloscope. The oscilloscope used was an Agilent Infiniium 54832D MSO oscilloscope and the signals were averaged 4096 times with each measurement. The experimental set up is shown in Figure 7.11. The detection interferometer was the Michelson interferometer detailed previously in Chapter 4.

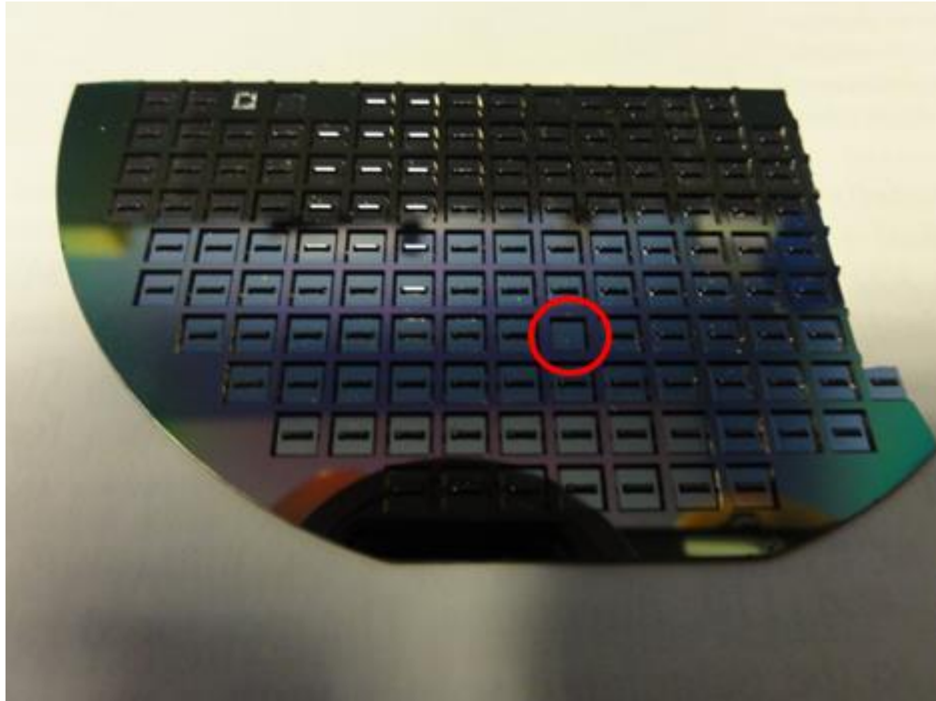

Figure 7.9: MEMS pressure sensor on wafer with test point highlighted.

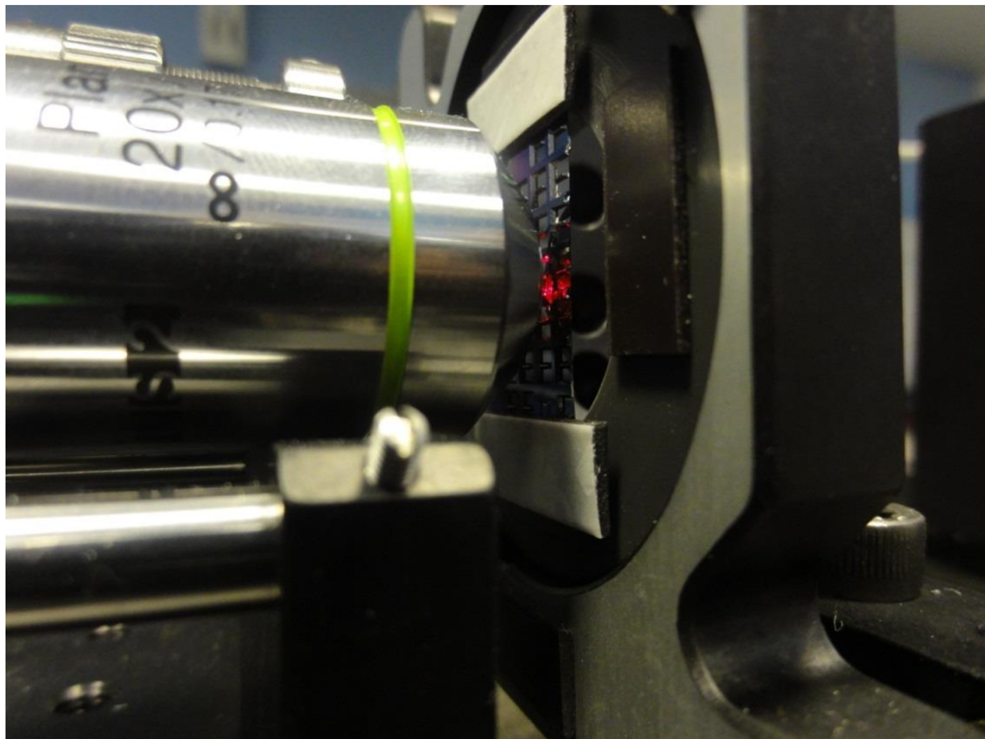

Figure 7.10: MEMS pressure sensors mounted in position.

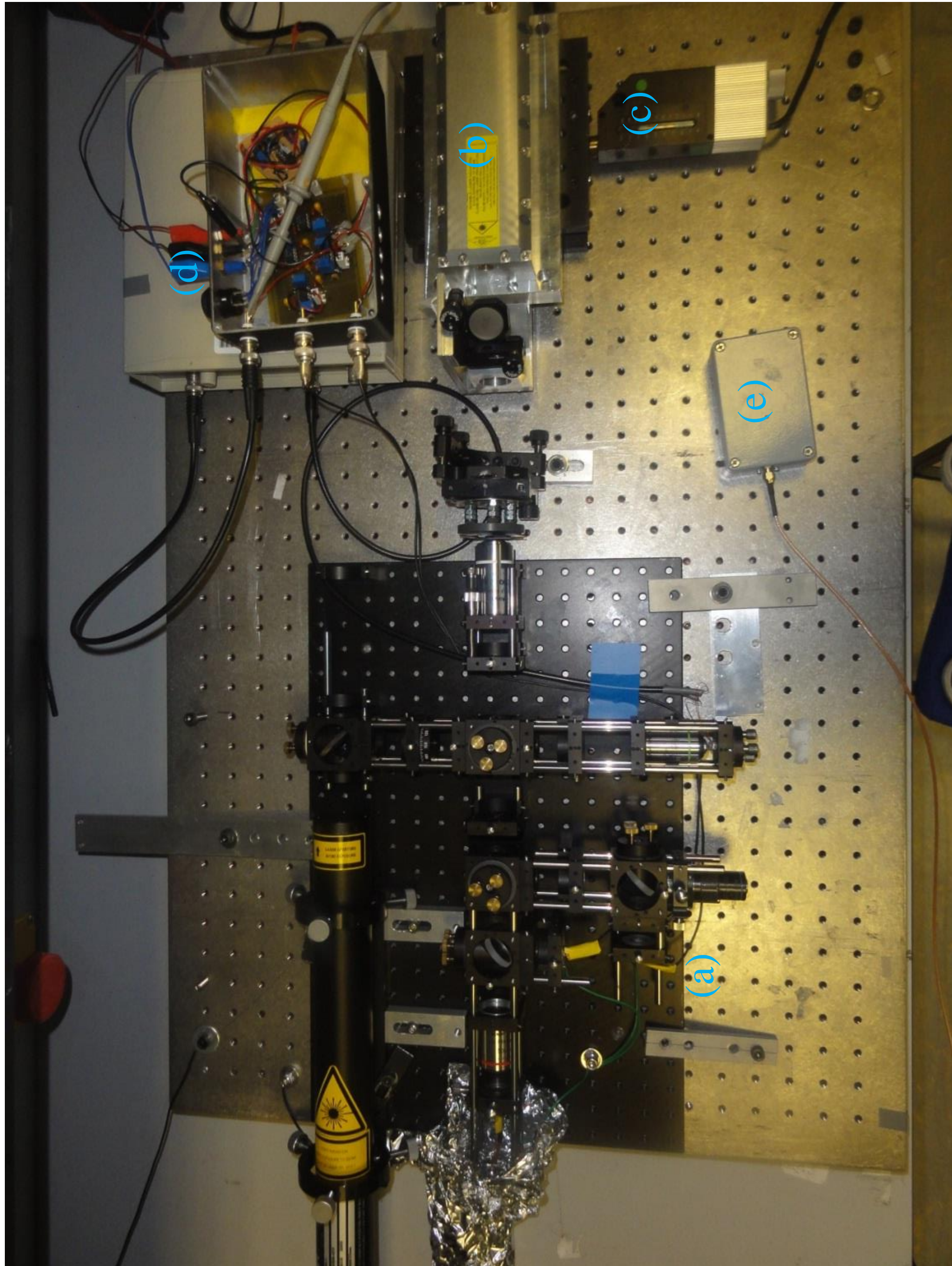

Figure 7.11: Experimental set up for the measurement of high frequency acoustic waves in silicon wafers and MEMS pressure sensors. Components shown are, (a) - Michelson interferometer, (b) - UV laser, (c) - translation stage, (d) - stabilisation circuit and (e) – trigger photodiode.

7.6 Dispersion Curve Sensitivity

The Lamb wave dispersion curves are sensitive to changes in material properties, such as Young's modulus, Poisson's ratio and thickness, but how sensitive are they and at what points are they most sensitive? The answer to this question is critical when the possibility of mode selection is available. Although not possible with a broadband source, if an excitation source was used that could excite the sample at a particular frequency, the answer to the question above shows the frequency ranges at which to excite the sample depending on what mode is desired. To answer the above question, group velocity and time frequency dispersion curves can be produced with starting values for each of the three variables above and monitor how the dispersion curve changes as a function of each. In order to choose a starting value for thickness, the thickness quoted for the silicon wafer from the supplier (*i.e.* 50 µm) will be used. For Poisson's ratio, the range of values in the literature [12] is from 0.28 to 0.36 so a good starting value is 0.32. Values for Young's modulus range from 130 GPa to 169 GPa [12, 13] so the starting point in this case will be 150 GPa. The following results assume a source detector separation of 1 mm, which is typical of the set up used for the MEMS pressure sensor characterisation. A density of 2329 kgm^{-3} is also assumed for silicon. The following tables show the material properties that were kept constant and those that changed. It should also be noted that it is a straight forward transformation from group velocity dispersion curves to time frequency dispersion curves and therefore these plots are only shown for reference. The relationship between group velocity and time-frequency dispersions curves is given as

$$c_g = \frac{d}{t} \qquad \textbf{7.7}$$

where c_g is the group velocity, d is the propagation distance and t is the propagation time for each frequency. The following modelled dispersion curves were produced using a MATLAB program developed within the Centre for Ultrasonic Engineering [14]. The constants quoted are Young's modulus E, Poisson's ratio υ and shear modulus G. the values for the constants are taken from [12].

Table 7.1: Material properties used for calculation of dispersion curves demonstrating dispersion curve sensitivity. Material properties are refer to the [110] direction in silicon.

Reference	Constant	Variable
Figure 7.12 to Figure 7.15	E = 169 GPa	
	v = 0.36	h = 50 µm (± 1%, ± 5% and ±10%)
	G = 79.6 GPa	
Figure 7.16 to Figure 7.19	h = 50 µm	
	v = 0.36	E = 150 GPa (± 1%, ± 5% and ±10%)
	G = 79.6 GPa	
Figure 7.20 to Figure 7.23	E = 169 GPa	
	h = 50 µm	v = 0.36 (± 1%, ± 5% and ±10%)
	G = 79.6 GPa	

7.6.1 Variation in Thickness

Varying the sample thickness affects the group velocity dispersion curve in a straightforward manner as illustrated in Figure 7.12 to Figure 7.15. Since the frequency component of the dispersion curve is dependent on thickness, increasing the sample thickness will decrease the frequency value. This however only becomes evident above approximately 30 MHz. The A_0 mode is relatively insensitive to changes in thickness and it would need a large increase in thickness to reduce the frequency component of the A_0 mode and this would be evident in the dispersive region. However, such drastic changes would never occur. While the S_0 mode is sensitive to changes in thickness at its dispersive region, the most sensitive mode is the S_1 mode at zero group velocity. The A_1 mode is also sensitive to changes in thickness, but not as much as the S_1 mode. The S_1 mode is a resonant mode in the sample and this will be addressed in more detail in section 7.7.3.

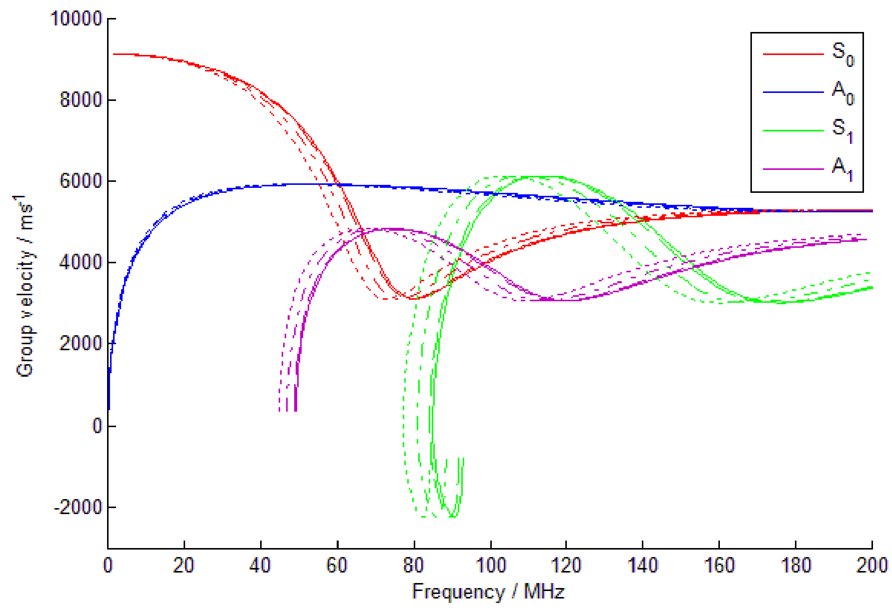

Figure 7.12: Variation in group velocity dispersion curve with increasing sample thickness. *E* = 169 GPa, *υ* = 0.36, *G* = 79.6 GPa. *h* = (50 µm, +1%, +5%, +10%).

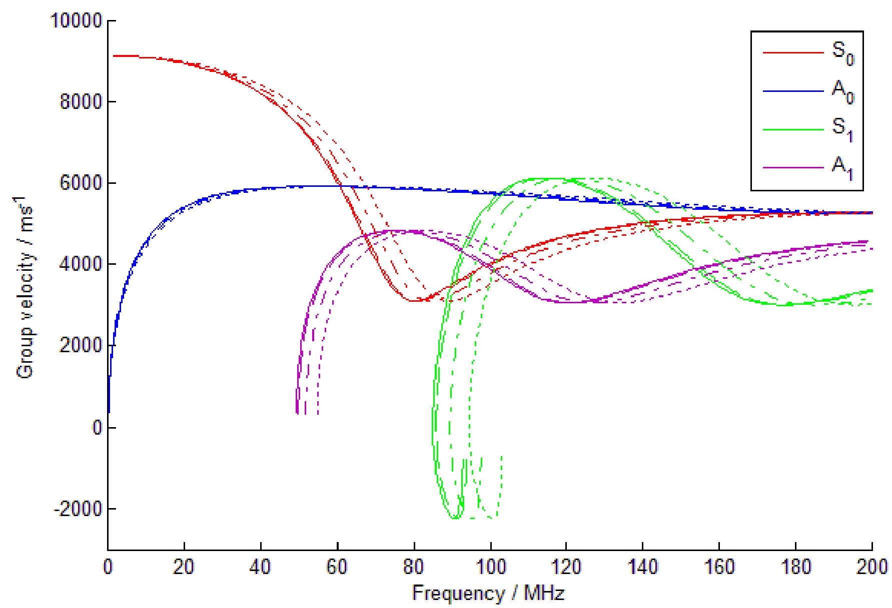

Figure 7.13: Variation in group velocity dispersion curve with decreasing sample thickness. *E* = 169 GPa, *υ* = 0.36, *G* = 79.6 GPa. *h* = (50 µm, -1%, -5%, -10%).

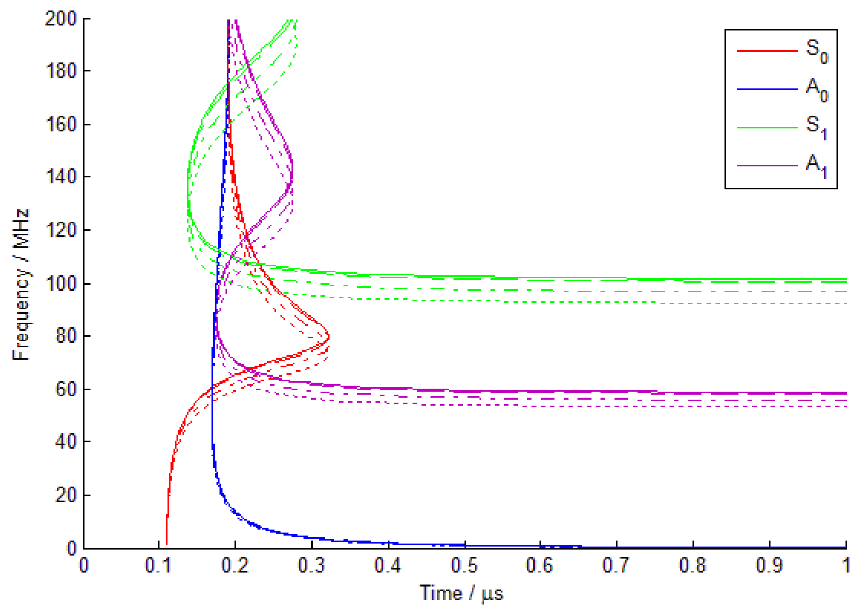

Figure 7.14: Variation in time frequency dispersion curve with increasing sample thickness. E = 169 GPa, υ = 0.36, G = 79.6 GPa. h = (50 µm, +1%, +5%, +10%).

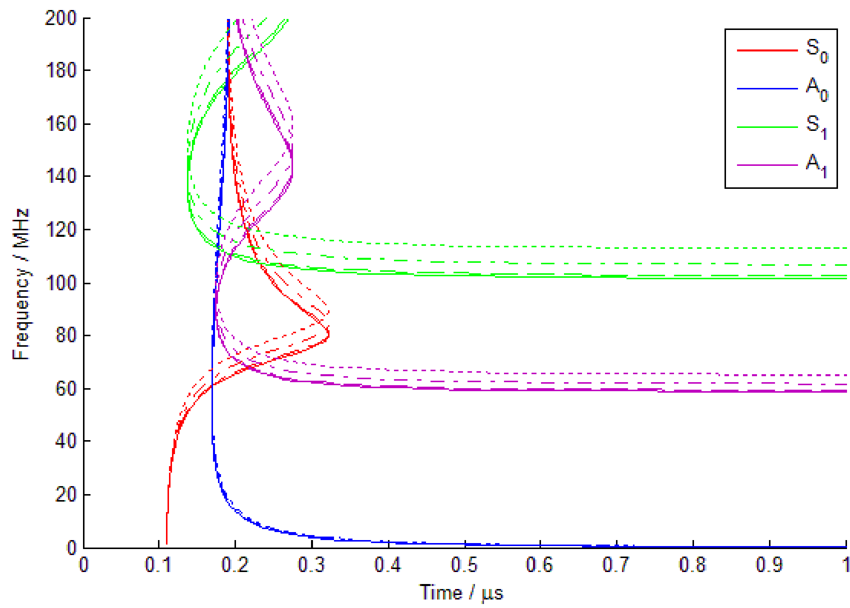

Figure 7.15: Variation in time frequency dispersion curve with decreasing sample thickness. E = 169 GPa, υ = 0.36, G = 79.6 GPa. h = (50 µm, -1%, -5%, -10%).

7.6.2 Variation in Young's Modulus

Variations in Young's modulus do not really affect the A_0 mode. However, at certain frequencies they can drastically affect the S_0, A_1 and S_1 modes. The low frequency component of the S_0 mode is very sensitive to changes in Young's modulus and from the three variables tested, this seems to be the only one that has any effect on this mode at this frequency range. An increase in Young's modulus increases the non-dispersive velocity of the S_0 mode *i.e.* the sheet (or plate) velocity. Likewise, increasing Young's modulus increases the frequency component of the S_1 mode at zero group velocity.

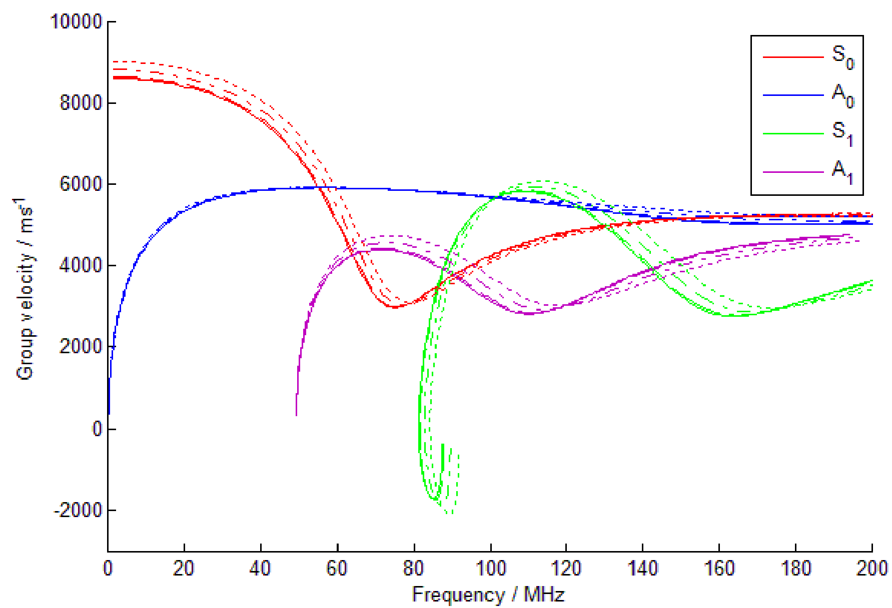

Figure 7.16: Variation in group velocity dispersion curve with increasing Young's modulus. *h* = 50 µm, *υ* = 0.36, *G* = 79.6 GPa. *E* = (169 GPa, +1%, +5%, +10%).

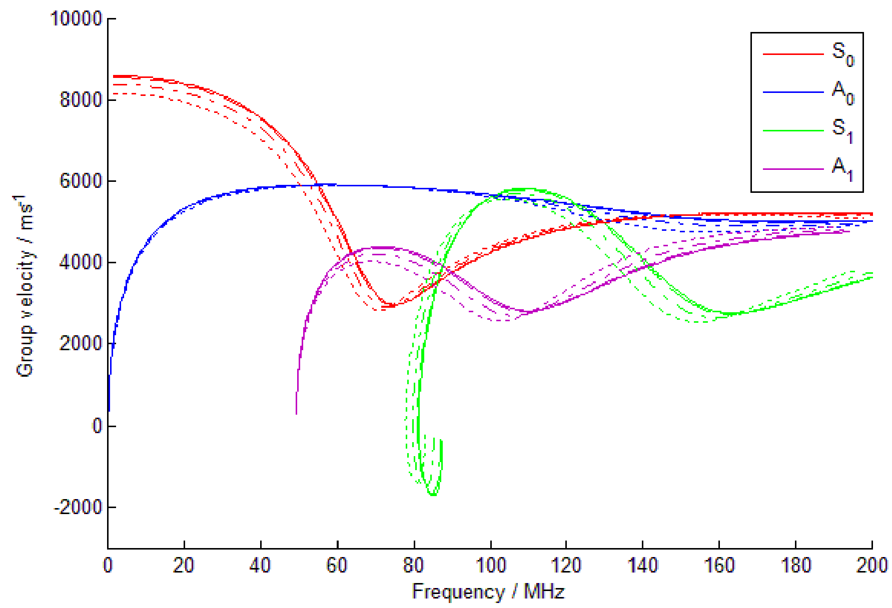

Figure 7.17: Variation in group velocity dispersion curve with decreasing Young's modulus. h = 50 µm, υ = 0.36, G = 79.6 GPa. E = (169 GPa, -1%, -5%, -10%).

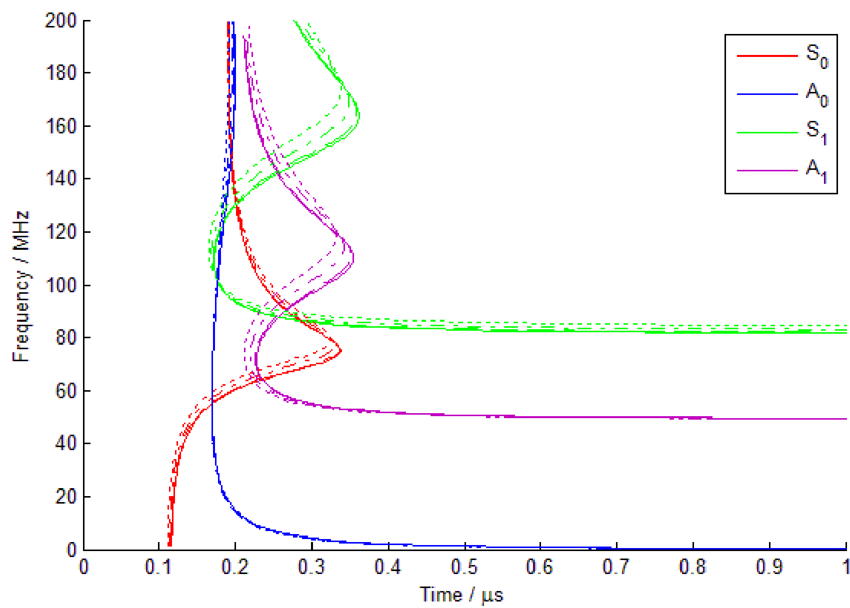

Figure 7.18: Variation in time frequency dispersion curve with increasing Young's modulus. h = 50 µm, υ = 0.36, G = 79.6 GPa. E = (169 GPa, +1%, +5%, +10%).

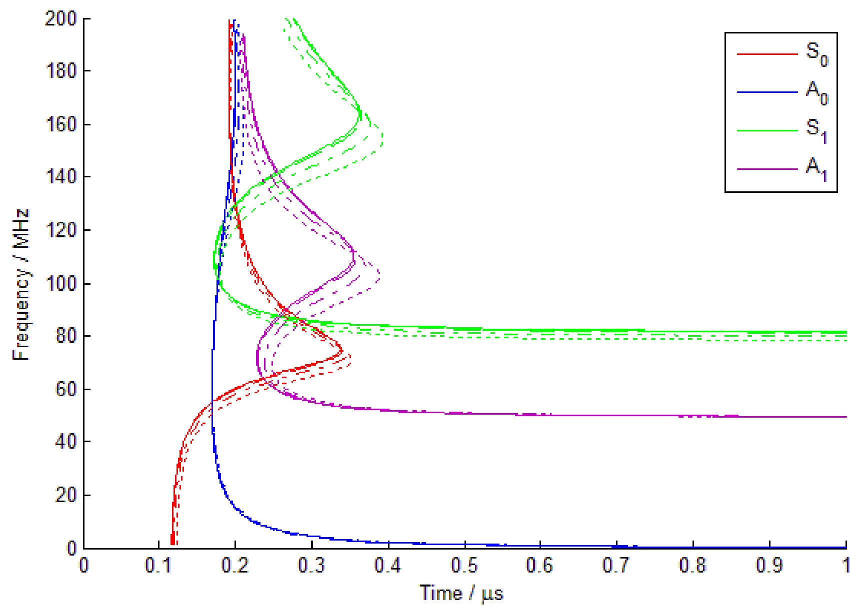

Figure 7.19: Variation in time frequency dispersion curve with decreasing Young's modulus. *h* = 50 µm, *υ* = 0.36, *G* = 79.6 GPa. *E* = (169 GPa, -1%, -5%, -10%).

7.6.3 Variation in Poisson's Ratio

Again, variations in Poisson's ratio do not really affect the A_0 and A_1. The symmetric modes are more sensitive than the anti symmetric modes, and it can be seen that the S_1 mode is much more sensitive than the S_0 mode. Variations in Poisson's ratio have a small effect on the dispersive part of the S_0 mode. Like Young's modulus, increasing Poisson's ratio increases the frequency component of the S_1 mode at zero group velocity.

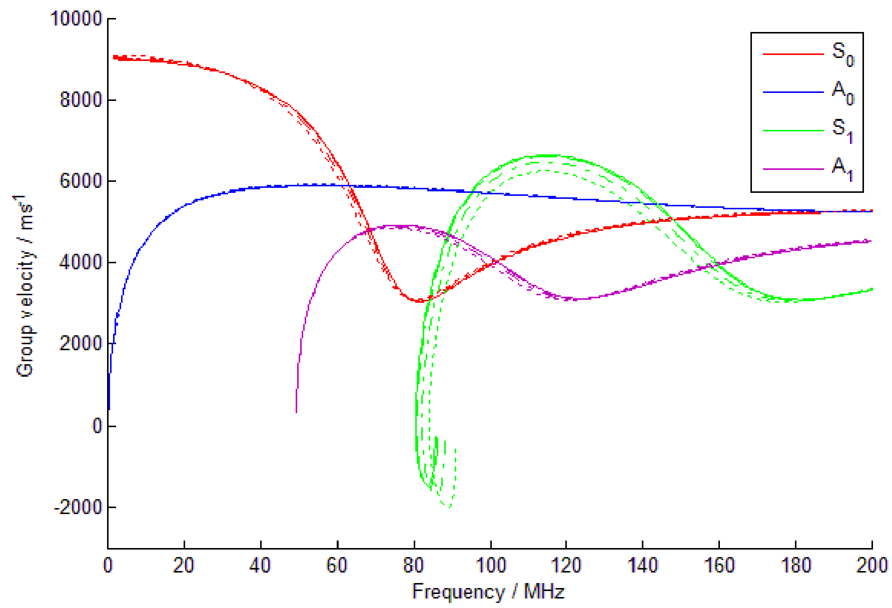

Figure 7.20: Variation in group velocity dispersion curve with increasing Poisson's ratio. E = 169 GPa, h = 50 µm, G = 79.6 GPa. υ = (0.36, +1%, +5%, +10%).

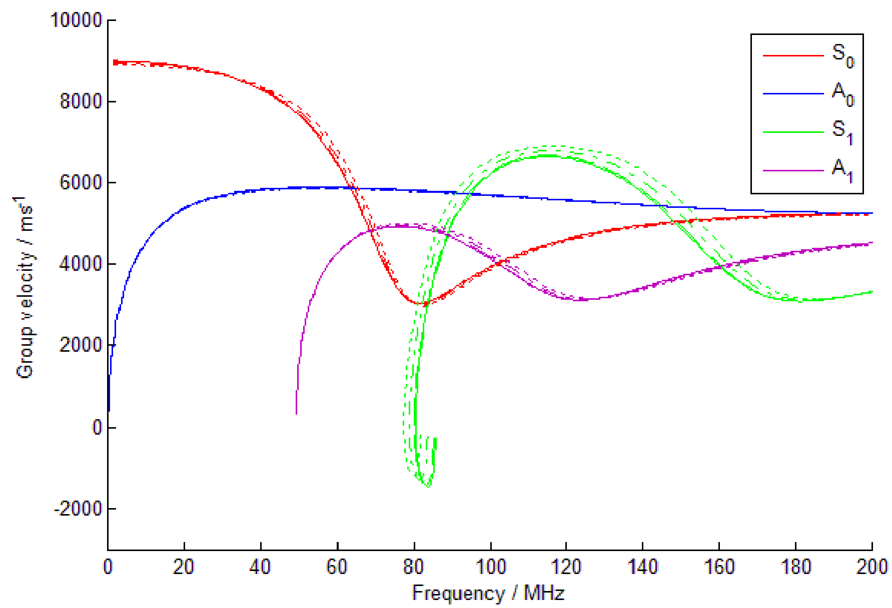

Figure 7.21: Variation in group velocity dispersion curve with decreasing Poisson's ratio. E = 169 GPa, h = 50 µm, G = 79.6 GPa. υ = (0.36, -1%, -5%, -10%).

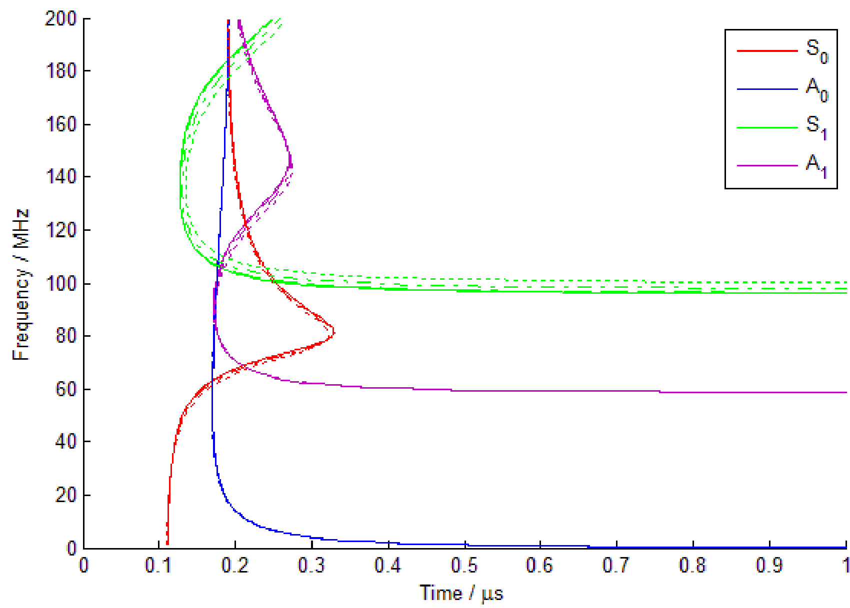

Figure 7.22: Variation in time frequency dispersion curve with increasing Poisson's ratio. *E* = 169 GPa, *h* = 50 µm, *G* = 79.6 GPa. υ = (0.36, +1%, +5%, +10%).

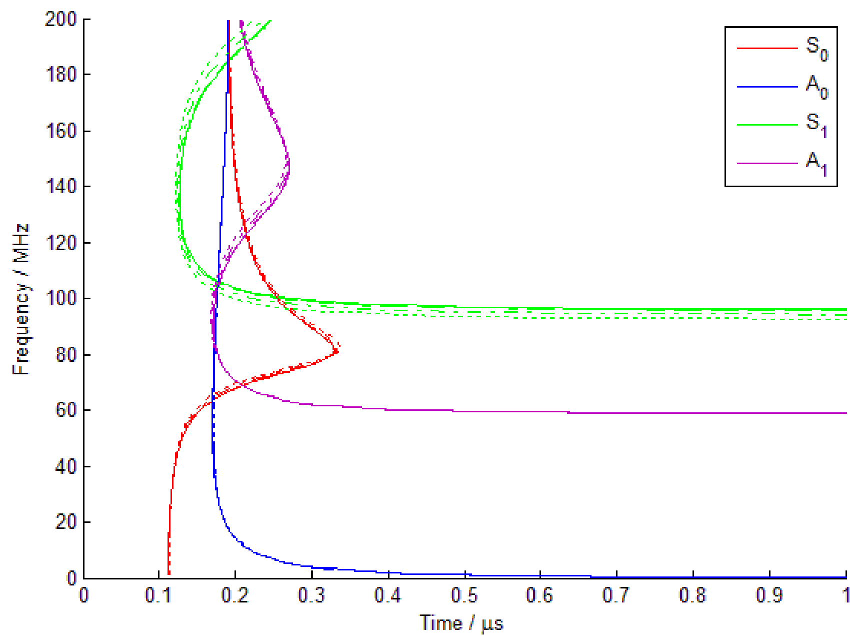

Figure 7.23: Variation in time frequency dispersion curve with decreasing Poisson's ratio. *E* = 169 GPa, *h* = 50 µm, *G* = 79.6 GPa. υ = (0.36, -1%, -5%, -10%).

In all cases, the A_0 mode is insensitive to changes in the material properties, with the exception of changes in thickness. The A_1 mode is relatively insensitive to material properties also.

In general, lower order modes are less sensitive to material property changes than higher order modes and the higher order modes appear to be more sensitive as they approach a lower group velocity. The value of the low frequency non-dispersive component of the S_0 mode is known as the plate velocity, defined as:

$$C_s = E^{\frac{1}{2}}[\rho(1-\upsilon^2)]^{-\frac{1}{2}} \quad \textbf{7.8}$$

where E is Young's modulus, ρ is the material density and υ is Poisson's ratio. It is obvious that changes in both Young's modulus and Poisson's ratio have a large impact on the plate velocity in the group velocity dispersion curve, but thickness has no impact. In an anisotropic material, in a direction of high symmetry, it can be assumed the plate velocity and group velocity of the low frequency S_1 mode are equal [15].

7.7 The MEMS Pressure Sensor

The experimental setup described in section 7.5 was used to perform measurements on membranes of the MEMS pressure sensor described previously. These were conducted on the blank test plate. The wave propagates in the [110] direction.

Figure 7.24 below shows the raw measured signal while Figure 7.25 shows the same data filtered using a Chebyshev Type II digital bandpass filter between 5 MHz and 250 MHz. This type of filter is not as common as the Type I filter, and it does not roll off as fast, but it has no ripple in the passband making it more ideal.

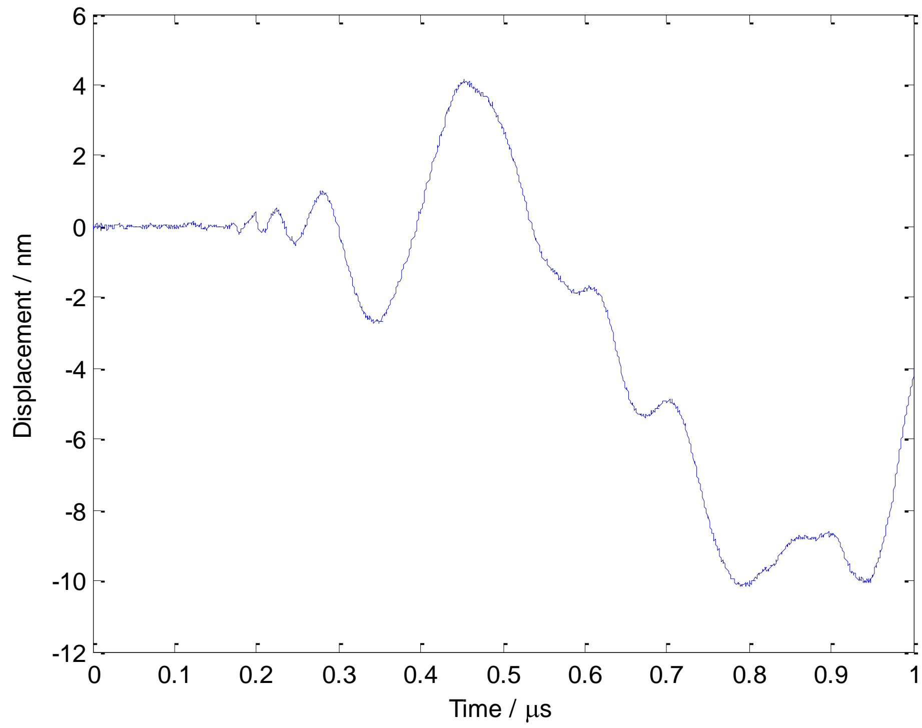

Figure 7.24: Measured Lamb wave generated in MEMS pressure sensor.

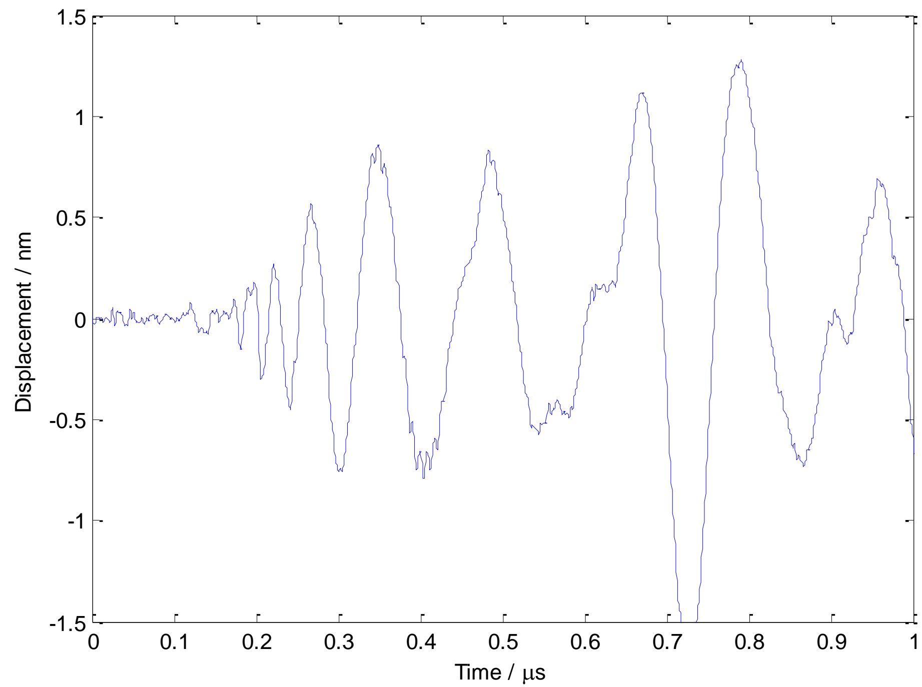

Figure 7.25: Measured data after bandpass filter between 5 MHz and 250 MHz is applied.

To obtain the group velocity dispersion curve, the reassigned Gabor transform is applied to the data using the MATLAB Time-Frequency Toolbox [16]. The Gabor transform is similar to the short time Fourier transform with the exception that the Gabor transform uses a Gaussian window. This gives a better time and frequency resolution as the signal is more concentrated than the rectangular window for example. This results in the following time-frequency representation of Figure 7.26.

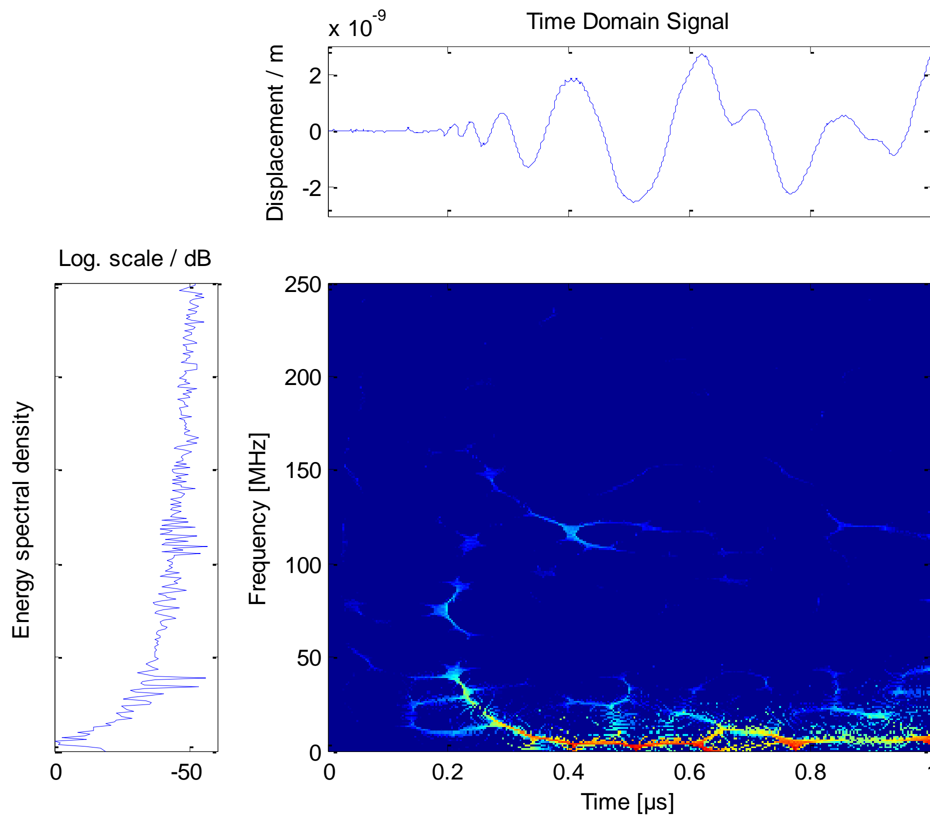

Figure 7.26: Reassigned Gabor time-frequency representation on the detected Lamb wave measured in the MEMS pressure sensor membrane. Also showing measured signal and energy spectral density.

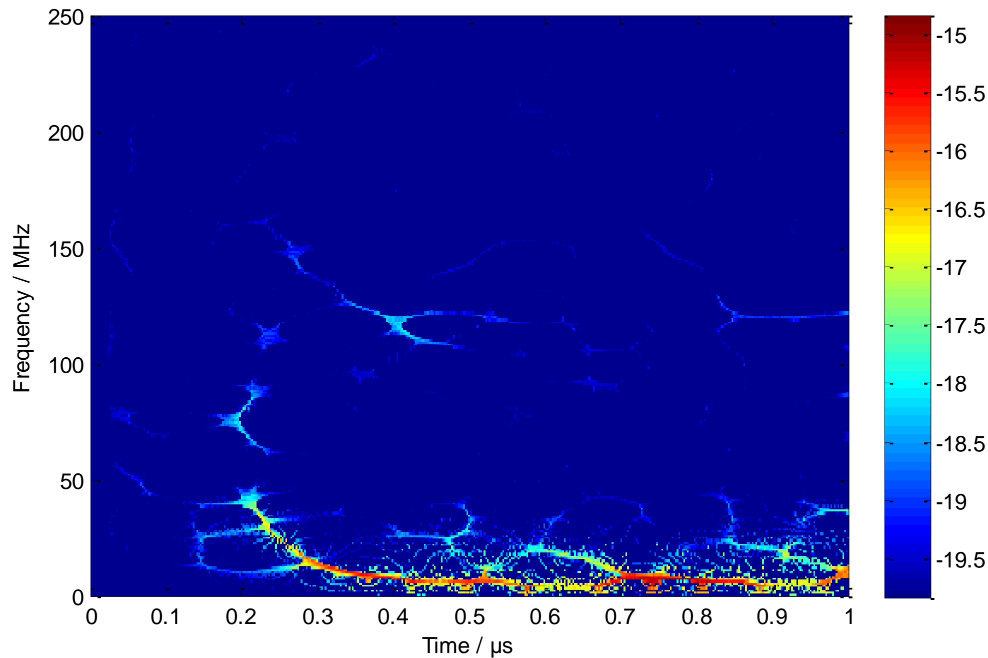

Figure 7.27: Reassigned Gabor time-frequency representation on the detected Lamb wave measured in the MEMS pressure sensor membrane.

Figure 7.26 and Figure 7.27 contain all the information needed to determine the thickness of the membrane along with values for group velocity, plate velocity, Rayleigh velocity, Young's modulus and Poisson's ratio. Figure 7.26 also shows the energy spectral density, or how the energy of the signal is distributed with frequency. A point to consider is there is no closed form mathematical expression to relate group velocity to elastic constants, which may be manipulated to obtain elastic constants. Developing one would be of enormous complexity and would present severe challenges for computerised optimisation [15]. Knowing this, the only method for obtaining material properties is by measuring the group velocities of each mode at various frequencies and using the equations presented in Chapter 5.

One aspect that must be considered is the possibility of the silicon being doped. As previously stated in this thesis, there was no prior knowledge of any of the properties of the silicon wafer, and as such a few assumptions have to be made. It is assumed the density is 2329 kgm^{-3}. It is also assumed that the transverse wave velocity in the

[110] direction is 5844 ms^{-1} [17]. There is every likelihood the wafer has been doped with another element, possibly phosphorus. It is however, generally accepted that doping has no effect on material properties including wave velocities, assuming doping levels are $<10^{20}$ cm^{-3} [18]. For very heavy doping, the material properties will typically decrease by approximately 1% to 3% [12]. Finally, the source-detector propagation distance is 1.25 mm.

7.7.1 Plate velocity

The group velocity, like the phase velocity, is dispersive so when group velocity is quoted, it must be for a particular mode. One mode of importance is the non-dispersive component of the S_0 mode, *i.e.* the low frequency component.

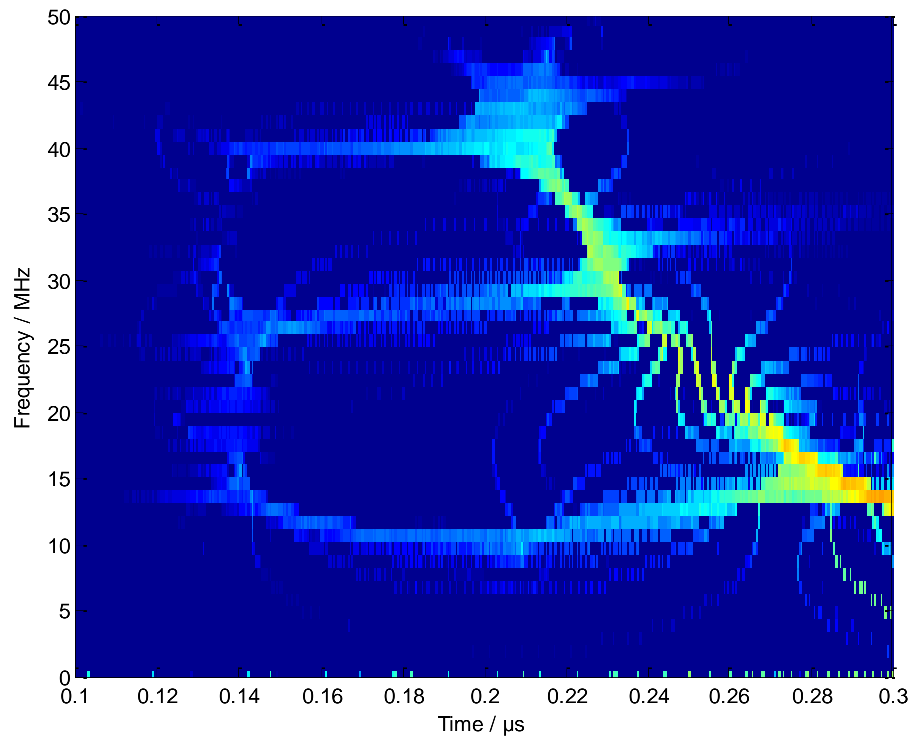

Figure 7.28: Low frequency S_0 and A_0 modes.

Figure 7.27 and Figure 7.28 show the arrival time of the S_0 mode. Figure 7.28 is the magnified version of Figure 7.27, from 0 MHz – 50 MHz and 0.1 μs – 0.3 μs It also shows a high region of dispersion in the A_0 mode. Concentring on the S_0 mode, the

arrival time occurs at 0.14 μs. Considering a propagation distance of 1.25 mm, this equates to a group velocity of 8930 ms^{-1} ± 320 ms^{-1}. This is also the value for the plate velocity within the membrane.

7.7.2 Rayleigh velocity

The Rayleigh velocity of a Lamb wave is the point on a phase velocity dispersion curve where the fundamental symmetric and anti-symmetric modes meet. In other words, it is the point where the frequency of the wave becomes too large to be confined within the plate boundaries. At this point, the wave travels along the surface and the sample acts like a half space.

The time-frequency plot in Figure 7.27 shows the point where the A_0 and S_0 modes almost meet. Note this is higher than the Rayleigh wave in phase velocity dispersion curves and so the A_0 velocity is the Rayleigh velocity. The two modes can be seen converging in Figure 7.29, with the A_0 mode on the left and the S_0 mode on the right.

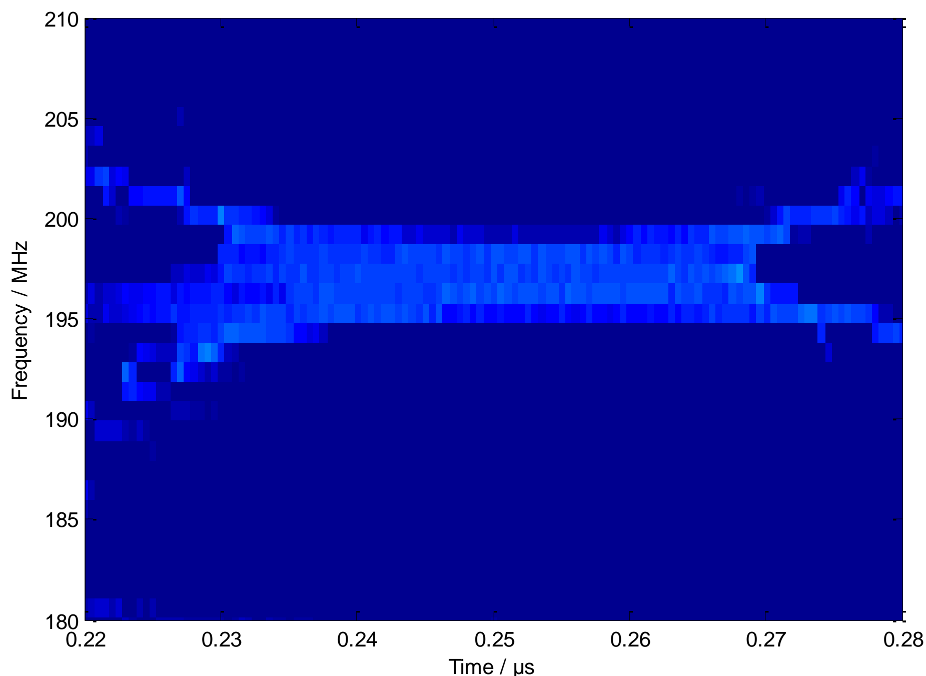

Figure 7.29: Onset of Rayleigh wave.

Using equation 7.7, it has been calculated that the Rayleigh wave has a velocity of 5465 ms^{-1} ± 145 ms^{-1}. From this a value of Poisson's ratio can be obtained.

Figure 7.28 and Figure 7.29 both highlight a problem with the reassigned time-frequency method. On the left of Figure 7.29 is some structure believed to be the Rayleigh wave associated with the A_0 mode. On the right is the S_0 mode approaching the Rayleigh velocity. In between these two modes however is interference caused by two closely spaced components. With time-frequency representations, there is a trade off between resolution and localisation. If more than one component is seen with a time-frequency smoothing window, a beating effect occurs causing interference fringes. This limits the reassigned time-frequency method from being a "super resolution" process.

7.7.3 The S_1 mode and membrane thickness

One interesting property of Lamb waves is that at specific frequencies, the group velocity tends towards zero while the phase velocity remains finite. When the phase velocity becomes infinite, the group velocity is zero, meaning the plate vibrates in longitudinal or shear thickness mode resonance. These resonances become uniformly distributed on the plate surface. The minimum wave mode (or frequency) where this is observed is the S_1 mode, but it can also occur in higher modes [19, 20]. The S_1 mode has been shown to have a very large quality factor [19], making it ideal for bulk acoustic wave velocity and mentioned thickness measurements. This is evident in the FFT of the measured signal, shown in Figure 7.30. The maximum peak shown at 120 MHz is the S_1 resonant mode.

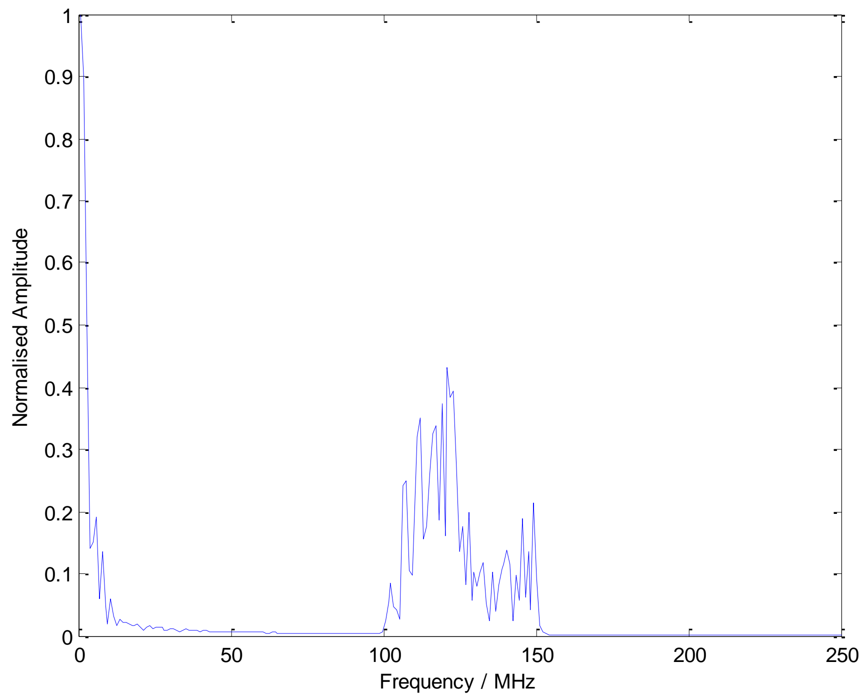

Figure 7.30: FFT of measured signal. S1 mode is visible at ≈120 MHz. (Signal bandpass filtered between 100 MHz and 150 MHz).

The S_1 mode (along with other higher order modes) originate at a particular cut off frequency. At this frequency, the plate vibrates in longitudinal or shear thickness mode resonance. For the S_1 mode, this point is a function of longitudinal velocity, C_L and the plate thickness, h.

$$f_R = \frac{C_L}{2h} \tag{7.9}$$

The origins of the S_1 zero group velocity resonance stems from the behaviour of the dispersion curve. The group velocity is zero at a frequency, f_{S1}, shown in Figure 7.31 at 120 MHz. The (wavenumber) dispersion curve consists of two branches with two different slopes. Figure 7.31 contains two modes, the S_1 mode in green and the S_2 mode in magenta. The upper branch belongs to the S_2 mode. This mode is considered a backwards propagating mode (giving it the designation S_{2b}) as the phase and group velocities are of opposite sign resulting in the propagation of acoustic energy being

different to that of the wave vector. The lower branch of the dispersion curve has phase and group velocities of the same direction and this is considered the true S_1 mode. The absolute value of the group velocity of the S_1 and S_{2b} modes approach zero and interfere with each other forming the standing S_1 zero group velocity mode [19].

The experimental setup was not optimal for this measurement. In order to observe as many modes as possible, the laser generation beam was focused onto the surface quite tightly. It has been shown [19] that there is a maximum peak (spot size) where upon the maximum resonant S_1 mode is observed. This happens when the spot size is approximately half an acoustic wavelength and as a result in this case leads to a lower quality signal.

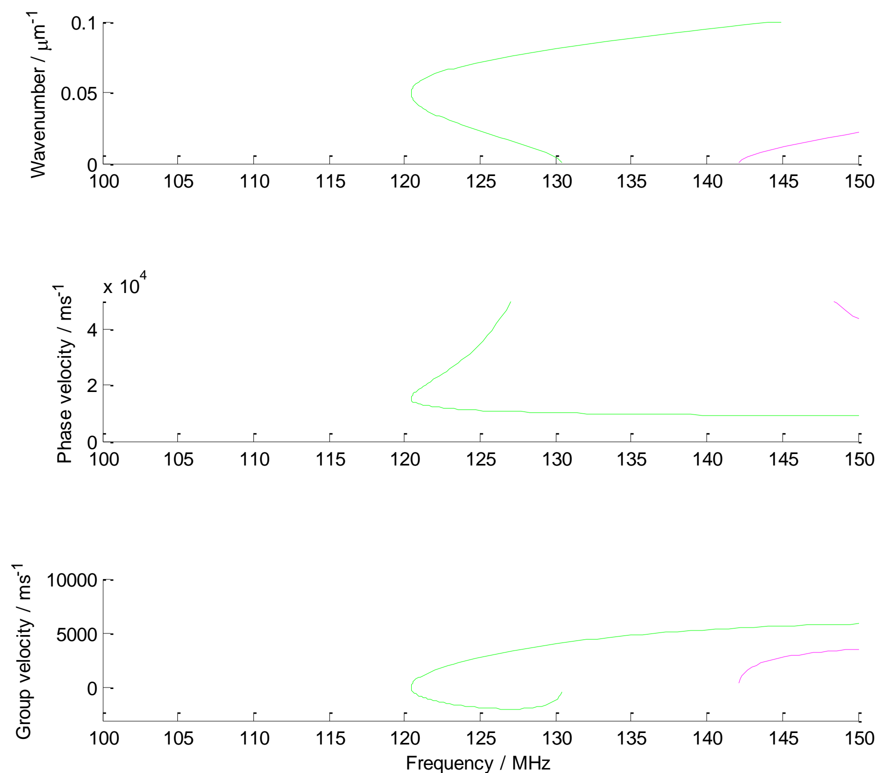

Figure 7.31: Modelled wavenumber, phase velocity and group velocity dispersion curves for the S_1 (green) and S_2 (magenta) modes using material property estimates for MEMs pressure sensor.

Figure 7.32 shows that the zero group velocity of the S_1 mode occurs at a frequency of 120.43 MHz ± 0.64 MHz, equating to a thickness of 35.01 μm ± 0.18 μm using equation 7.9.

The S_1 mode is also very sensitive to changes in thickness [20]. This was first seen in Figure 7.14 and Figure 7.15. The sensitivity to change in thickness δh can be given as

$$\delta h = \frac{h\delta f}{f} \qquad \textbf{7.10}$$

where δf and f are the frequency shift and frequency respectively. If the resonance peak shifts on the order of 0.1 MHz, and with a measured frequency of 120 MHz and a thickness of 35 μm, changes of thickness of 292 nm (approximately 0.8%) can be observed.

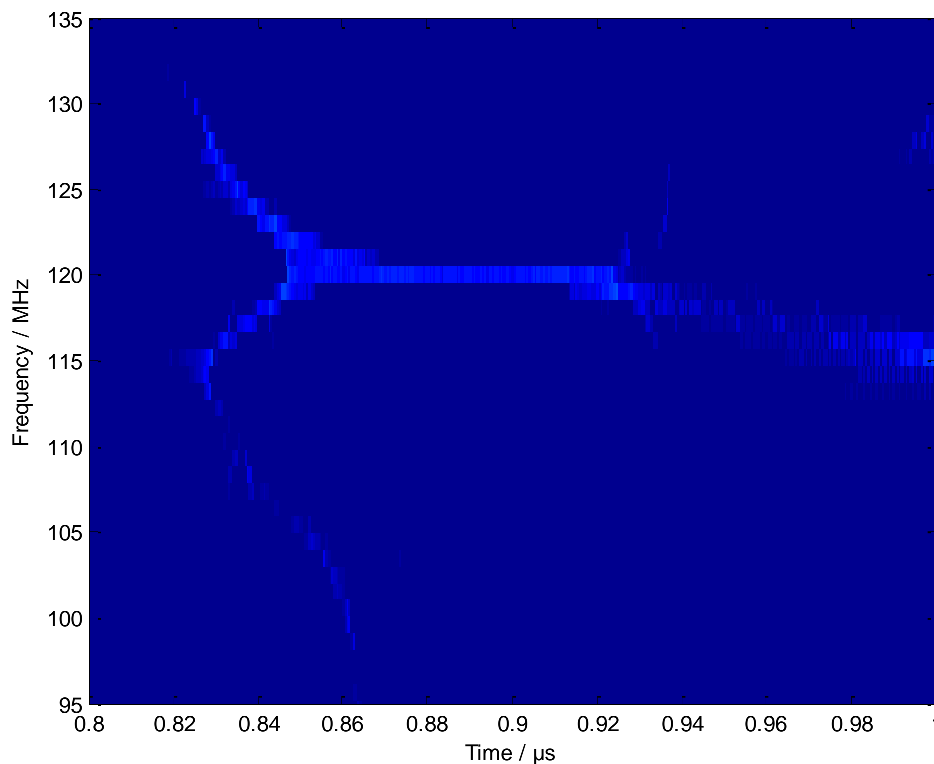

Figure 7.32: Measure S_1 mode approaching zero group velocity.

7.8 Estimation of Young's modulus and Poisson's ratio in the [110] direction

The solution to the Rayleigh wave equation is given as [21]

$$C_R = \frac{0.862 + 1.14\upsilon}{1 + \upsilon} C_T \quad \textbf{7.11}$$

where C_R is the Rayleigh velocity, υ is Poisson's ratio and C_T is the transverse velocity. While equation 7.11 is listed in [21], a second equation is also given.

$$C_R = \frac{C_T}{1.14418 - 0.25771\upsilon + 0.12661\upsilon^2} \quad \textbf{7.12}$$

The author of [21] references the first of these equations to Achenbach [22] and the second as a private communication (Sinclair). However, the author choses to use the second equation.

Using equation 7.12, a value for Poisson's ratio of 0.351 is obtained. At this value for the Rayleigh wave velocity there is a 0.098% variation in the calculation. For completeness, equation 7.11 gives a value of 0.357 for Poisson's ratio.

Having calculated a value for the plate velocity and Poisson's ratio, (using the value of 0.351), Young's modulus can now be found. Using equation 7.8, Young's modulus can be shown to be 163 GPa ± 11.7 GPa.

7.9 Experimental and theoretical results

This final section pulls together the measured time-frequency spectrogram and using the determined material properties. Combined plots showing the time-frequency and group velocity dispersion curves are given. The time frequency plot (Figure 7.33) shows good agreement with the theoretical curves with the exception of the high frequency S_0 mode. Overall, the theoretical and measured curves could possibly be brought closer together if the items in section 7.10 are addressed.

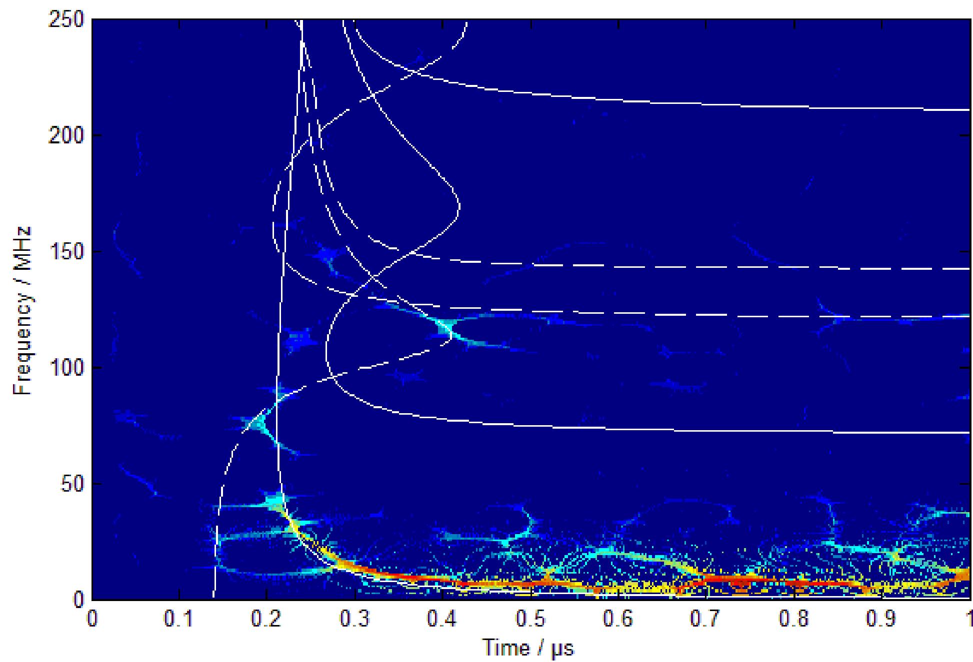

Figure 7.33: Measured and theoretical time-frequency dispersion curve for MEMS pressure sensor membrane. Solid lines refer to the antisymmetric modes and dashed lines refer to the symmetric modes.

Again, Figure 7.34 shows good agreement between the theoretical and measured point. In both these plots, the mostly dominant source of error is the distribution of the points during the reassignment process caused by neighbouring modes. In the group velocity dispersion curve these look quite isolated. However, upon comparing the group velocity dispersion curve with the time-frequency dispersion curve, it is clear there are a considerable number of locations where this interference can occur. As mentioned above, this unfortunately is unavoidable.

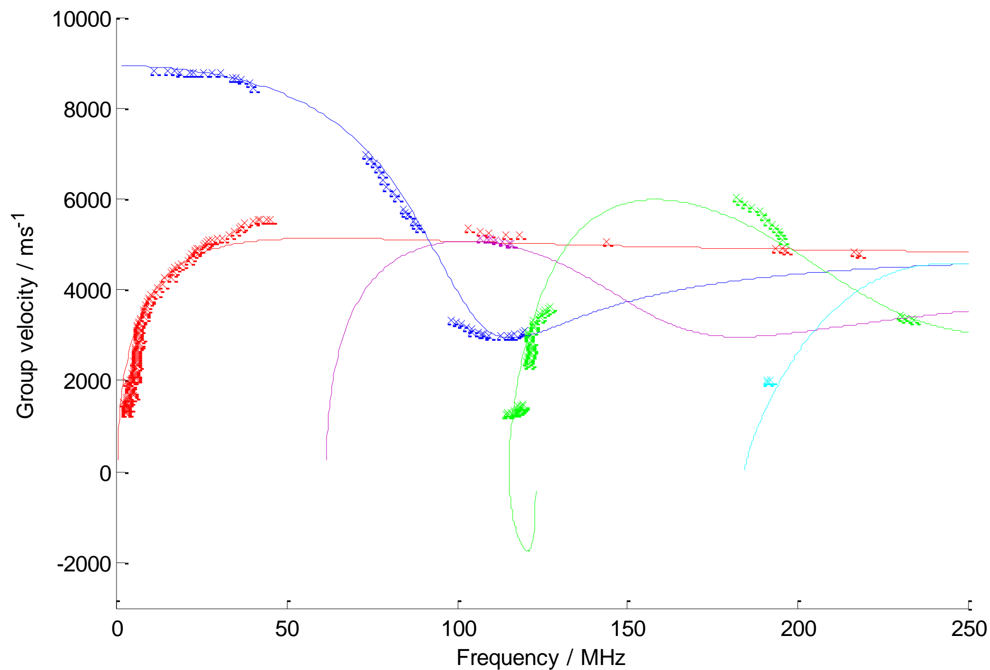

Figure 7.34: Measured and theoretical group velocity dispersion curve for MEMS pressure sensor membrane. Solid lines refer to theoretical dispersion curves and crosses show the measured points.

7.10 Future Experiments

Future work would include the same methodology with the exception that the excitation would occur on the silicon side of the membrane instead of the metallic side. This would have induced a photostrictive response in the membrane as well as a thermoelastic response, providing a better estimate of Poisson's ratio.

It would also be advantageous to repeat the measurements described above, but also rotating the sample by a fixed angle per measurement. This would demonstrate the anisotropic nature of silicon and provide the mechanical properties in other crystal planes.

7.11 Conclusions

This chapter has shown that even by taking a single measurement and performing time frequency analysis, an accurate value for membrane thickness using the S_1 mode can be calculated. This was calculated to be 35.01 μm ± 0.18 μm and will be verified in the next chapter. Values of 163 GPa ± 11.7 GPa for Young's modulus and 0.351 for Poisson's in the [110] direction have also been otained. Comparing these to values taken from [12], Hopcroft quotes 169 GPa (3.6% greater than the value obtained in this work) for Young's modulus and 0.36 (2.5% greater that the value obtained in this work) for Poisson's ratio.

While there is some discrepancies in these results, the experimental costs, setup and run time are less (much less in terms of run time) than that required to perform a 2D-FFT.

7.12 References

[1] D. Alleyne and P. Cawley, "A two-dimensional Fourier transform method for the measurement of propagating multimode signals," *J. Acoust. Soc. Am.,* vol. 89, no. 3, pp. 1159-1168, 1991.

[2] "Nanopositioning," Attocube, 2001-2012. [Online]. Available: http://www.attocube.com/nanoPOSITIONING/nanopositioning.html.

[3] D. Gabor, "Theory of communication. Part 1: The analysis of information," *J.IEE,* vol. 93, no. 26, pp. 429-441, 1946.

[4] K. R. Fitz and S. A. Fulop, "A unified theory of time–frequency reassignment.," *Preprint posted on arXiv.org,* 2005.

[5] S. Hurlebaus, M. Niethammer, L. J. Jacobs and C. Valle, "Automated methodology to locate notches with Lamb waves," *J. Acoust. Soc. Am,* vol. 2, no. 4, pp. 97-102, 2001.

[6] A. Mertins, Signal Analysis: Wavelets, Filter Banks, Time Frequency Transforms and Applications, John Wiley & sons, 1999.

[7] B. Sorazu, “Optical Techniques for examining mechanical Materials,” 2006.

[8] M. Niethammer, L. J. Jacobs, J. Qu and J. Jarzynski, “Time-frequency representation of Lamb waves using the reassigned spectrogram.,” *J. Acoust. Soc. Am.,* vol. 107, no. 5, pp. L19-L24, 2000.

[9] “Goodfellow,” [Online]. Available: http://www.goodfellow.com/.

[10] F. Auger and P. Flandrin, “Improving the readability of time-frequency and time-scale representations by the reassignment method,” *IEEE. Trans. Signal Processing,* vol. 43, no. 5, pp. 1068-1089, 1995.

[11] S. W. Hainsworth and M. D. Macleod, “Time Frequency Reassignment: A Review and Analysis”.

[12] M. A. Hopcroft, W. D. Nix and T. W. Kenny, “What is the Young’s Modulus of Silicon?,” *J. Microelectromech. Syst.,* vol. 19, no. 2, pp. 229-238, 2010.

[13] E. Boyd and D. Uttamchandani, “Measurement of the anisotropy of Young’s Modulus in single-crystal Silicon using a wagon-wheel test structure,” *J. Microelectromech. Syst.,* vol. 21, no. 1, pp. 243-249, 2012.

[14] I. Veres, *Private Communication.*

[15] A. G. Every and W. Sachse, “Determination of the elastic constants of anisotropic solids from acoustic-wave group-velocity measurements,” *Phys. Rev. B,* vol. 42, no. 13, pp. 8196-8205, 1990.

[16] F. Auger, P. Flandrin, P. Goncalves and O. Lemoine, *Time-Frequency Toolbox: For use with MATLAB,* CNRS and Rice University, 1996.

[17] H. J. McSkimin and P. Andreatch, “Elastic moduli of silicon vs hydrostatic pressure at 25.0°C and -195.8°C,” *J. Appl. Phys.,* vol. 35, no. 7, pp. 2161-2165, 1964.

[18] W. C. Crone, “A Brief Introduction to MEMS and NEMS,” in *Springer Handbook of Experimental Solid Mechanics*, W. N. Sharpe, Ed., 2008.

[19] O. Balogun, T. Murray and C. Prada, “Simulation and measurement of the optical excitation of the S1 zero group velocity Lamb wave resonance in plates,” *J. Appl. Phys.,* vol. 102, pp. 064914-1 - 064914-10, 2007.

[20] C. Prada, O. Balogun and T. W. Murray, "Laser-based ultrasonic generation and detectionof zero-group velocity Lamb waves in thin plates," *Appl. Phys. Lett.,* vol. 87, p. 194109, 2005.

[21] C. B. Scruby, K. R. Jones and L. Antoniazzi, "Diffraction of elastic waves by defects in plates: Calculated arrival strengths for point force and thermoelastic sources of ultrasound.," *J. Nondestruct. Eval,* vol. 5, no. 3/4, 1986.

[22] J. D. Achenbach, Wave Propagation in Elastic Solids, Butterworth-Heinemann, 1973.

8 Comparison of other techniques to measure the thickness of a MEMS pressure sensor membrane

8.1 Introduction

The previous chapter showed how applying time-frequency analysis to a multimode Lamb wave signal in a MEMS pressure sensor membrane can allow for the determination of membrane thickness among other properties. As stated at the start of this thesis, knowledge of membrane thickness is vital to understand the deflections and sensitivity of the pressure sensor when applied in a specific environment.

8.2 Scanning Electron Microscope

A measurement of the thickness of the membrane was achieved by taking an SEM image of the cross-section of the pressure transducer as shown in Figure 8.1 and Figure 8.2. From these figures, it can be seen that the thickness is approximately 36 μm, taking into consideration the slight angular deviation. This would strongly indicate that unless a very high resolution scanning electron microscope was used and the plane being imaged was exactly perpendicular to the imaging electron beam, using an SEM can only ever give an estimate of thickness.

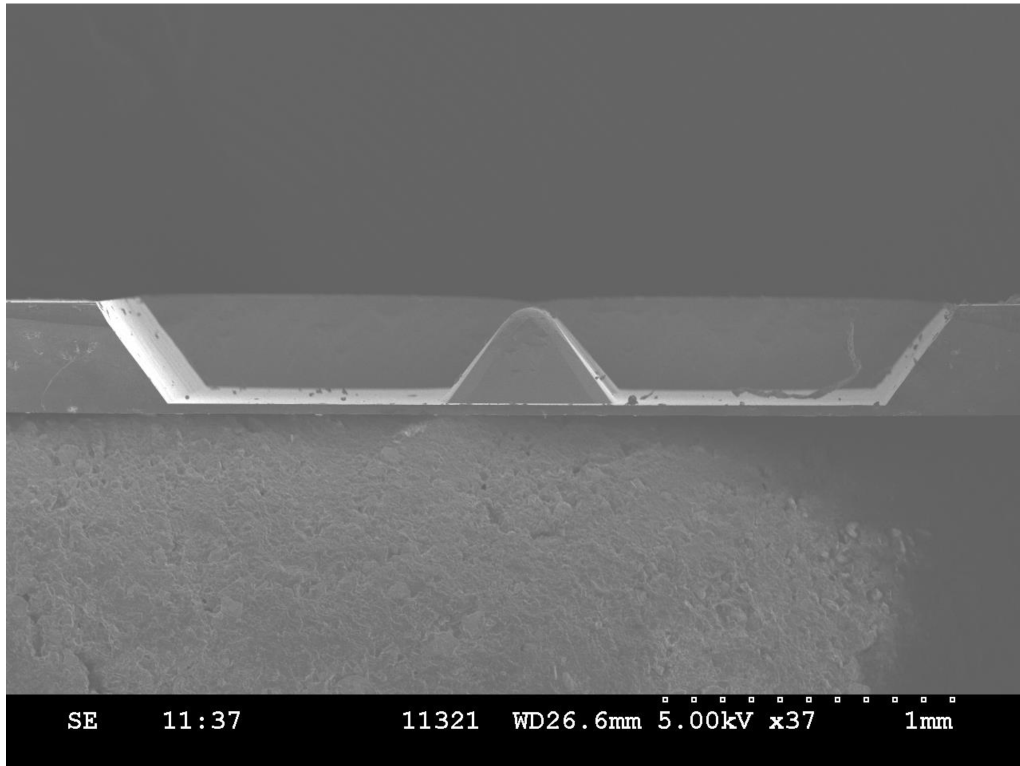

Figure 8.1: Cross-section of MEMS pressure sensor membrane (×37 magnification).

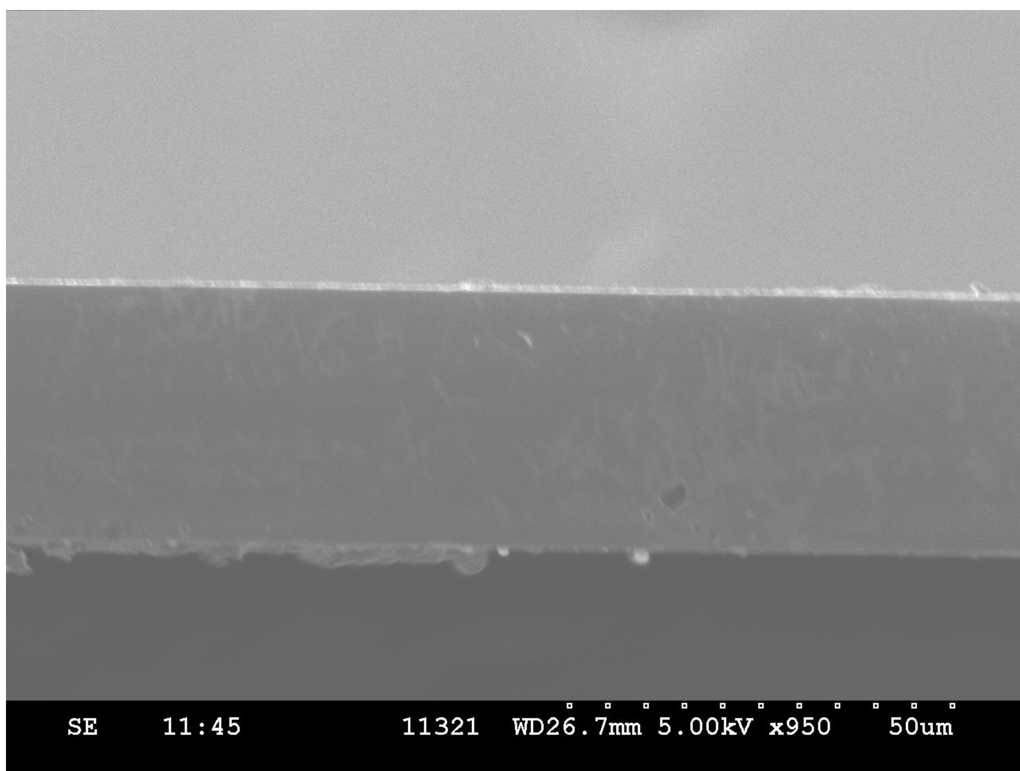

Figure 8.2: Cross-section of MEMS pressure sensor membrane (×950 magnification).

8.3 Infrared transmission of the MEMS pressure sensor membrane

Another method suitable for measuring the thickness of a material is to use light at a particular wavelength where the material is [partially] transparent. Obviously the material's optical properties would be "fixed", so the choice of laser wavelength is critical. Once a suitable wavelength is chosen, the two surfaces of the material will act as an etalon. If the refractive index of the sample is known, the separation of the surfaces, *i.e.* the sample thickness can be determined by measuring the interference between directly transmitted and internally reflected light. Interference produces intensity modulation with peaks occurring when the optical path length difference ($2nd$) between the two paths is an integer number of wavelengths. The difference between the peaks is the free spectral range $\Delta\upsilon$ (wavenumber) or $\Delta\lambda$ (wavelength) and is given as

$$\Delta\nu = \frac{c}{2nd} \qquad \Delta\lambda = \frac{\lambda^2}{2nd} \tag{8.1}$$

where c is the speed of light in vacuum, λ is the wavelength, n is the real part of the refractive index and d is the plate thickness.

The experiment set up to measure the thickness is shown in Figure 8.3. The laser source was a Santec TSL210 fibre laser with a wavelength range of 1530 nm to 1610 nm. The light was delivered via an optical fibre and was incident perpendicular to the sample. The transmitted light was focused onto a photodiode using a ×10 microscope objective and the signal was amplified using a Fempto Amplifier (DHPCA-100).

Over the wavelength range produced by the laser, there is a change in refractive index of the sample. This was corrected for using the Sellmeier equation for silicon given below

$$n^2(\lambda) = 1 + \frac{B_1\lambda^2}{\lambda^2 - C_1} + \frac{B_2\lambda^2}{\lambda^2 - C_2} + \frac{B_3\lambda^2}{\lambda^2 - C_3} \tag{8.2}$$

where n is the refractive index, λ is the optical wavelength (given in micrometres) and B_i and C_i are the Sellmeier coefficients given in Table 8.1 [1-3]. The Sellmeier equation is plotted in Figure 8.4

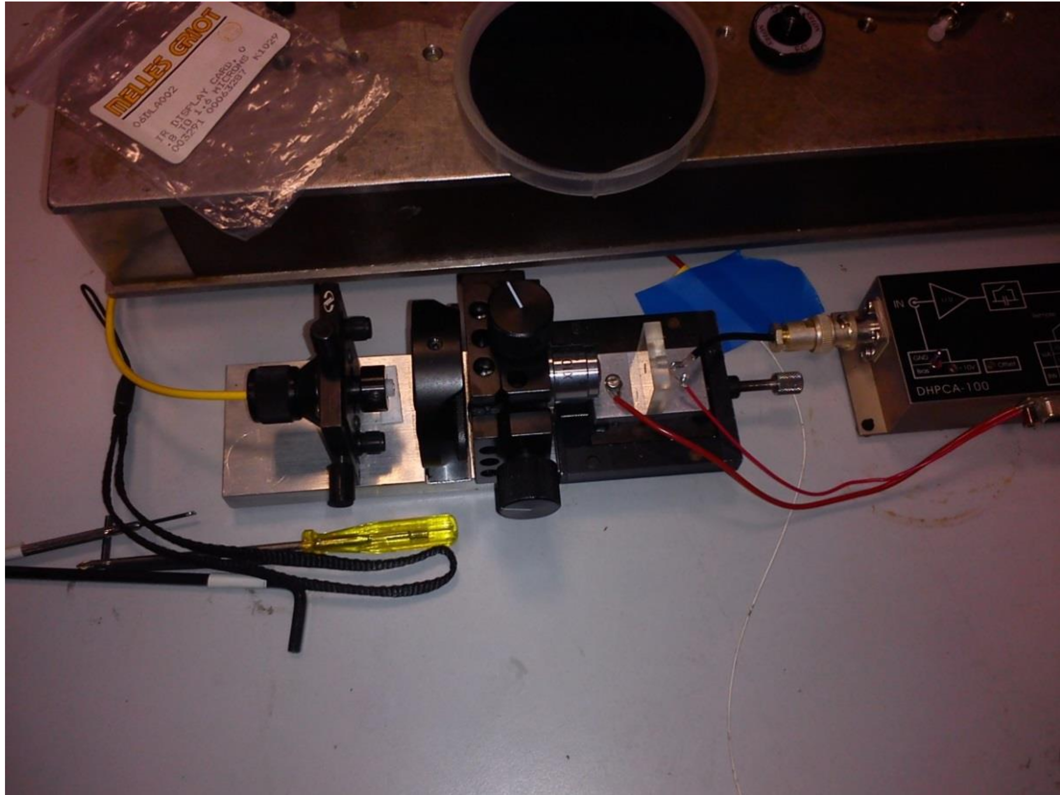

Figure 8.3: Experimental setup to measure the infrared transmission of the MEMS pressure sensor.

Table 8.1: Sellmeier coefficients.

B1	10.66842933
B2	0.003043475
B3	1.54133408
C1	0.3015116485
C2	1.13475115
C3	1104

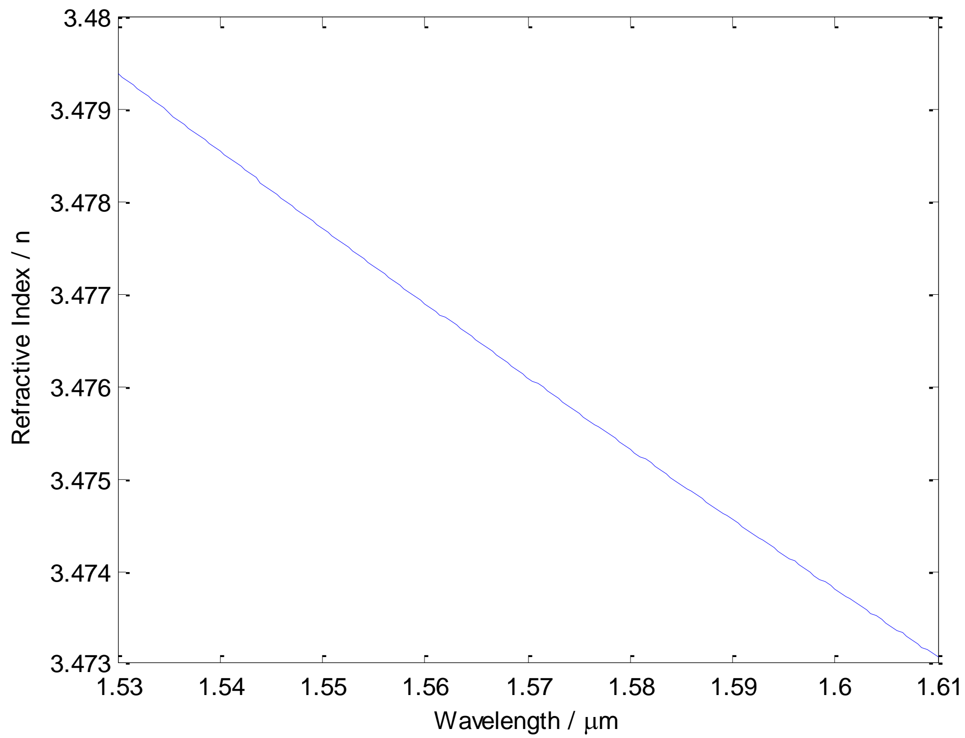

Figure 8.4: Sellmeier equation for the wavelength range 1530 nm to 1610 nm.

Figure 8.5 below shows the transmission spectrum for the MEMS pressure sensor. From the measured peaks, and using equation 8.2, the thickness of the MEMS pressure sensor membrane was calculated to be 34.6 µm ± 0.27 µm.

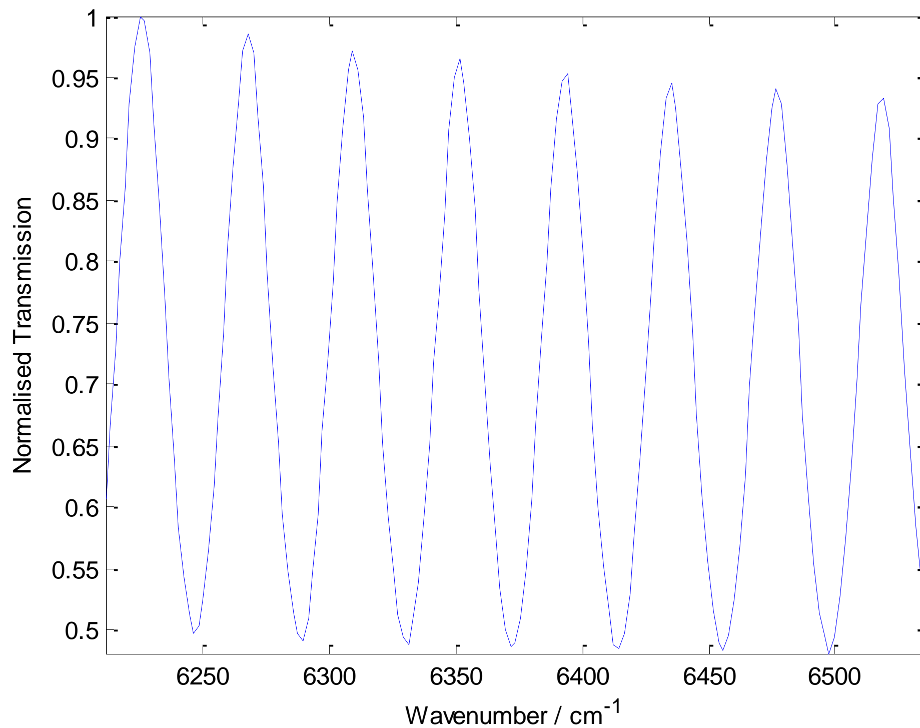

Figure 8.5: Transmission spectrum for the MEMS pressure sensor.

8.4 Conclusions

Using the Lamb wave group velocity method, a thickness for the membrane was determined to be 35.01 μm ± 0.18 μm and from the results above, the thickness was determined to be 34.6 μm ± 0.27 μm. It is reasonable to conclude that these two results are in good agreement with each other. The second point to consider is that both measurements were not taken at the same location, allowing for thickness variations within the membrane.

8.5 References

[1] B. Taitian, "Fitting refractive index data with the Sellmeier dispersion formula," *Appl. Opt.*, vol. 23, p. 4477, 1984.

[2] D. F. Edwards and E. Ochoa, "Infrared refractive index of silicon," *Appl. Opt.*, vol. 19, p. 4130, 1980.

[3] M. J. Weber, Ed., Handbook of Optical Materials, CRC Press, 1992.

9 Conclusions and Future Work

9.1 Conclusions

The development and operation of MEMS pressure sensors requires an accurate knowledge of the physical parameters and material properties of the materials used in production. The measurement of membrane thickness and material properties (Young's modulus and Poisson's ratio) was achieved using laser generated and detected ultrasonic Lamb waves, coupled with the utilisation of Gabor time frequency analysis to obtain a group velocity dispersion curve.

This thesis has been divided into three sections. The first section introduces the problem of MEMS characterisation (Chapter 1) and outlines a state of the art review (Chapter 2). The second section (Chapters 3, 4 and 5) describes the theory of laser generated ultrasound, optically detected ultrasound and an introduction to the theory of Lamb waves. Finally, Chapters 6, 7 and 8 present the results of the thesis, detailing the effect of applying a thin metallic film has on the generation efficiency of laser generated ultrasound, the determination of the membrane thickness in a MEMS pressure sensor, along with estimates of the material properties, Young's modulus and Poisson's ratio and finally, verifying the membrane thickness.

When considering which laser source to use to generate acoustic waves, Chapter 6 shows that light at 532 nm is the optimum choice (from the fundamental and harmonics of an Nd:YAG laser). Most metals have a high reflectivity in the near IR, ruling out 1064 nm and from a safety point of view 355 nm is not ideal. It was also shown that there was little difference in the acoustic waves generated by 355 nm and 532 nm. As a result of this work, the concept of the photostrictive effect in silicon was demonstrated. Photostriction can be used as a good indicator of Poisson's ratio, but in this case, this required the reliance on literature values and "guessing" of doping levels.

The main focus of Chapter 7 was to use laser generated and detected ultrasound to measure the thickness, Young's modulus and Poisson's ratio of the membrane in a MEMS pressure sensor. This was achieved by measuring a broadband signal and using a Gabor time-frequency representation to obtain the frequency at which the S_1 mode approaches zero group velocity. By using this method, a value for membrane thickness was determined to be 35.01 µm ± 0.18 µm. Values of 163 GPa ± 11.7 GPa for Young's modulus and 0.351 for Poisson's ratio in the [110] direction were also estimated and these varied from accepted values by -3.6% for Young's modulus and -2.5% for Poisson's ratio.

Finally, Chapter 8 using the phenomena of interference due to infrared transmission to verify the membrane thickness to be 34.6 µm ± 0.27 µm.

This just leaves one final question to be answered. Could the method described in this thesis to measure membrane thickness, Young's modulus and Poisson's ratio be used within a current MEMS pressure sensor manufacturing line? The method and equipment would be suitable as part of a manufacturers quality control, within a quality (or otherwise) laboratory. The equipment and method would non-destructively and remotely be capable of measuring the above parameters. Incorporating the method described in this thesis into a production line would prove more difficult. Computing power and digital signal processing algorithms have progressed enough to make this possible, however the major problem would be with the detection system. This would need to be adequately shielded to protect against the more electrically noisy environment, but additionally the signal to noise ratio would need to be improved so signal averaging could be reduced or ideally removed. The current experimental setup would not be suitable for this type of inspection integration.

9.2 Future Work

In order to improve on the measurements made in this thesis with the Michelson interferometer, two modifications must be taken into consideration. The first is the detection spot size on the sample. With the current arrangement, this will detect acoustic waves with bandwidths up to 500 MHz. To achieve a larger bandwidth, smaller spot sizes (possibly through utilisation of shorter wavelength lasers) must be used. The second modification is with the detection electronics. The current amplifier is limited to 200 MHz, which was suitable for this work, but will most likely need expanding if smaller structures are to be measured.

If the work in Chapter 6 was to be repeated, or more likely, applied to future work involving thin films on substrates, it is extremely important that the optical constants, such as refractive index and extinction coefficient are measured independently and literature values are not relied on. Another interesting variation of this work would be to study the effect of acoustic wave generation efficiency with varying film thickness.

While the results in Chapter 7 show that by using a single measurement, an accurate value of membrane thickness can be achieved along with good estimates for Young’s modulus and Poisson’s ratio, these results were only obtained in a single orientation.

Publications

Laser Ultrasound for the Non Contact Characterisation of the Mechanical Properties of Materials.

Culshaw, B. Sorazu, B. Pierce, G. McKee, C. Thursby, G.

1st International Symposium on Laser Ultrasonics: Science, Technology and Applications 2008

CW Laser generated ultrasound techniques for microstructure material properties evaluation.

Thursby, G. Culshaw, B. Pierce, G. Cleary, A. McKee, C. Veres, I.

Proceedings of SPIE - The International Society for Optical Engineering, v 7293, 2009, *Smart Sensor Phenomena, Technology, Networks, and Systems 2009*

Numerical investigation of elastic wave propagation in layered microstructures.

Veres, I. Cleary, A. Culshaw, B. McKee, C. Pierce, G. Thursby, G.

16th international congress on sound and vibration. 2009

A comparison of three optical systems for the detection of broadband ultrasound.

Thursby, G. McKee, C. Culshaw, B.

Proceedings of SPIE - The International Society for Optical Engineering, v 7648, 2010, *Smart Sensor Phenomena, Technology, Networks, and Systems 2010*

Simultaneous determination of elastic properties and thickness of orthotropic plates by Lamb waves.

Veres, I. Pierce, G. McKee, C. Cleary, A. Thursby, G. Armstrong, I. Culshaw, B.

Journal of the Acoustical Society of America. Not yet published.

Low Peak-Power Laser Ultrasonics.
Pierce, G. Culshaw, B. Veres, I. Cleary, A. Thursby, G. McKee, C. Swift, C. Armstrong, I. *Non Destructive Testing and Evaluation - Special Issue on Laser Ultrasonics. 26 (3-4).*

Laser Generated Ultrasound – Which Optical Wavelength is best?
McKee, C.
University of Strathclyde Research Presentation Day 2011

Laser generated ultrasound in metals and thin films on silicon.
McKee, C. Culshaw, B. Thursby, G. Cleary, A. Armstrong, I.
Review of Progress in QNDE, Vol 31.

Characterisation of a MEMS pressure transducer using Laser Generated Ultrasound.
McKee, C. Culshaw, B. Thursby, G. Cleary, A. Armstrong, I.
1st EOS Topical Meeting on Micro- and Nano-Optoelectronic Systems 2011.

Thickness measurement of silicon MEMS pressure sensor membrane using laser generated ultrasound.
McKee, C. Culshaw,B. Leach, R.
12th International Conference of the European Society for Precision Engineering & Nanotechnology 2012

End